UNIVERSITY OF NAIROBI

CHARACTERIZATION OF CHEMICAL BATH DEPOSITED NICKEL-DOPED CADMIUM SULPHIDE THIN FILMS FOR SOLAR CELL APPLICATIONS

BY

SHEILAH JEPKORIR BISACH

I56/76207/2014

A Thesis Submitted for Examination in Fulfilment of the Requirements for Award of the Degree of Master of Science (Physics) of the University of Nairobi.

2021

DECLARATION

I declare that this research work is my original work and has not been submitted elsewhere for examination, an award of a degree, or publication. Where other people's work or my work has been used, this has properly been acknowledged and referenced in accordance with the University of Nairobi's requirements.

Signature…… 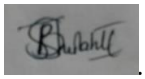 ……Date…….18/03/2021……

Sheilah Jepkorir Bisach

I56/76207/2014

Department of Physics

University of Nairobi

This thesis is submitted for examination with our approval as research supervisors:

Prof. Francis .W. Nyongesa Sign  Date… March 19, 2021…

Department of Physics

University of Nairobi

fnyongesa@uonbi.ac.ke

Prof. Robinson .J. Musembi Sign  Date… March 20, 2021…

Department of Physics

University of Nairobi

musembirj@uonbi.ac.ke

Prof. Bernard .O. Aduda Sign  Date …March 22, 2021…

Department of Physics

University of Nairobi

boaduda@uonbi.ac.ke

ABSTRACT

CdS films have received a lot of attention attributed to their high transparency, high absorption coefficient, high electron affinity, and outstanding photoconductive property. So far, the best performance of thin film solar cells has been achieved using ultra-thin polycrystalline CdS as a buffer layer. While CdS thin film is the best choice for use as a window/buffer layer, it still experiences optical losses in the low-wavelength region of the solar spectrum due to its low bandgap (2.42 eV). Previous research has shown that nickel widens the bandgap of some semiconductors such as ZnO, CdS, and Sb_2S_3. Therefore, nickel doping of CdS could be a feasible way of widening its bandgap. The current study is intended to enhance the optical properties of CdS, hence the performance of the solar cells and optoelectronic devices by doping with nickel during film growth to widen the bandgap of CdS. CdS:Ni thin films were synthesized using chemical bath deposition (CBD) with different concentrations of Cd^{2+} and Ni^{2+} (15 wt%, 25 wt%, 35 wt%, and 45 wt%). The films were prepared from an aqueous solution of 0.1M cadmium chloride, 1M thiourea, 0.05M nickel (II) chloride, 1M triethanolamine (complexing agent), and 35 wt% ammonia solution (pH regulator). The pH of the reaction bath was ≈11. The samples were annealed in air at varying temperatures (150 – 450 °C). The influence of nickel concentration and annealing temperatures on structural and optical properties of CdS thin films was studied. The incorporation of nickel into the CdS structure was recognized using X-ray diffraction (XRD). Optical properties, reflectance, and transmittance, in the range 200 nm-1500 nm were determined by UV-VIS-NIR spectrophotometer. The generated data were used to calculate other optical and solid-state properties like extinction coefficient (k), bandgap (E_g), absorption coefficient (α), refractive index (n), and Urbach energy (E_U). The films were found to be polycrystalline and exhibited a mixed-phase structure (cubic and hexagonal structures). It was further observed that the diffraction peaks shifted slightly to the lower angle with increasing Ni^{2+} concentration. This could be as a result of compressional micro-stress in the CdS lattice, due to the difference in ionic radii of Cd^{2+} ion and Ni^{2+} ion. The transmittance of the films was found to increase with an increase in both dopant concentration and annealing temperature. This may be as a result of the improvement in the crystallinity of the films with increasing dopant concentration and annealing temperature. The bandgap of as-prepared CdS:Ni was observed to widen as the nickel concentration was increased. This could be due to donor electrons occupying the states at the bottom of the conduction band blocking thus the low energy transitions (Burstein- Moss effect). On annealing the films, their bandgaps decreased when the temperature was raised upto 250 °C and then increased with further annealing at 350 and 450 °C. The decrease in the energy bandgap could be attributed to the increase in the grain size leading to denser films with lower bandgaps. The increase in the energy bandgap of films annealed at 350 and 450 °C could be attributed to the phase transition from cubic (zinc-blend) to hexagonal (wurtzite) structure. The absorption coefficients for all CdS:Ni thin films were found to be greater than 104 cm-1 in the visible region (380 nm to 780 nm) and near-infra red (780 and 2500 nm) regions which confirmed that the films have a direct optical energy gap. CdS:Ni thin films with 25 wt % and annealed at 250 °C were found to be the most appropriate films for use in solar cell as window/buffer layers as they recorded the highest transmittance with minimum optical properties (of Urbach energy of 0.16 and the lowest extinction coefficient) and had negative charges as the majority charge carriers. To realize higher conversion efficiencies in thin-film solar cells using CdS as window/buffer, we recommend further studies on film thickness and composition of the CdS:Ni thin films by varying the

deposition time, pH of the solution, the concentration of the reagents, and temperature of the reaction bath.

CONTENTS

Contents

LIST OF TABLES

LIST OF FIGURES

ACKNOWLEDGEMENTS

Foremost, I am grateful to God for guiding me through my research. My sincere thanks and appreciation goes to my supervisors Prof. Francis Nyongesa, Prof. Robinson Musembi, and Prof. Bernard Aduda, for their kind support during my MSc studies and research. Their supervision immensely assisted me during the research and writing of this thesis.

My sincere thanks also go to Dr. P. Karunakaran Nair of the Department of Solar Energy Materials, IER-UNAM México for his patience, and guidance. The knowledge he gave me was essential during this work. Am also profoundly indebted to Maria Luisa Ramón García of IER-UNAM México for help with XRD peak assignments.

I am genuinely appreciative to my postgraduate colleagues for their valuable discussion and critique while writing this thesis. I sincerely thank Victor Odari, Charles Opiyo, John Nguu, Nicholas Musila, Sr. Mary Taabu, and Jacinta Okwako for their knowledgeable guidance in my research. Special thanks to Celline Awino for help with the collection of X-ray diffraction (XRD) data.

Special thanks to Mr. Boniface Muthoka for being on standby to service equipment which was crucial towards the realization of this work. I want to express my warmest thankfulness to members of the Department of Physics, University of Nairobi, who gave me valuable advice, encouragement, and ideas throughout this work.

I am sincerely grateful to the Department of Physical Sciences, Chuka University, for enabling me to carry out Hall Effect measurements using their equipment.

I shall forever be indebted to Condensed Matter Group, Department of Physics; and the International Science Programme (ISP) of Uppsala University, Sweden for awarding me a scholarship that enabled me to study my MSc. To you, I say thank you.

Finally, I would like to thank my family: my husband, my parents, sisters, and brothers for their love, encouragement and prayers throughout my research.

DEDICATION

I dedicate this thesis to my husband, Josky, who has been a constant source of support and encouragement during the challenges of graduate school and life.

CHEMICAL SYMBOLS

Al	Aluminium
Cd	Cadmium
$CdCl_2.21/2H_2O$	Hydrated Cadmium Chloride
CdO	Cadmium Oxide
$Cd(OH)_2$	Cadmium Hydroxide
CdS	Cadmium Sulphide
CdTe	Cadmium Telluride
CH_4N_2S	Thiourea
CIGS	Copper Indium Gallium Selenide
Co	Cobalt
CO	Carbon Monoxide
CO_2	Carbon Dioxide
Cr	Chromium
Cu	Copper
$F:SnO_2$	Fluorine-doped Tin Oxide
Fe	Iron
Ga	Gallium
H	Hydrogen
In_2S_3	Indium Sulphide
In	Indium
Li	Lithium
Mn	Manganese
M^{n+}	Metal salt
NH_3	Ammonia solution
Ni	Nickel
Ni_3S_2	Nickel sulphide
Ni_3S_4	Nickel sulphide
$NiCl_2.6H_2O$	Hydrated Nickel (II) Chloride

O	Oxygen
OH^-	Hydroxide
P_2O_5	Diphosphorus Pentoxide
Se	Selenium
S	Sulphur
SO_2	Sulphur dioxide
Zn	Zinc
ZnS	Zinc Sulphide
ZnSe	Zinc Selenide
X^{m-}	Chalcogenide ion

ABBREVIATIONS

α	Absorption coefficient
β	Line broadening in radians
β_T	Band tailing parameter
θ_B	Braggs angle
λ	Wavelength
μ	Carrier mobility
ρ	Resistivity
σ_{op}	Optical conductivity
ρ	Resistivity
υ	Drift velocity
Å	Angstrom (10^{-10} m)
A	Constant
A_l	Ligand species
Abs	Absorption
B	Magnetic field
CAGR	Compound Annual Growth Rate
CBD	Chemical Bath Deposition
D_t	Thickness of the film
DMS	Diluted Magnetic Semiconductors
D_p	Average crystallite size
d	Interplane spacing
F_m	Magnetic force
D_p	Average Crystallite size,
F_e	Electric force
E_e	Electron charge
E	Electric field
E_g	Bandgap
E_F	Fermi energy

E_U	Band energy
EDXRF	Energy Dispersive X-ray Fluorescence
FETs	Spin Field Effect Transistors
FWHM	Full Width at Half Maximum
GDP	Gross Domestic Product
GIXRD	Grazing incidence x-ray diffraction
I	Current
IRENA	International Renewable Energy Agency
ISE	Institute for Solar Energy Systems
J	Current density
JCPDS	Joint Committee on Powder Diffraction Standards
K	Constant
k	Extinction co-efficient
KeV	Kilo electron Volts
K_i	Instability constant
K_{sp}	Solubility product
kWp	Kilowatt peak
l	length
LED's	Light Emitting Diodes
Log	Logarithm
m	Constants
n	Refractive index
n_c	Concentration
NEA	Nuclear Energy Resource
n_s	Sheet concentration
^oC	Degrees Celsius
PL	Photoluminescence
PPC	Persistence Photo Conductivity
PV	Photovoltaic
q	Charge

R	Reflectance
R_B	Magnetoresistance
R_H	Hall coefficient
R_s	Sheet resistance
RX9	Graphite crystal
t	Time
T	Transmittance
TCO	Transparent Conducting Oxide
TEA	Triethanolamine
TM	Transition Metals
UV	Ultra Violet
VIS-NIR	Visible-Near Infra-Red
wt%	Weight percentage
XRD	X-Ray diffraction
V_H	Hall voltage
V_{OC}	Open circuit voltage

CHAPTER 1

INTRODUCTION

1.0 Background

Production and the supply of clean, safe, and sustainable energy is one of the critical challenges facing current civilization (Balzani and Armaroli, 2010). The rapid population and economic growth have significantly increased the energy demand, making it one of the essential resources for humankind's existence. Currently, fossil fuels constitute over 80% of the total energy consumed by humankind (World energy outlook, 2018). Exploitation and combustion of fossil fuel to meet our energy demand has been very convenient but has caused harm to the environment and human health through the emission of greenhouse gases (e.g. CO_2, CO, SO_2, and P_2O_5) and toxic waste, climate change, ozone depletion, water and land degradation due to oil spills and coal-ash spills and air pollution (Casper, 2010). Heat-trapping properties of carbon dioxide released into the atmosphere contributes to global warming resulting in extreme weather such as heavy rain, searing and prolonged heat waves, intense hurricanes, and recurring droughts (Bradford, 2006; Balzani and Armaroli, 2010). Black carbon particles are also a significant contributor to global climate change, as it strongly absorbs sunlight and has a heating effect on the atmosphere. Black carbon particles remain in the atmosphere for only a few weeks, therefore reducing emissions would instantly lower the rate of global warming. There is a need to explore new sources of energy that are environmentally friendly, inexhaustible, and available worldwide (Bradford, 2006; Balzani and Armaroli, 2010).

With the uneven global distribution of fossil-fuel resources on earth (McGlade and Ekins, 2015), renewable energy technologies promise to slow our dependence on the expensive, scarce, and environmentally unfriendly fossil fuels. Renewable energy is a potential source of clean energy for the reason that they preserve natural resources; their operating costs are low, low carbon emissions, and are sustainable (IRENA, 2012). Lately, there has been an increase in the usage of renewable energy because of the high cost of fossil fuels and concerns over greenhouse gases and toxic waste.

Solar energy is a renewable source of energy with high potentials for meeting global energy consumption. It is an inexhaustible source of energy at any reasonable period for human civilization. Besides, it is abundant even in a situation of doubling or tripling present energy demand (Balzani and Armaroli, 2010). Photovoltaics are used to produce electricity by directly transforming light energy from the sun using the properties of suitable semiconducting materials. Solar power is also very convenient in remote areas in both terrestrial and extra-terrestrial, it is unlimited, cheap, clean, renewable, and well distributed in every part of the world. Energy from the sun reaching the surface of the earth surpasses our annual energy needs, given that one hour of sunlight could provide our annual needs for one year (Fyfe *et al.*, 1993). The benefits of solar energy over other renewable sources of energy include environment-friendliness; universal and versatile; low-cost maintenance; and a short energy payback period (Ayieko *et al.*, 2013).

Photovoltaic (PV) Systems are categorized into three generations, namely: first, second, and third-generation Photovoltaics Systems (IRENA, 2012). First-generation PV systems use the wafer-based crystalline silicon technology and are fully commercialized. Second-generation PV systems are based on thin-film technologies while third-generation PV systems are still under demonstration and have not been widely commercialized, e.g., intermediate-level cells (impurity PV and intermediate band solar cells), concentrator systems, thin-film tandems, a-Si tandems, Si nanostructure tandems, organic PV Systems, multi-colour (tandem) cells, group III-V tandems and hot electron -carrier cells (Conibeer, 2007).

Over 80% of commercially available solar cells are based on silicon technology which needs high purity silicon material. The best laboratory solar cell efficiencies for mono-crystalline and multi-crystalline silicon wafer-based technologies are 26.7% and 22.3%, respectively (Green *et al.*, 2018; Fraunhofer ISE: Photovoltaics Report, 2019). The thickness of the absorber layer for a crystalline solar cell is around 300 μm. About 10 kilograms to 15 kilograms of silicon is required to produce 1 kWp (Shah *et al.*, 1995). Production of silicon solar cells requires the use of high purity raw material which makes it expensive to produce. Unlike silicon solar cells which require about 200μm - 300μm thick active layer, an active layer of a few micrometers (μm) is necessary to produce thin-film solar cells (Chopra *et al.*, 2004). Thin-film solar cells promise thinner, less expensive, and more flexible technology compared to silicon solar systems. Lately, efforts have been made to develop and research more on thin-film solar cells because it is easy to manufacture.

Recently, thin-film solar cell laboratory conversion efficiencies have progressively improved promising reduced manufacturing costs compared to silicon technology (Green *et al.*, 2018).

Over the last 15 years, the global Compound Annual Growth Rate (CAGR) of photovoltaic installations was above 24%. The annual new solar PV system installations were 29.5 GW in 2012 and 99.8 GW in 2017 (Jäger-Waldau, 2018). The increase in new PV system installations during this period is attributed to a global decrease in the cost of PV systems and also as a result of shifting to large-scale utility systems. The market share of thin-film technologies in 2017 was about 5% of the total annual production (Fraunhofer ISE: Photovoltaics Report, 2019). The highest lab efficiency in thin-film technology is 22.9% for CIGS ($CuIn_{1-x}\ Ga_xSe_2$) and 21% for CdTe solar cells (Green *et al.*, 2018). In the last ten years, CdTe module solar energy conversion efficiency increased from 9% to 16% (Fraunhofer ISE: Photovoltaics Report, 2019).

1.1.1 Why thin-film materials?

Thin film semiconductors can be "grown" on a substrate through "the random nucleation and growth processes of individually condensing or reacting atomic, ionic or molecular species" (Chopra *et al.*, 2004). Deposition parameters strongly influence the structural and physical properties of these materials. The different microstructure of films, i.e., epitaxial growth, nanocrystalline, amorphous, and extremely oriented films, can be obtained by using various deposition methods and substrates while varying the deposition parameters. The substrate can be rigid, flexible, insulator, or metal with varying shapes, sizes, areas, and structures (Chopra *et al.*, 2004).

There exist a variety of deposition methods for thin films. These include; electrophoresis, chemical bath deposition, screen printing, sputtering, chemical vapour deposition, resistive evaporation, spray pyrolysis, laser ablation, ion-exchange reactions, and glow discharge decomposition. Thin films can be fabricated using a single method or a combination of methods. Doping of materials can also modify the characteristics of thin films in desired and controlled ways. Desired profile in the growing films can be obtained by controlling the doping profile (Chopra and Das, 1983). Different types of electronic junctions are possible too for thin film materials. Lattice constants and graded bandgap can be engineered to develop designer solar cells.

1.1.2 Materials for buffer/window layers and how they affect the performance of thin film solar cells

Window and buffers layers play a fundamental role in thin-film solar cells. Buffer and window layers minimize recombination losses while assisting in achieving large band-bending. The buffer layer also guards the junction against the chemical reactions and damage while enhancing band alignment of the cell and creating a wide depletion region with the absorber layer (Contreras *et al.*, 2002). Therefore, for high-efficiency thin-film solar cells, the bandgaps of the window and buffer layers must be wide, and their thicknesses must be as small as possible to retain low series resistance.

Solar cells made with optimized and appropriate buffer layers produce better optical (lattice) matches with the absorber and thereby reduce recombination at the interface (Siebentritt, 2004). High-efficiency thin-film solar cells with large short circuit current and open-circuit voltage can be produced by optimizing buffer layers (Von Roedern and Bauer, 1999). Buffer layers in heterojunction solar cells play a role in adjusting the interface charge, to ensure the position of the Fermi level at the interface above the bandgap centre of the absorber (Siebentritt, 2004).

The CdS (direct bandgap ≈ 2.42 eV) thin film is an excellent heterojunction solar cell partner commonly used as a window/buffer material in thin-film CdTe and Cu(In,Ga)Se_2 polycrystalline photovoltaic devices (Mustafa *et al.*, 2012) due to symmetric emission spectrum, narrow and tunable bandgap, and broad, continuous excitation spectrum (Bhambhani and Alvi, 2016). CdS films have received a lot of attention because of their high transparency, high absorption coefficient, easy ohmic contact, outstanding photoconductive property, and high electron affinity. Thin-film CdS is more photochemically stable than silicon nanoparticles (Bhambhani and Alvi, 2016). Because of these exceptional optical properties, CdS is mostly used as a window or buffer layer in solar cells, photo-detector, photoconductors, photo-resistors, green lasers, electrical driven laser, light-emitting diodes, address decoder, and sensors (Mustafa *et al.*, 2012; Bhambhani and Alvi, 2016).

Although several wide-bandgap Cd-free buffer layers materials have been explored for buffer layer, for example, Zn(O,S) (Thankalekshmi and Rastogi, 2012), Zn(OH,S) ZnO (Ennaoui *et al.*, 1998), (Ennaoui *et al.*, 2003; Hubert *et al.*, 2008), ZnS (Nakada and Mizutani, 2002; Nakada *et*

al., 2003), ZnSe (Hariskos *et al.*, 2005) and In_2S_3 (Huang *et al.*, 2001; Bayon and Herrero, 2001) as an alternative to CdS, the best performance is attained using ultra-thin polycrystalline CdS (Alam *et al.*, 2014).

Band offsets at the buffer/absorber interface mostly influence the functioning of a solar cell. These band offsets are greatly influenced by the deposition method because of the intermixing and chemical reactions at the interface (Nakada and Mizutani, 2002). A positive conduction band offset at the buffer/absorber interface helps to reduce interface recombination (Siebentritt, 2004). And so, there is a need to improve the conduction band alignment and to explore the influence of the buffer–absorber interface on the functioning of a solar cell.

Cadmium and sulphur atoms favourably influence the surface or near-surface chemistry of the absorber material. Sulphur is thought to passivate surface defects while the cadmium atoms diffuse into the near-surface region of the absorber film aiding in defect passivation and/or n-type doping (Elango, 2012).

Chemical Bath deposited CdS is commonly used for efficient solar cell technologies (Ballipinar and Rastogi, 2017). It is fine-grained and resistive. When used as a buffer layer, the chemical bath deposited CdS forms a high quality junction with the absorber at the same time allowing the maximum amount of light to the junction. CdS large bandgap allows transmission of longer wavelength sunlight into the absorber layer, enhancing the efficiency of the photovoltaic device. CdS buffer layer is very compatible with the crystal lattice of the absorber layer and has favourable conduction band alignment (Alam *et al.*, 2014). Efficiencies of up to 22.3% laboratory efficiency have been reported on $Cu(In,Ga)Se_2$ solar cells with CdS as a buffer layer (Jackson *et al.*, 2011).

Chemical bath deposited CdS films show high resistance in the range $10^5\Omega$ cm-$10^7\Omega$ cm (Ristova, 1998). This high resistivity needs to be reduced to at most 10Ω cm while preserving the films' good photosensitivity. Several ways which have been used to try to minimise CdS' dark resistivity include the annealing (in nitrogen/hydrogen atmosphere and rapid thermal annealing) and the doping of CdS with metal impurities during (in-situ doping) or after the deposition process (Khallaf *et al.*, 2008).

Doping of CdS with impurities enables us to alter its properties to achieve desired properties, making them multifunctional both as a window and buffer layer for thin-film solar cells

(Bhambhani and Alvi, 2016). Doping alters its carrier concentrations, transmittance, morphology, bandgap, magnetic properties, the density of states, electrical conductivity, etc. The dopant ions and dissimilarity typically determine the outcome of doping of these semiconductors in ionic radii with the host atoms (Elango, 2012). The dopant's ionic radius determines whether the dopant ion could replace the desired ion in the lattice structure. The Ni^{2+} ion is one of the efficient dopants among the various transition metal ions suitable for altering the optical, electrical, and magnetic properties of multiple semiconductors. It is possible to incorporate Ni^{2+} ions into the CdS structure because of its small ionic radius (0.069 nm) and high electronegativity (1.91 Pauling) likened to that of Cd^{2+} ions whose ionic radius and electronegativity are 0.097 nm and 1.91 Pauling, respectively (Gellings and Bouwmeester, 1997).

In this work, we study the influence of nickel concentration and annealing temperatures on the optical and structural properties of CdS thin films prepared using the chemical bath deposition method for solar cell and optoelectronic applications.

1.2 Statement of the Problem

Studies made on CdS thin film prepared using various deposition methods have shown that the desired quality of films can be obtained by incorporating dopant impurities during film growth depending on the film applications. The structural, optical, electrical, and magnetic properties of CdS can be tailored to achieve desired characteristics suitable for various applications by doping with various amounts of dopant material. CdS is a suitable material for applications as a window and buffer layer in a thin-film solar cell structure. However, for these layers to play their roles well, their bandgap must be suitably wide enough to increase the amount of light reaching the absorber layer to enhance cell efficiency. CdS thin films experience optical losses in the low-wavelength region of the solar spectrum due to their low bandgap (2.42eV). In this study, we hope to enhance the optical properties of CdS and by extension, the performance of the solar cells and optoelectronic devices by doping with nickel to widen the bandgap of CdS.

1.3 Justification and Significance of the Study

Several approaches for the deposition of high-quality CdS thin films geared towards improving the conversion efficiency of these devices have been investigated over the years. But currently, the idea of doping the buffer/window layer has not been widely explored. Doping is a promising

method for tailoring the structural, optical, and electrical properties of CdS. Previous research has shown that nickel widens the bandgap of some semiconductors such as ZnO (Thakur *et al.*, 2013); CdS (Elango *et al.*, 2012); and Sb_2S_3 (Nwofe and Agbo, 2017; Mushtaq *et al.*, 2016). Therefore, nickel doping of CdS could be a feasible way of widening its (CdS') bandgap; hence, improving the performance of the solar cell and optoelectronic devices. Incorporation of dopant impurities can be done during film growth or after deposition, and in our study, we will introduce the dopant impurity (nickel) during film growth using chemical bath deposition. There is relatively little research on the effect of nickel doping on CdS. The few studies available focus on the preparation of CdS:Ni nanoparticles (Bhambhani and Alvi, 2016); (Rao *et al.*, 2011) while those that have prepared CdS:Ni thin films have used other deposition method including; sol-gel spin coating technique (Chtouki et al., 2017) and spray pyrolysis (Rmili *et al.*, 2013). This study is expected to provide information on the effect of nickel doping of CdS thin films prepared using a simple and cheap method of deposition, namely chemical bath deposition.

1.4 Aim and Objectives

1.4.1 Aim

This study aims to synthesize and characterize Ni-doped CdS thin films by chemical bath deposition technique for use in thin-film solar cells as a window/buffer layer and also for applications in electronic and optoelectronic devices.

1.4.2 Objectives

The objectives of this study are to:

1. To analyze the effect of concentration of the nickel dopant on the structural and optical properties of Ni:CdS thin films prepared using a chemical bath deposition method.
2. To investigate the effect of annealing temperature on the structural and optical properties of Ni-doped CdS thin films prepared using a chemical bath deposition method.
3. To study electrical properties (hall effect measurements) of doped Ni:CdS thin films

CHAPTER 2

LITERATURE REVIEW

2.1 Doping of Semiconductor Materials

The idea of the deliberate introduction of impurity atoms into nanocrystals of semiconductors to modify their electronic, optical, structural, and magnetic properties was first presented in the 1940s (Sze, 1990). Since then, much effort has been made to incorporate impurities into the lattice of the host atoms deliberately. For dopants to replace the host atoms, their atoms must be approximate of the same size as the host atoms. When the impurities' ionic radius is much smaller than that of host atoms, the impurities are not incorporated into the crystal lattice but reside between the crystal atoms on interstitial sites. This causes impurity levels in the bandgap and acts as recombination centres.

The properties of doped semiconductor material are determined by the type of impurity and the level of concentration. The type of impurity determines the structural, optical, electrical, and magnetic properties of the doped material enabling us to control and alter their properties to achieve desired characteristics suitable for various applications (Schubert, 2015).

A breakthrough in semiconductor physics came in the early 1990s when Bhargava *et al* (1994) successfully doped zinc sulphide nanocrystals with manganese. For the first time, the luminescence properties of zinc sulphide nanocrystals were improved by doping ZnS nanocrystals with Manganese. The Mn-doped zinc sulphide nanocrystals produced both high quantum luminescent efficiencies of upto 18% (Bhargava *et al*., 1994) and lifetime shortening concurrently. Five years later, Borse *et al*., (1999) observed that blue light emission (>425 nm) in highly luminescent ZnS nanoparticles was completely quenched when the ZnS nanoparticles were doped with nickel or iron (Borse *et al*., 1999). These two studies strongly indicated that the properties of doped semiconductor material are determined by the type of impurity and the level of concentration. From then onwards, there was an enormous upsurge of interest in studying doped-semiconductors nanocrystals because of their potential technological applications.

2.2 Doping of Cadmium Sulphide

Cadmium sulphide is a semiconductor material with a wide direct bandgap of 2.42 eV, they possess the properties of being highly transparent, high electron affinity, and excellent visible light absorption ability (Rmili *et al.*, 2013; Wang *et al.*, 2012). Because of these exciting properties, CdS has wide-ranging applications in optoelectronic and electronic devices which include: flat panel displays, logic gates, non-linear optical devices, light-emitting diodes, single-electron transistors, data storage, near field optical lithography, and telecommunications. CdS is also resilient to radiation which is advantageous for its usage in solar cells for space applications, where the devices are constantly exposed to radiation (Chandramohan *et al.*, 2009).

During the last two decades, extensive studies have been carried on doping CdS with various metallic elements by researchers using several deposition methods to prepare high-quality films appropriate for solar energy conversions, and optoelectronic applications. Most of these reports on doped CdS have shown notable changes in the bandgap. Some of the elements reported to have led to decreasing in band-gap of CdS include; manganese (Chandramohan *et al.*, 2009); lithium (Sahu and Chandra, 1987); (Shikalgar and Pawar, 1979); aluminium (Khallaf *et al.*, 2008); Akintunde, (2000) and Lokhande and Pawar, (1982); copper (Petre *et al.*, 1999); gallium (Khallaf *et al.*, 2009); and indium (Khallaf *et al.*, 2009). The dopant's ions replace Cd^{2+} ions either/both substitutionally and interstitially.

Remarkable results on bandgap tuning by doping of semiconductor material were obtained when CdS was doped with zinc. The energy bandgap of Zn-doped CdS films was reported to lie in between the bandgap of cadmium sulphide (2.42 eV) and that of ZnS (3.66 eV). This, therefore, means that the energy bandgap can be controlled to suit the application of the films by varying the ratio of Cd and Zn. This impressive energy bandgap of Zn-doped CdS films has led to a reduction in window absorption losses and an increase in short-circuit current in the solar cell. The films are now used in the fabrication of p-n junctions without lattice mismatches but with the help of quaternary materials (Jayaramaiah *et al.*, 2016). Nickel doping has also been reported to increase the bandgap of cadmium sulphide thin films (Elango *et al.*, 2012).

Luminescence properties of manganese-doped cadmium sulphide have been reported to be influenced by the concentration of manganese. A new emission band at 2.22 eV was observed on the manganese-doped cadmium sulphide samples by Chandramohan *et al* (2009). This provides a

possibility of incorporating optically active impurity centres in cadmium sulphide which may be useful in making flat panel display devices

Doping of CdS with metallic ions may increase or decrease the resistivity of films. This is seen in the resistivity of $Cd_{1-x}Fe_xS$ films synthesized by chemical vapour deposition with varying Iron contents on c-plane sapphire (Wu *et al.*, 2006). It was found that as the iron contents increased, the resistivity of the films also increased because of the ionization of holes from trivalent Fe^{2+} ions.

On the other hand, lithium doping has also been reported to reduce the resistivity of cadmium sulphide thin films (Sahu and Chandra, 1987; Shikalgar and Pawar, 1979). Like lithium doped cadmium sulphide thin films, the resistivity of chemical bath deposited aluminium-doped cadmium sulphide was lower as compared to that of pure CdS. Their lowest resistivity achieved was 4.6×10^{-2}cm, and the highest carrier density was $1.1 \times 10^{19}cm^{-3}$.

Doping of semiconductor material also enables us to control the electrical conductivity of semiconductor material. N-type indium-doped CdS prepared using thermal diffusion of indium showed an increase in electrical conductivity up to $300\Omega^{-1}cm^{-1}$ while their photosensitivity is completely lost (George *et al.*, 1995). Indium-doped cadmium sulphide films deposited by Jäger and Seipp (1981) by co-evaporation of cadmium sulphide and indium with varying indium concentration were reported to be of high conductivity. When cadmium sulphide was doped with high levels of indium concentration, indium atoms were doped interstitially into cadmium sulphide and formed an impurity band. Bertran *et al* (1984) also deposited In-doped films by co-evaporation of CdS and indium at varying deposition temperatures (160 °C, 220 °C, and 250 °C) and indium concentration ($10^{17}cm^{-3}$-$10^{21}cm^{-3}$). It was observed that at lower indium concentrations, the electrical conductivities of the films were highly dependent on deposition temperature. At $N_{In} = 8 \times 10^{18}cm^{-3}$ the electrical conductivity of the films was minimum which was a result of minimum mobility. It has also been reported that doping of CdS with a high concentration of dopant ions, i.e., Fe^{2+} may reverse the electrical conductivity of the films from n-type to p-type. (Wu *et al.*, 2006).

Though much effort has been put to dope CdS with various metallic ions, doping of cadmium sulphide with group II metallic ions, i.e., cobalt and nickel is not quite investigated. Ni^{2+} ions have an ionic radius of 0.069 nm, which is slightly less than that of Cd^{2+} (0.097 nm). Ni^{2+} has an electronegativity of 1.91 Pauling while Cd^{2+} of 1.61 Pauling (Gellings and Bouwmeester, 1997).

From this information, we can foresee Ni^{2+} ions substituting Cd^{2+} ions in CdS structure. Ni-doping of CdS have been reported to lead to an increase in the bandgap of CdS (Elango *et al.*, 2012); which is useful for solar cell application as a large bandgap allows transmission of longer wavelength sunlight into the absorber layer, enhancing the efficiency of the photovoltaic device (Rmili *et al.*, 2013).

2.3 Nickel Doping of CdS Thin Films

Window and buffer layers play significant roles in thin film solar cell structure as stated in section 1.1.2. For these layers to play their roles well, their bandgap must be suitably wide enough and their thicknesses are as small as possible to maintain low series resistance. Window/buffer layer with a larger bandgap increases the amount of light reaching the absorber layer, thus improving the cell efficiency. The best and typically used n-type window/buffer layer, CdS, still suffers from optical losses in the low-wavelength region of the solar spectrum because of the low bandgap (2.42 eV). One of the requirements for highly efficient solar cells is buffer thickness of <30 nm for efficiencies, η >18% (Sozzi *et al.*, 2014).

Previous research has shown that nickel widens the bandgap of some semiconductors such as ZnO (Thakur *et al.*, 2013); CdS (Elango *et al.*, 2012); and Sb_2S_3 (Nwofe and Agbo, 2017; Mushtaq *et al.*, 2016). Therefore, nickel doping of CdS could be a feasible way of widening its bandgap; hence, improving the performance of the solar cell and optoelectronic devices. The outcome of doping the bandgap of semiconductors will largely depend on its structure, type of material (n-type or p-type), and doping density (high/ low). Bandgap widening in n-type semiconductors is a result of the Burstein-Moss effect, i.e., the bandgap increases due to the shift of Fermi level to the conduction band occupying some of the bottom states in the conduction band (Lu *et al.*, 2007). Thus, a transition from valance band to conduction band will require large energy.

There is relatively little research on the effect of nickel doping on CdS. Most of these studies focus on the preparation of Ni-doped CdS nanoparticles (Bhambhani and Alvi, 2016); (Rao *et al.*, 2011). The few studies were done on Ni-doped CdS thin films can be considered as the first step towards a more profound understanding of the influence of nickel doping on CdS films. Rmili *et al.*, (2013) prepared Ni-doped CdS thin film using spray pyrolysis and studied its properties as a function of the [Ni]/[Cd] ratio. Rmili *et al.*, (2013) found that the bandgap of the films decreased as the amount

of nickel was increased. The films obtained had a relatively low resistivity of about $1.3x10^5\Omega$ cm. The undoped films had high transmittance values as compared to the Ni-doped films. The decreased transmittance makes the films not favourable for use in thin-film solar cells as most of the sunlight needs to be absorbed in the absorber layer to increase the efficiency of the solar cell. Also, films prepared using this technique are usually non-uniform with larger grain sizes because of the uncontrolled size of the sprayed droplet.

Chandran and Suresh (2011) prepared Ni-doped CdS nanocrystalline films using the chemical bath deposition method with deposition temperature at 75 °C. They observed that the nanocrystalline particles spread over the substrate. The films were annealed at 500 °C in the air for 1hr which is a possibility that the Ni-doped CdS film could have been oxidized. The question that then naturally arises is the appropriate annealing temperature of Ni-doped CdS films in the air. Previous literature shows that annealing cadmium sulphide at temperatures above 370 °C in air results in the formation of a thin layer of CdO layer (Nair *et al.*, 2001). Therefore, the high annealing temperature (500 °C) could have led to the decomposition of the films. Also, deposition temperature was a bit high for deposition of the smooth and uniform thin film layer. This could be the reason for the spreading of the nanocrystalline spread over the substrate. Deposition temperature of below 50 °C could be appropriate for the deposition of smooth and uniform layer of film. Thin films grown at slow growth reaction rate are adherent, thin and hard. The main drawback of films deposited at lower temperatures by chemical bath is the high series resistance.

Similarly, Chandran and Suresh (2011) prepared CdS films, Kumar *et al.*, (2013) prepared $Cd_{1-x}Ni_xS$ ($0 \leq x \leq 0.09$) nanofilms using chemical bath deposition with deposition temperature 70 °C for 80 minutes under constant stirring. The films were annealed at 300 °C. The films had relatively high transmittance (> 65%) and reflectance (< 20%) in the visible region. Also, the bandgap of the films was found to decrease with increased nickel content.

Ottih and Ekpunobi, (2011) prepared Ni-doped CdS films prepared using chemical bath deposition at room temperature various deposition time (8-24 hours) and investigated its optical properties. The film thickness was in the range of 0.3μm - 1.0μm and increased linearly with the deposition time. The thin films were also found to have very low transmittance values at the UV region and moderate transmittance values at VIS and NIR- region. The low transmittance values could be due to the long deposition time. The bandgap of the films increased with nickel doping with a bandgap

of about 3.30 eV. For solar cell application, similar films can be deposited for a short deposition time, i.e., 30 minutes to obtain a thin layer that can be used as a window/buffer layer. Films grown at a slower growth rate are adherent, thin and hard. The series resistance can further be reduced by making the film layer as thin as possible.

Chandramohan *et al.* (2010) prepared Ni-doped CdS thin films by 90 keV Ni^{+} implantation at room temperature. They observed that doping of CdS with Ni^{+} ions does not lead to any structural /phase transformation but induces structural disorder which brings about the decrease in the bandgap from 2.39 to 2.28 eV following nickel implantation up to 3×10^{16} ions cm^{-2}. The creation of shallow acceptor states also modifies the luminescence properties of CdS. The main disadvantage of using an ion implantation technique is that it uses very toxic gas sources, e.g., arsine and phosphine. It is also an expensive way of doping semiconductors.

From these studies on ni-doped CdS, we have noted that the bandgap of the films prepared using a chemical bath deposition method is strongly influenced by deposition parameters, particularly the role of deposition temperature. Generally, most deposition of CdS is done at raised temperatures (usually ≥ 60 °C). The literature review shows that in films prepared with deposition temperature above 50 °C, their bandgap decreased with increasing nickel content while those prepared with deposition temperature below 50 °C, bandgap increased with increasing nickel content. Previous studies have shown that increasing the deposition temperature speed up the film growth improves crystallinity, reduces bandgap and improves conductivity (Dona and Herrero, 1997); (Liu *et al.*, 2010).

As far as we know, no previous research has investigated the effect of annealing temperatures on structural and optical properties of CdS:Ni thin films. We have observed that most of the studies on nickel doping of CdS have emphasized the effect of nickel concentration on the structural, optical, electrical, and magnetic properties of Ni-doped CdS thin films. So here we are attempting to study both the effect of nickel concentration and annealing temperatures on structural and optical properties of cadmium sulphide thin films prepared using chemical solution deposition. We chose the chemical bath deposition technique to prepare the thin films because it is among the most suitable deposition methods to deposit high-quality films as it is cheap, simple deposition, and uses low-priced equipment facilities. This method is also ideal for depositing thin films over large and

irregular surfaces. Finally, it is a low-temperature deposition process that aids in the improved orientation of crystallites and grain structure.

CHAPTER 3

THEORETICAL FRAMEWORK

3.1 Introduction: Cadmium Sulphide

The n-type CdS thin film is the oldest and widely researched window/buffer layer material for heterogeneous solar cells (Mathew, 2009) because of its role as the best heterojunction partner for CdTe and Cu(In,Ga)Se_2 (CIGS) solar cells (Naciri *et al.*, 2007). The CdS occurs naturally in two forms: Greenockite which forms hexagonal crystals with the wurtzite structure and hawleyite has the zinc blende structure (Lohninger, 2011) as shown in Figures 3.1 and 3.2. The free energy of formation of both cubic and hexagonal phases varies slightly, and therefore, the existence of a mixed-phase is often seen during the growth of CdS (Kumar *et al.*, 2012). Hexagonal CdS is desirable for a solar cell application, owing to its excellent stability (Elango, 2012), good crystallinity (Moutinho *et al.*, 2003), and contains a low density of planar defects. The CdS thin films with high electrical conductivity are suitable for use in thin-film solar cells. High electrical conductivity contributes to a decrease in sheet resistance of the solar cell, consequently resulting in increased efficiency of the solar cell.

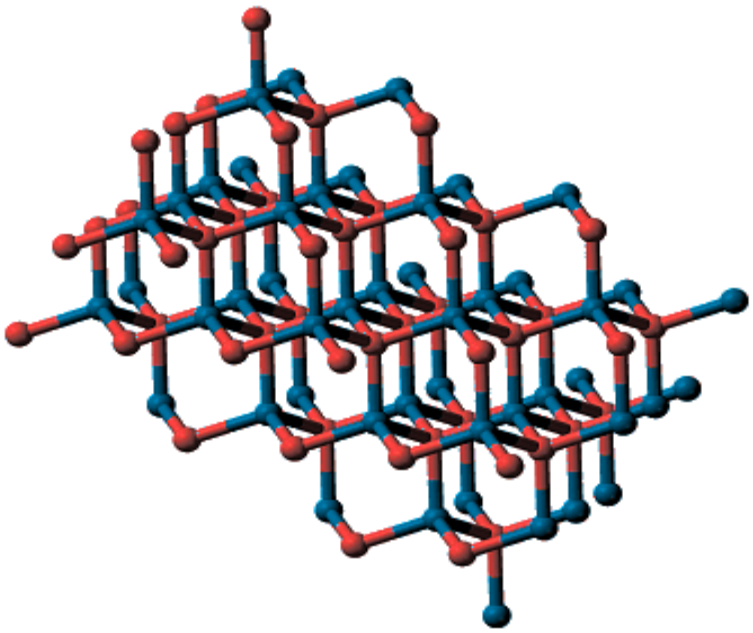

Figure 3. 1: Cubic structure of CdS (Source: chem.libretexts.org)

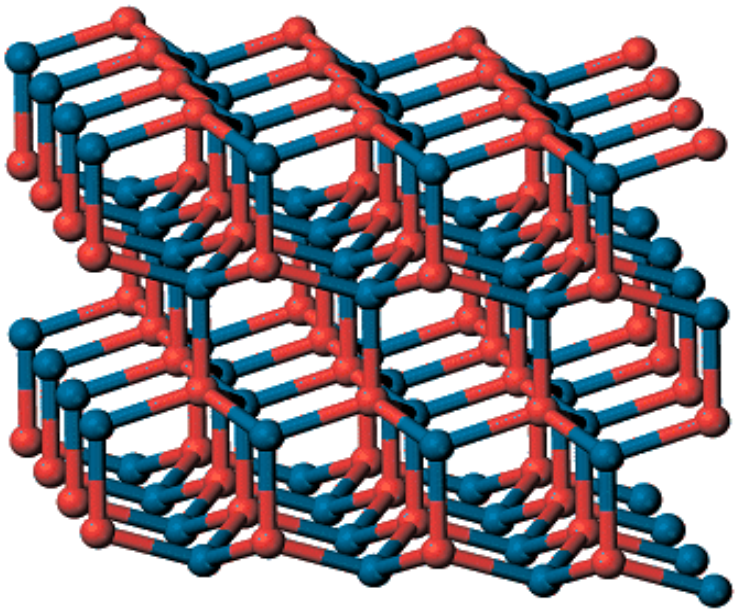

Figure 3. 2: Hexagonal structure of CdS (Source: chem.libretexts.org)

Conduction in pure cadmium sulphide is credited to native defects or sulphur vacancies and cadmium interstitials. We can, therefore, alter the conductivity of CdS by controlling the native defects by introducing impurity atoms into CdS nanocrystals. These impurities will influence the electrical conductivity of CdS (Rmili *et al.*, 2013). There are several approaches researchers have used to improve the quality of CdS thin films while preserving their good photosensitivity. They include the introduction of metal impurities during or after the deposition of CdS thin films (Petre *et al.*, 1999); and post-deposition treatments e.g. the annealing of the thin films in nitrogen/hydrogen/argon atmosphere and rapid thermal annealing. In our study, we introduced nickel ions into the structure of cadmium sulphide during deposition using chemical bath deposition and investigated the effect of nickel concentration and annealing temperatures on the structural and optical properties of Ni-doped CdS.

3.1.1 Chemical Bath Deposition

Chemical bath deposition, otherwise known as chemical solution deposition, is a cheap and simple deposition technique where films are "grown" on a substrate from a chemical reaction happening in an aqueous solution (Hodes, 2002); The solution contains a soluble metal salt Mn^{+} and a chalcogenide source (sulphide, selenide, telluride). The soluble metal salt dissolves in the solution,

releasing cations while the chalcogenide source decomposes, releasing anions. A layer of the compound is grown on the substrate when the cations and anions react. A precipitate is also formed in the bulk of the solution. Chalcogenide ions are gradually released into the solution wherein the free metal ion is buffered at a low concentration. The concentration of the free metal ion is regulated by the formation of complex species according to the reaction in equation (3.1) (Ortega-Borges and Lincot, 1993);(Hodes, 2002).

$$M(A)^{2+} \longleftrightarrow M^{2+} + A \tag{3.1}$$

The concentration of free metal ion at a particular temperature is given by equation (3.2) (Ortega-Borges and Lincot, 1993):

$$\frac{[M^{2+}]+[A]}{(M(A)^{2+})} = K_i \tag{3.2}$$

where A is the ligand species and K_i is the instability constant of the complex ion. The value K_i is different for the various complexing agents. An increase in instability constant means more ions will be released. The stability of this complex is influenced by the pH and temperature of the reaction bath. The complex is made more stable by increasing the pH while the complex becomes less stable when the temperature of the reaction bath increases. The complexing agent is added to the aqueous solution to control the hydrolysis of the metal ion. Therefore, metal ions concentration in the reaction bath is controlled by adding the concentration of a suitable complexing agent and the temperature of the reaction bath (Lakshmi, 2001). The temperature of the chemical bath is controlled by immersing it in an oil/water bath and heating it to the desired temperature, as shown in Figure 3.3.

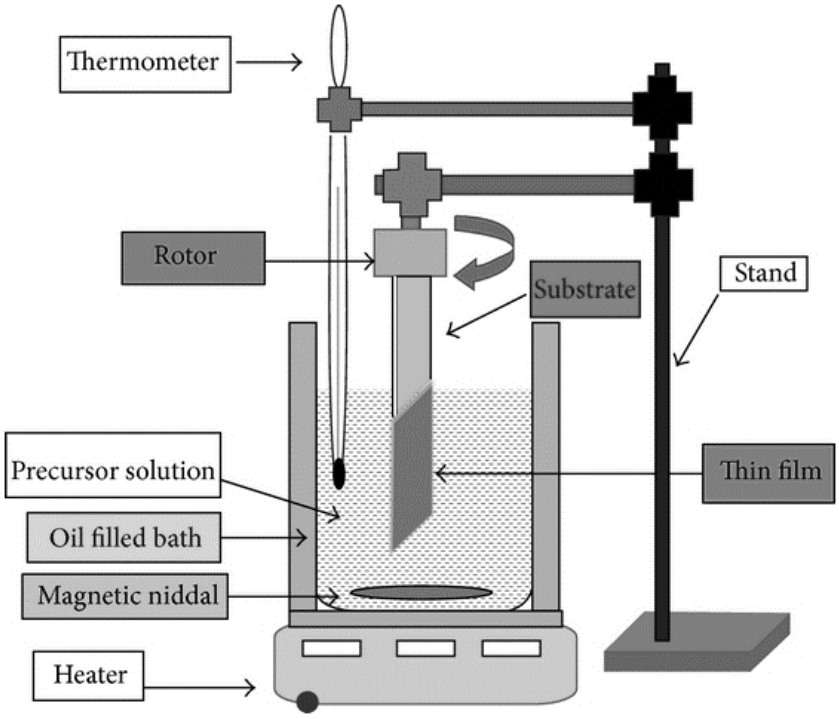

Figure 3. 3: Chemical bath deposition set up

(Source: (Pawar *et al.*, 2011)).

3.1.2 Principle of chemical bath deposition (CBD) technique

Formation of a precipitate in chemical solution deposition takes place when the ionic product of reactants surpasses the solubility product at a specific temperature. The solubility product gives the solubility of a sparingly soluble ionic salt. The more soluble is the salt, the greater the ion product, and the greater is its solubility product. On the other hand, solubility product also depends on the number of ions involved (Hodes, 2002). There will be no precipitation if the ionic product is not more than the solubility product as the solid phase produced will dissolve back to the solution. This is the principle behind chemical solution deposition.

3.1.3 Thin film deposition mechanisms in chemical bath deposition (CBD) technique

Thin-film deposition by chemical solution deposition occurs through the following four possible mechanisms: These are Simple ion-by-ion, simple cluster, complex decomposition ion-by-ion, and complex decomposition cluster (Hodes, 2002). Simple ion-by-ion mechanism and simple cluster (hydroxide) mechanism involve anions. In contrast, complex decomposition ion-by-ion

mechanism and complex decomposition cluster mechanism involve breaking carbon–chalcogen bond (Hodes, 2002).

3.1.3.1 Simple ion-by-ion mechanism

This deposition mechanism happens by sequential ionic reactions. The general reaction for the mechanism is given by (Hodes, 2002):

$$M^{n+} + X^{M-} \longrightarrow M_mX_n \quad (3.3)$$

Solid M_mX_n is formed once the ionic product $[M^{n+}][X^{m-}]$ surpasses the solubility product, K_{sp} of M_mX_n (Hodes, 2002). Therefore, no solid phase will be formed if the ionic product does not exceed the solubility product, K_{sp}. Thus precipitation process is not a one-way process but an equilibrium. A suitable complexing agent is added to the aqueous solution to retain metal ions in the solution and prevents hydroxide from precipitating out (Hodes, 2002).

3.1.3.2 Simple cluster (hydroxide) mechanism

Chemical bath depositions are done under circumstances where a metal hydroxide, $[M(OH)_n]$is formed. Metal hydroxide is formed either as an adsorbed species on the substrate or as a colloid but not in the bulk of the solution. Therefore, solid M_nX_n is formed by the reaction of X^{m-} ion with the $M(OH)_n$ (Hodes, 2002).

$$M^{n+} + nOH^- \longrightarrow MOH_n \quad (3.4)$$

$$M(OH)_n + M^{m-} \longrightarrow M_mX_n + nOH^- \quad (3.5)$$

3.1.3.3 Complex-decomposition ion-by-ion mechanism

This mechanism involves the complexation of free metal cations (Cd^{2+}) by thiourea as shown in equation (3.6) (Hodes, 2002):

$$SC(NH_2)_2 + Cd^{n+} \longrightarrow [SC(NH_2)_2 - Cd]^{n+} \quad (3.6)$$

$$[SC(NH_2)_2 - Cd]^{n+} + 2OH^- \longrightarrow CdS + CN_2H_2 + 2H_2O \quad (3.7)$$

3.1.3.4 The complex decomposition cluster mechanism

This mechanism is founded on the formation of a solid phase rather than reacting directly with a free anion as shown in the example of the formation of CdS (Hodes, 2002).

$$Cd(OH)_2]_n + SC(NH_2)_2 \longrightarrow Cd(OH)_2]_{n-1} + (OH)_2Cd - S - C(NH_2)_2 \quad (3.8)$$

$$Cd(OH)_2]_{n-1} + (OH)_2Cd - S - C(NH_2)_2 \longrightarrow Cd(OH)_2]_{n-1}CdS + CN_2H_2 + H_2O \quad (3.9)$$

(This process continues until all the metal hydroxide is converted to cadmium sulphide.)

3.2 Chemical Bath Deposition of Ni-doped CdS Thin Films

The formation of Ni-doped cadmium sulphide thin films using chemical solution deposition is based on the four main mechanisms, as explained in section 3.1.2. CdS is usually formed when its ionic product surpasses its solubility product (≈10-25). Doping of CdS with nickel, a transition metal element, has previously been successfully incorporated into the CdS structure to form CdNiS, ternary alloy (CdNiS). CdNiS precipitates in the bulk of the solution and also at substrates' surfaces forming a film through the following possible mechanisms: [Ortega-Borges and Lincot (1993); (Hodes (2002)]: simple ion-by-ion mechanism, simple cluster (hydroxide) mechanism, complex decomposition ion-by-ion mechanism, and complex decomposition cluster mechanism.

3.2.1 The simple ion-by-ion mechanism

In simple ion-by-ion mechanism, Ni-doped CdS thin films are formed from the chemical reaction of dissolved cadmium ions and nickel ions with thiourea molecules in ammonia solutions as shown in equations (3.10) and (3.11) (Hodes, 2002).

$$[Cd(NH_3)_2]^{2+} \longrightarrow Cd^{2+} + 4NH_3 \quad (3.10)$$

($[Cd(NH_3)_2]^{2+}$ dissociate to free Cd^{2+} ions)

$$[Ni(NH_3)_2]^{2+} \longrightarrow Ni^{2+} + 4NH_3 \quad (3.11)$$

($[Ni(NH_3)_2]^{2+}$ dissociate to free Ni^{2+} ions)

$$SC(NH_2)_2 + 2OH^{-1} \longrightarrow S^{2-} + CN_2H_2 + 2H_2O \quad (3.12)$$

(Formation of sulphide ion)

$$Cd^{2+} + S^{2-} + Ni^{2+} \longrightarrow CdNiS_{(S)} \quad (3.13)$$

(CdNiS formation by ionic reaction)

3.2.2 The simple cluster (hydroxide) mechanism

$$nCd^{2+} + nNi^{2+} + 2n(OH)_n^- \longrightarrow [Cd(OH)_2]_n + [Ni(OH)_2]_n \quad (3.14)$$

(Formation of a solid $Cd(OH)_2$ and $Ni(OH)_2$ cluster)

$$[Cd(OH)_2]_n + [Ni(OH)_2]_n + nS^{2-} \rightleftharpoons n\,CdNiS + 4nOH^- \quad (3.15)$$

(Exchange reaction)

3.2.3 The complex decomposition ion-by-ion mechanism

$$SC(NH_2)_2 + Cd^{2+} \rightleftharpoons [SC(NH_2)_2 - Cd]^{2+} \quad (3.16)$$

$$SC(NH_2)_2 + Ni^{2+} \rightleftharpoons [SC(NH_2)_2 - Ni]^{2+} \quad (3.17)$$

$$[SC(NH_2)_2 - Cd]^{2+} + [SC(NH_2)_2 - Ni]^{2+} + 2OH^- \longrightarrow CdNiS + 2CN_2H_2 + 4H_2 \quad (3.18)$$

3.2.4 The complex decomposition cluster mechanism

$$[Cd(OH)_2]_n + [Ni(OH)_2]_n + SC(NH_2)_2 \rightleftharpoons [Cd(OH)_2]_{n-1} + [Ni(OH)_2]_{n-1} + (OH)_2Cd - (OH)_2Ni - S - C(NH_2)_2 \quad (3.19)$$

$$[Cd(OH)_2]_{n-1} + Ni(OH)_2]_{n-1} + (OH)_2Cd - (OH)_2Ni - S - C(NH_2)_2 \rightleftharpoons [Cd(OH)_2]_{n-1}CdS + [Ni(OH)_2]_{n-1}NiS + CN_2H_2 + H_2O \quad (3.20)$$

(This process continues until all the $Cd(OH)_2$ and $Ni(OH)_2$ are converted to CdNiS (Hodes, 2002)).

3.3 Factors Influencing Chemical Bath Deposition Process

Several factors influence film formation when using chemical solution deposition. They include pH of a solution, temperature of reaction bath, nature and concentration of reactants, nature, and concentration of the complexing agent, the spacing of the substrates, and duration of the reaction. These factors don't affect the chemical reaction individually and the final result is due to the cumulative effect of the interdependence of all these factors (Lakshmi, 2001). Different qualities of films are obtained under different conditions in the reaction bath.

3.3.1 The pH of a solution

The pH of a solution is given by:

$$p\mathrm{H} = -\log[H^+] \tag{3.21}$$

Most (but not all) chemical bath deposition reactions take place in basic solutions (pH values of 9–12). The pH of a solution can be stabilized by a buffer. Increasing the pH value of the reaction bath stabilizes the metal complex which reduces the availability of free metal ions. This reduces the rate of reaction leading to higher terminal thickness (Hodes, 2002).

3.3.2 Temperature of the reaction bath

The temperature of the solution influences the dissociation of the complex. When the temperature of the solution is increased, dissociation of the complex is increased. Ions interact more frequently due to an increase in their kinetic energy leading to the decrease or increase of terminal thickness, subject to the extent of super-saturation of the solution. Bath temperature significantly influences the properties of chemically deposited thin films (Nair *et al.*, 1988).

3.3.3 Nature and concentration of reactants and complexing agent

The composition of thin films deposited by the chemical bath is influenced by the nature and the concentration of the metal salts Mn^+ and that of chalcogenide source X (X= S, Se, Te). Precipitation control is achieved by regulating the amount of the metal salts, Mn^+, using a

complexing agent which releases a small quantity (Guillén *et al*., 1998; Lakshmi, 2001) as given in equation (3.22)

$$\frac{[M^{2+}]+[A]}{(M(A)^{2+})} = K_i \qquad (3.22)$$

Equation (3.22) shows that increasing the concentration of the reactants increases the terminal thickness and thin film deposition rate. At a high concentration of reactants, the rate of precipitation is very high, resulting in decreased film thickness.

3.3.4 Concentration of complexing agent

Precipitation control is achieved by controlling the concentration of the metal salts using a complexing agent which releases a small quantity. Using large amounts of complexing ions in a chemical bath reduces the metal ion concentration. This reduces the rate of precipitation, leading to a larger terminal thickness of the film.

3.3.5 Spacing of the substrates

The separation between substrates during film deposition has been noted to influence film formation when using chemical solution deposition in batch production. Film thickness reaches "an asymptotic maximum" with the increase in substrate separation (Reádigos *et al*., 2000). Each substrate has a critical layer of the solution close to it. Around this layer, ionic species have a greater chance of interacting with the film layer. The temperature of the bath, composition of the solution, and duration of deposition affect the critical layer.

3.3.6 Duration of the reaction

The thickness of thin films deposited on a substrate using chemical deposition is highly dependent on the amount of time taken to deposit the layer of the film. The thickness of thin films in which the film formation and kinetics occurs by ion by ion condensation has a linear relationship with deposition time (Ezugwu *et al*., 2009). Higher deposition time results in thicker thin films. Also, thin films of good quality are grown slowly. Thin films grown at a slow growth reaction rate are adherent, thin and hard.

3.3.7 Nature of substrates

The nature of a substrate is important in the adhesion of thin-film and reaction kinetics. Films are more adherent on rough substrates. This is possible because of the greater surface area of contact for every geometric surface area. Glass substrates are usually sensitized with tin chloride solution. Tin chloride hydrolyzes giving nuclei of tin hydroxide/oxide on the surface (Hodes, 2002). Glass slides are usually soaked in acid, i.e., hydrochloric and nitric acid for a day (degreasing), and then washed with deionized (DI) water. This acid treatment is essential because there is the oxidation of halide ions in glass slides thus introducing nucleation centres for film deposition (Oriaku *et al.*, 2008; Ottih *et al.*, 2011). Lattice parameters of substrates and those of the deposited material also influence the rate of deposition, with those matching well recording higher terminal thickness and deposition rates.

3.4. Optical Characterization of Thin Films

Optical experiments present a good means of investigating the properties of semiconductor materials. UV/Vis/NIR spectroscopy enables us to measure transmittance, reflectance, and the absorbance of semiconductor materials. The relationships between these properties and formulas assist us in the analysis of the properties of these materials.

3.4.1 Reflectance (R), transmittance (T), and absorbance (α)

Reflectance is the amount of light or any radiation striking a surface that is reflected. Transmittance is the ratio of light energy transmitted through the material, while absorbance is a measure of the ability of a body to absorb light.

$$\text{Absorbance} = \log\left(\frac{1}{T}\right) \tag{3.23}$$

where T is the transmittance.

3.4.2 Absorption coefficient

It is a measure of the rate of reduction in the intensity of electromagnetic radiation as it goes through a material. Material with a low absorption coefficient does not readily absorb light (Peter *et al.*, 2016). The absorption coefficient is given by equation (3.24);

$$\alpha = -\frac{ln\left(\frac{T}{1-R}\right)}{D_t} \tag{3.24}$$

where α is absorption coefficient, R is reflectance, T is transmittance and D_t is the thickness of the film. Scattering losses and fundamental absorption influence the absorption coefficient. At shorter wavelengths, near the absorption edge, the contribution of the scattering losses is insignificant as compared to that of fundamental absorption (Sta *et al*., 2014).

3.4.3 Bandgap

The bandgap is the difference in energy between the lowest point of the conduction band (conduction band edge) and the highest point of the valence band (valence band edge). The optical band is deduced using Tauc's relationship which is given by equation (3.25) (Park, 2012);

$$(\alpha h\nu) = \mathrm{A}(h\nu - \mathrm{E_g})^m \tag{3.25}$$

where α is the absorption coefficient, $(h\nu)$ is photon energy, A is a constant, E_g the bandgap, and m is a constant, equivalent to 2 for direct gap materials and *1/2* for indirect gap materials. The bandgap is calculated by plotting a graph of $(\alpha h\nu)^2$ against $h\nu$ or $(\alpha h\nu)^{\frac{1}{2}}$ against $h\nu$ for direct or indirect bandgap respectively. The Bandgap is made up of some sub-bands. Sub-band is associated with surface states and surface defects.

3.4.4 The extinction coefficient (k)

The extinction coefficient (k) is deducted from the relation:

$$k = \frac{\alpha\lambda}{4\pi} \tag{3.26}$$

where α is the absorption coefficient, and λ is the wavelength (Park, 2011).

3.4.5 Refractive index

It is the ratio of the speed of light in a vacuum to the speed of light as it goes through a material. It measures how much the speed of light is reduced in the medium. It is calculated using equation (3.14):

$$n = \frac{1+R}{1-R} + \sqrt{\frac{4\mathrm{R}}{(1-\mathrm{R})^2} - \mathrm{k}^2} \tag{3.27}$$

where R is the optical reflectance while k is the extinction coefficient of the films (Mahdi *et al.*, 2009).

3.4.6 Urbach Energy

Along with the absorption coefficient versus photon energy graphs, close to the optical band edge, there exists an exponential part called Urbach tail. Urbach tail appears in low/poor crystalline, amorphous and disordered materials since these materials have localized states which extend in the bandgap. The absorption coefficient is given by equation (3.28) (Marquina *et al.*, 2017).

$$\alpha = \alpha_0 exp\left(\frac{h\upsilon}{E_U}\right) \tag{3.28}$$

From equation (3.28), we can get a straight line equation given by:

$$ln\alpha = ln\alpha_0 + \frac{h\upsilon}{E_U} \tag{3.29}$$

where ($h\upsilon$) is incident photon energy and E_U is the band energy. Urbach energy (band tail width) is then calculated from the gradient of the $ln\alpha$ versus $h\upsilon$ graph. The Urbach (band tail width) energy gives details on the material's structural disorder and localized states in the bandgap (Street, 1991). Doping of semiconductors introduces defects in a material. This is usually confirmed by calculating the Urbach energy of the undoped and the doped materials.

3.5 Hall Effect

When an electric current goes through a material placed in a magnetic field, a potential proportional to the magnetic field and the current is developed across the material in a direction perpendicular to both the current and to the magnetic field. This effect is known as the Hall effect.

Lorentz force, which is a combination of electric force and magnetic force, is the basic principle underlying the Hall Effect. There will be a net transport of carriers along the length of the conductor under the influence of these applied fields (Popovic, 2003).

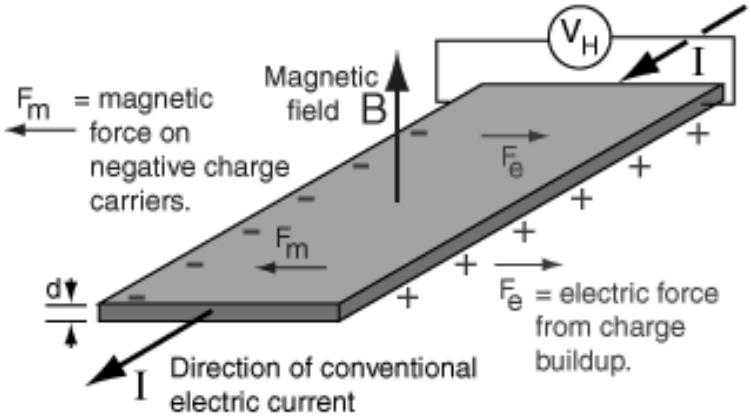

Figure 3. 4: Hall probe configuration for magnetic field measurement (Source: http://hyperphysics.phy-astr.gsu.edu)

Hall Effect measurements system is used to measure electrical properties of a material such as a carrier conductivity type (N or P), concentration (n), carrier mobility (μ), Hall voltage (V_H), Hall coefficient (R_H), Magnetoresistance (R_B) and Resistivity (ρ). Figure 4.4 shows a conducting slab with length l, width w, and thickness t (Popovic, 2003).

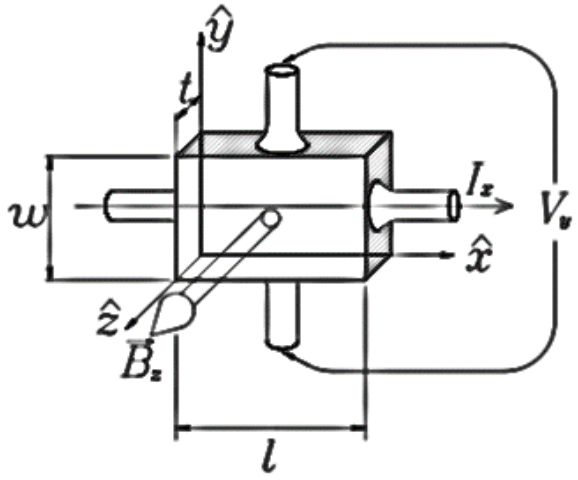

Figure 3. 5: Hall Effect configuration (Source: (Popovic, 2003)

Assuming that the conductor has charge carrier of charge q, charge carrier number density, n, i.e., number of carriers per unit volume, and charge carrier drift velocity v_x when a current I_x flows in the positive x-direction, the current I_x is given by (Popovic, 2003):

$$I_x = J_x wt = nq v_x wt \tag{3.30}$$

where wt is the cross-sectional area of the conductor

The application of an electric field along the length of the conductor causes the flow of current I_x. The material obeys Ohm's law, in case the current is directly proportional to the field (Popovic, 2003).

$$J_x = \sigma E_x \tag{3.31}$$

where σ is the conductivity of the material in the conductor.

Assuming that the conductor is placed in a magnetic field perpendicular to the plane of the slab; the charge carriers will experience a Lorentz force $qv \times B$ that will deflect them toward one side of the slab. Charges accumulate one side of the slab, which creates a transverse electric field E_y that counteracts the force of the magnetic field. When a steady state is reached, there will be no net flow of charge in the y-direction, since the electrical and magnetic forces on the charge carriers in that direction must be balanced (Popovic, 2003). Thus

$$E_y = v_x B_Z \tag{3.32}$$

Where E_y is the electric field (Hall field), and B_z is the magnetic field. The potential difference across the sample (the Hall voltage, V_H) is given by (Popovic, 2003):

$$V_H = -\int_0^w E_y d_y = -E_y w \tag{3.33}$$

We obtain

$$V_H = -\left(\frac{1}{nq}\right)\frac{I_x B_z}{t} \tag{3.34}$$

where $R_H = \frac{1}{nq}$ is known as the Hall coefficient.

$$R_H = \frac{tV_H}{BI_x}(cm^3 C^{-1}) \tag{3.35}$$

It is negative if the charge carriers are negative and positive if the charge carriers are positive. The polarity of V_H determines the sign of the charge carriers. The SI units of the Hall coefficient are [m^3/C].

when Hall-voltage V_H is known, sheet concentration of charge carriers' n_s can be found as(Popovic, 2003):

$$n_s = \frac{IB}{E_e V_H} \tag{3.36}$$

Where I is the current flowing along the sample and E_e is the electron charge. The density of the majority charge carriers n_m and their mobility μ_m can be calculated as (Popovic, 2003):

$$n_m = \frac{n_s}{t} = \frac{IB}{eV_H t}, = \frac{1}{qR_H}(cm^{-3}) \tag{3.37}$$

$$\mu_m = \frac{1}{en_s R_s} = R_H \sigma \tag{3.38}$$

3.6 X-ray Diffraction Analysis

The structure and atomic spacing of materials are determined using X-ray crystallography. X-rays are normally used to study the structure of internal crystalline solids because their wavelengths are in the range of 0.5 - 2.5Å, which is of a similar order of magnitude as the distance between atoms

in solids. Diffraction patterns of the material reveal how the atoms of crystalline solids are arranged. It is dependent on the diffraction of X-ray radiation by the periodic atomic structure (Warren, 1990; Als-Nielsen and McMorrow, 2011).

Diffraction of X-rays is due to the constructive interference of monochromatic X-rays on a crystalline sample. A cathode-ray tube is used to generate X-rays which are then filtered to produce monochromatic X-rays. The X-rays are then collimated to concentrate and then focused toward the sample. The incident rays and the sample interact producing constructive interference (and a diffracted ray) once conditions satisfy Bragg's Law ($n\lambda=2d\ sin\ \theta$), Where n is the order of the diffracted beam, λ is the wavelength of the X-ray beam, d is the distance between adjacent planes of atoms, and θ is the angle of incidence of the X-ray beam (Als-Nielsen and McMorrow, 2011; Dutrow and Christine, 2020 webpage). The interplane spacing (*d-spacings*) is given by:

$$d = \frac{n\lambda}{2\sin\theta} \tag{3.39}$$

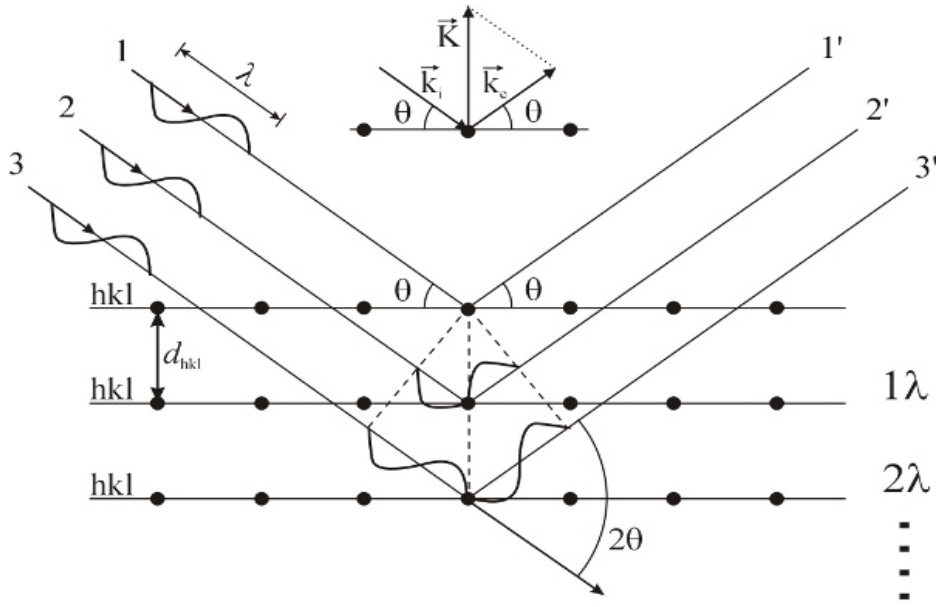

Figure 3. 6: Interaction of incident rays with a material producing constructive interference (Source: https://fys.kuleuven.be)

X-rays that are diffracted are at that point detected, processed, and counted. By scanning the sample over a range of 2θ angles, all possible diffraction directions of the lattice are achieved due to the unsystematic orientation of the powdered material. By converting the diffraction peaks to d-spacings, we can identify the rock crystals in the sample because each rock crystal has a set of

unique d-spacings. Normally, this is done by comparing the d-spacings with standard reference patterns (Warren, 1990).

$$d_{hkl} = \frac{a}{\sqrt{h^2+k^2+l^2}} \tag{3.40}$$

Scherrer formula shown in equation 4.18 gives the full width at half maximum (FWHM) of the peak.

$$FWHM = 0.9\lambda \frac{0.9\lambda}{tcos(\theta_B)} \tag{3.41}$$

Where λ is the wavelength of the X-rays, t is the thickness of the layer and θ_B the Bragg angle of the reflection. FWHM is in radians.

3.7 Energy Dispersive X-ray Fluorescence spectrometer (EDXRF)

Energy Dispersive X-ray Fluorescence (EDXRF) is an X-ray fluorescence technique used for elemental analysis applications (Cox, 1985). The purpose of EDXRF measurements is to study the emission spectra influenced by chemical bonding or to make a quantitative determination of low atomic number elements (Cox, 1985). The schematic of a typical Energy Dispersive X-ray Fluorescence (EDXRF) spectrometer is as shown in Figure 4.1.

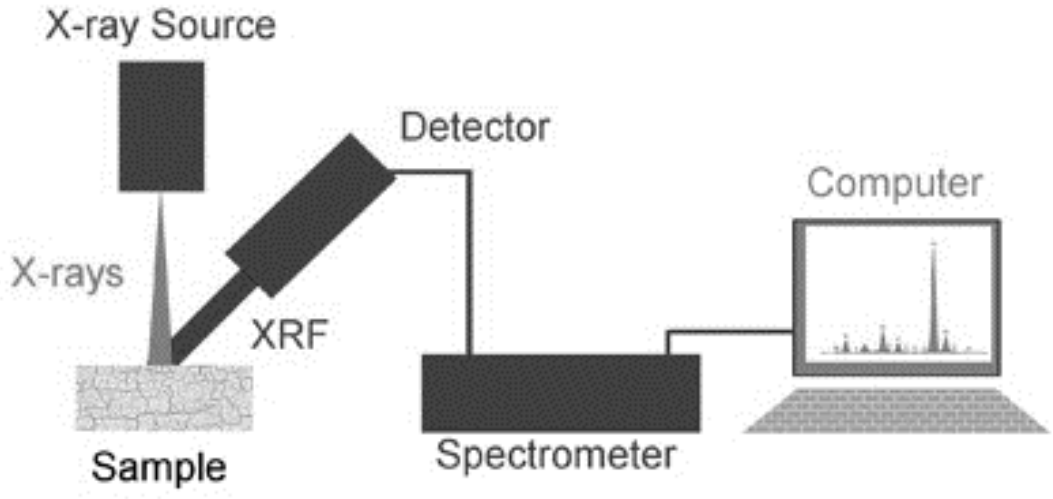

Figure 3. 7: Schematic of a typical Energy Dispersive X-ray Fluorescence (EDXRF) spectrometer

(Source: http://www.horiba.com)

In Energy Dispersive X-ray Fluorescence (EDXRF), low energy “soft’’ X-rays (1-50 keV) are emitted from an X-ray tube. The X-rays enter the sample and cause the atoms in the sample to emit the characteristic signature fluorescence of their distinctive low energy “soft’’ X-rays. These fluorescent X-rays are captured in a detector and counted by a multichannel analyzer. Software is then used to calculate the concentration of each element present in the sample from sodium through uranium.

CHAPTER 4

EXPERIMENTAL PROCEDURES

4.0 Introduction

In this section, the materials and techniques used in this work are presented. Details on substrate cleaning prior to deposition of pure cadmium sulphide and Ni-doped CdS thin films are given. The process of depositing cadmium sulphide and Ni-doped cadmium sulphide thin films using chemical bath deposition technique and subsequent film treatments are described and illustrated. Film characterization in terms of film thickness, reflectance, transmittance, X-ray diffraction, Energy Dispersive X-ray Fluorescence spectrometer (EDXRF), and Hall Effect measurements are also presented.

4.1 Substrate Cleaning and Process of Film deposition

4.1.1 Substrate cleaning

Microscope glass slides obtained locally and FTO conducting glass substrates (F:SnO, 1.5 mm thick) sourced from ForschungZentrum Jullich were used in the deposition of the thin films. Prior to the deposition of the thin films, microscope glass slides were degreased in concentrated nitric acid for one day and then rinsed in deionized (DI) water. This acid treatment was essential to introduce nucleation and epitaxial centres where the films would be embedded. The glass substrates and FTO coated conducting glass were then cleaned in an ultrasonic bath by successively washing using a detergent, ethanol, and distilled water to remove impurities on the surface of the glass substrates. They were then finally dried in the air. The FTO conducting glass used had a sheet resistance of about 8Ω/□.

4.1.2 Chemical bath deposition of Ni-doped CdS thin films

Ni-doped CdS thin films were grown on glass substrates based on the reaction of thiourea and triethanolamine complex of Cd^{2+} given by the general equation (4.1) (Ortega-Borges and Lincot, 1993). Deposition of these films was carried out in 50ml beakers.

$$[Cd(NH_3)_4]^{2+} + SC(NH_2)_2 + 2OH^{-1} \longrightarrow CdS + CN_2H_2 + 4NH_3 + 2H_2 \qquad 4.1$$

Cadmium sulphide and Ni-doped cadmium sulphide films were deposited using different concentrations of Cd^{2+} and Ni^{2+} with triethanolamine complexing agent. The films were prepared from an aqueous solution of 0.1M cadmium chloride ($CdCl_2.2^1/_2H_2O$) (BDH Chemicals Ltd), 1M thiourea (CH_4N_2S) (Sigma–Aldrich), 0.05M nickel (II) chloride ($NiCl_2.6H_2O$) (BDH Chemicals Ltd), 1M triethanolamine (TEA) (Sigma–Aldrich) and 35 wt% ammonia solution (pH regulator). The pH of the reaction bath was ≈11. The amounts of cadmium chloride solution and nickel chloride solution were varied, as shown in Table 4.1. The mixture was stirred well to form a homogenous solution.

Good quality thin films grown by chemical bath deposition are those deposited at low temperatures. To achieve this, the reaction bath containing metal ions and chalcogen ions was placed in an oil bath (placed on a thermostatically controlled plate) maintained at 33 °C, just about 8 °C above the room temperature (25 °C). The slow growth reaction rate at this low temperature will result in the deposition of adherent, thin and hard thin films. Clean glass slides were finally immersed in the aqueous solution as shown in Figure 4.1. This temperature of 33 °C in the reaction bath was attained in about 6 minutes.

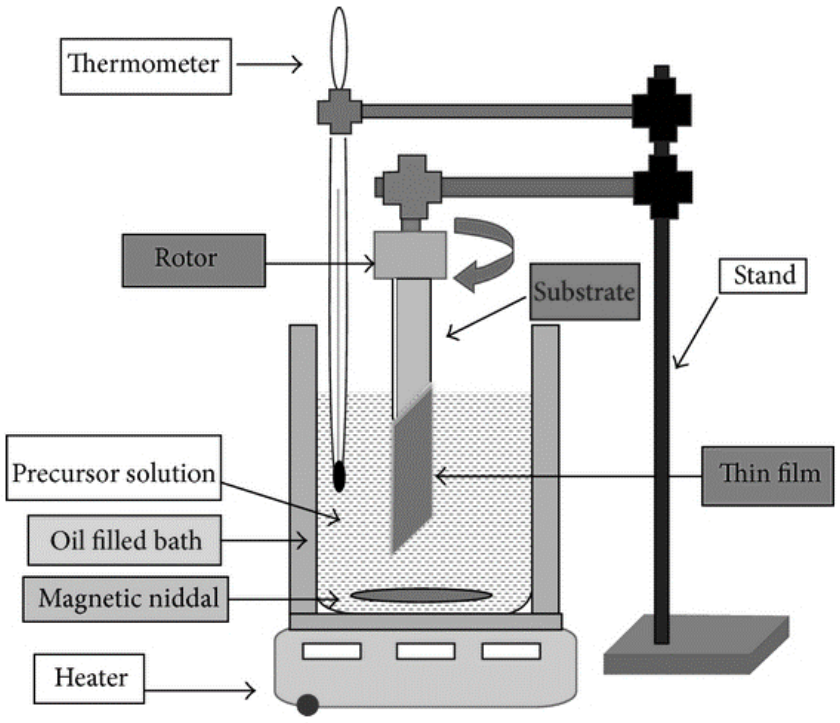

Figure 4. 1: Set up for chemical bath deposition

(Source: (Pawar *et al*., 2011)).

All cadmium sulphide and Ni-doped CdS samples were deposited for 40 minutes. The thin films were then gently rinsed with distilled water to remove the loosely attached particles on the glass substrates. Since the sample holder used in chemical bath deposition the thin films coats on the front and rear side, the rear side of the glass the thin coating was removed using cotton swabs dipped in nitric acid to facilitate transmission and reflection measurements.

Table 4. 1: Amounts of reagents used in the preparation of Ni-doped CdS thin films

Slide No.	$CdCl_2$ (0.1M)		$NiCl_2$ (0.05M)		TEA (Triethanolamine)	NH_3	$SC(NH_2)_2$		Distilled H_2O
	Conc. (wt%)	Vol. (ml)	Conc. (wt%)	Vol. (ml)	Vol. (ml)	Vol. (ml)	Conc. (M)	Vol. (ml)	Vol. (ml)
A1	100.0	5.0	0.0	0.0	2.0	2.5	1.0	2.5	30.0
A3	85.0	4.3	15.0	1.5	2.0	2.5	1.0	2.5	30.0
A4	75.0	3.8	25.0	2.4	2.0	2.5	1.0	2.5	30.0
A5	65.0	3.3	35.0	3.4	2.0	2.5	1.0	2.5	30.0
A3	55.0	2.8	45.0	4.3	2.0	2.5	1.0	2.5	30.0

4.2 Measurement of Thin Film Thickness

The thin film thickness of the as-grown and post-deposition annealed thin film samples of pure cadmium sulphide and Ni-doped CdS with varying nickel concentrations were determined using SCOUT software which is based on the theory by Drude and Kim ("SCOUT software," 2001) and calculation performed in the wavelength range from 200 nm – 2500 nm. The SCOUT™ software was used to analyze the optical spectra by computer simulation. In this research work, reflectance and transmittance spectra were simultaneously fitted. Model calculations were based on the Drude model (for free carriers), harmonic oscillator, Kim oscillator, OJL interband transition model, and Tauc-Lorentz interband transition model ("SCOUT manual," 2001).

4.3 Annealing of the Deposited Thin Film

The doped and undoped films (samples) were annealed in a tube furnace (Daihan Labtech Co., Ltd) for 30 minutes in air at a pre-set temperature of 150 °C, 250 °C, 350 °C, and 450 °C. Thereafter, allowed to cool to room temperature before being removed from the tube furnace. The heating rate was maintained at 30 °C per minute.

4.4 Optical Characterization of Thin Films

4.4.1 Reflectance and transmittance measurements

The optical properties: reflectance and transmittance, in the range of 200 nm-1500 nm were measured by UV-VIS-NIR spectrophotometer (SolidSpec-3700 DUV, Shimadzu Corporation) and used to calculate other optical and solid-state properties like bandgap (E_g), refractive index (n), extinction coefficient (k) and absorption coefficient (α) as indicated in the sections below.

(i) Bandgap

The optical band was determined using Tauc's relationship which is given by equation (4.2) (Park, 2012);

$$(\alpha h\nu) = \mathrm{A}(h\nu - \mathrm{E_g})^m \tag{4.2}$$

where α is the absorption coefficient, ($h\nu$) is photon energy, A is a constant, Eg the bandgap, and m is a constant, equivalent to 2 for direct gap materials and $\frac{1}{2}$ for indirect gap materials. The bandgap was calculated by plotting a graph of $(\alpha h\nu)^2$ against $h\nu$ or $(\alpha h\nu)^{\frac{1}{2}}$ against $h\nu$ for direct or indirect bandgap respectively.

(ii) The extinction coefficient (k)

The extinction coefficient (k) was deduced from the relation:

$$k = \frac{\alpha\lambda}{4\pi} \tag{4.3}$$

where α is the absorption coefficient, and λ is the wavelength (Park, 2011).

(iii) Refractive index

This is the ratio of the speed of light in a vacuum to the speed of light as it goes through a material. It measures how much the speed of light is attenuated in the medium. The refractive index was calculated using equation (4.4):

$$n = \frac{1+R}{1-R} + \sqrt{\frac{4\mathrm{R}}{(1-\mathrm{R})^2} - \mathrm{k}^2} \tag{4.4}$$

Where R is the optical reflectance while k is the extinction coefficient of the thin films (Mahdi *et al.*, 2009).

(iv) Urbach Energy

The absorption coefficient is given by equation (4.5) (Marquina *et al.*, 2017).

$$\alpha = \alpha_0 exp\left(\frac{h\upsilon}{E_U}\right) \tag{4.5}$$

From equation (3.28), we can get a straight line equation given by:

$$ln\alpha = ln\alpha_0 + \frac{h\upsilon}{E_U} \tag{4.6}$$

where ($h\upsilon$) is incident photon energy and E_U is the band energy. The Urbach energy (band tail width) was then calculated from the gradient of the $ln\alpha$ versus $h\upsilon$ graph.

4.5 Polarity of charge carriers

The Hall voltage and current measurements were carried out using the setup shown in Figure 4.2. The Magnetic field intensity (B) was measured using a digital flux/gauss meter while the direct current power supply was used to measure the supplied electric current (I) and the hall voltage (V_H). The Hall voltage and current values were recorded at the magnetic field of 3G. Measurements were carried out at room temperature (25 ℃).

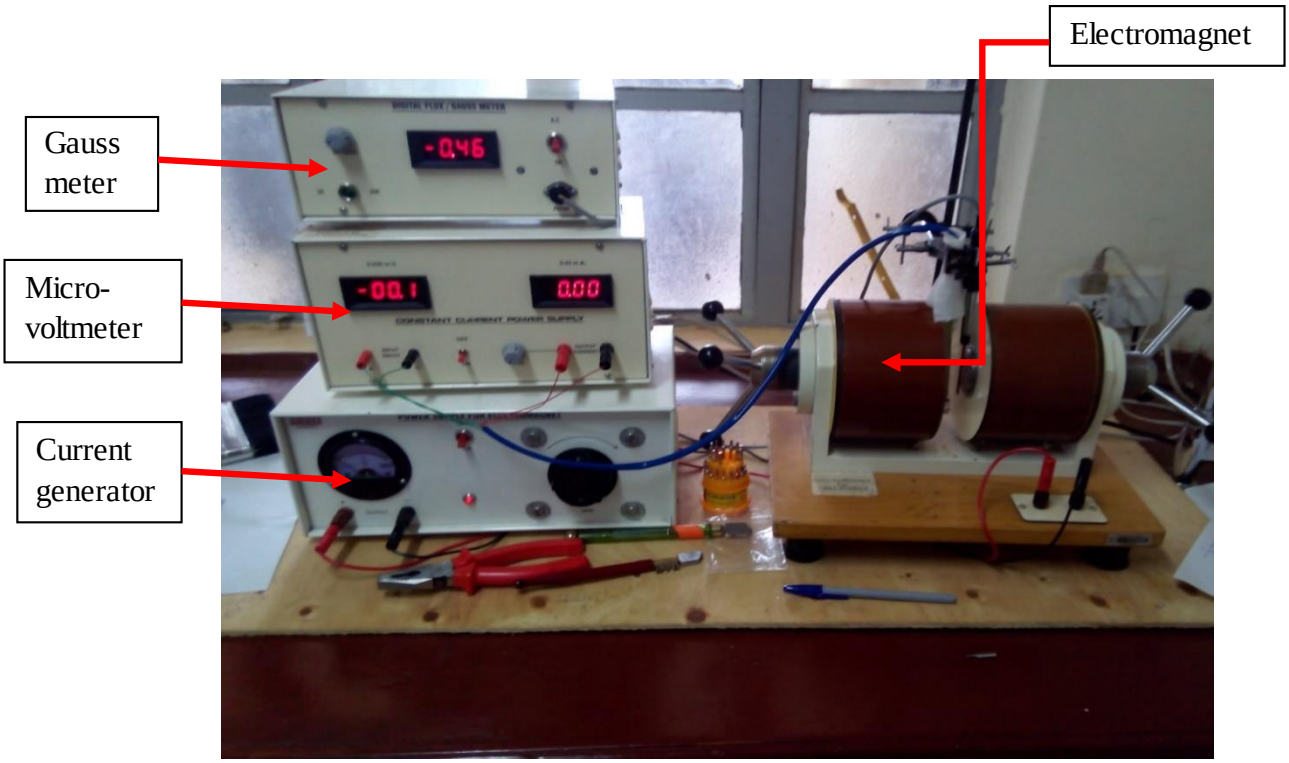

Figure 4. 2: Hall Effect set up

4.6 Structural analysis

The structure of the thin films was analyzed by Grazing incidence x-ray diffraction using an advanced X-ray diffractometer (Bruker D8) with Cu-Kα (1.5405 Å) radiation for thin films analysis (LMC). The instrument is equipped with a 9-fold sample changer. Measurements were carried out in the 2θ range from 10° to 70° with an increment of 0.02° and step time of 7s at an angle of incidence of 0.5°. Identification of the diffraction peaks was made using the JCPDS (Joint Committee on Powder Diffraction Standards) database. The size of CdS nanoparticles was calculated using Scherrer's equation [4.7] (Monshi *et al.*, 2012).

$$D_P = \frac{K\lambda}{\beta Cos\theta} \qquad (4.7)$$

where, D_p = Average crystallite size, K= 0.94, β = Line broadening in radians, θ = Braggs angle and λ = X-Ray wavelength. (Monshi *et al.*, 2012).

4.7 Elemental analysis

The Rigaku NEX CG spectrometer was used for the elemental analysis of undoped and Ni-doped CdS thin films. Table 4.2 shows the experimental conditions used for the measurement of the samples. The measurements were done in the air.

Table 4. 2: Experimental conditions used for the measurement of the samples.

Condition	Secondary target	Tube Voltage	Tube current (mA)	Measured time (sec)
Mo	Mo	50	Auto	50
Cu	Cu	50	Auto	50
RX9	RX9	25	Auto	50
Si	Si	25	2.00	50

CHAPTER 5

RESULTS AND DISCUSSIONS

5.0 Introduction

In this chapter, a detailed presentation of all the results obtained using various characterization techniques for Ni-doped CdS thin films prepared using chemical bath deposition is made. The chapter begins with a structural and compositional analysis of Ni-doped CdS thin films. The influence of Ni^{2+} concentration and annealing temperature on the optical characteristics, the polarity of charge, and Urbach energies of Ni-doped CdS thin films is described. Results from XRD spectroscopy were used to explain the observed trends in the optical and structural properties of the films

5.1 Compositional Analysis

EDXRF was used to identify the elemental composition of the deposited thin films. Figure 5.1 shows the EDXRF spectra of microscope glass slides substrate used to deposit CdS:Ni thin films.

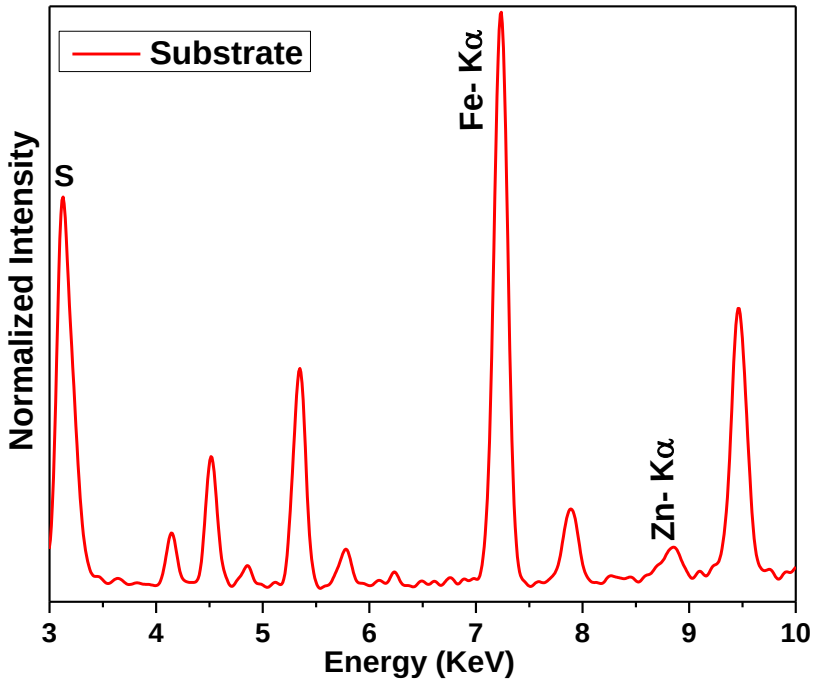

Figure 5. 1: EDXRF spectra of the substrate used to deposit the samples for Elemental analysis

Microscope glass slides are usually made of glass such as borosilicate glass or soda-lime glass. Borosilicate glass (pyrex) was used as it is heat-shock resistant. Borosilicate glass is made up of silica, boric oxide, sodium oxide, and alumina.

Figure 5.2 shows the EDXRF spectra of as-grown Ni-doped CdS thin films doped at different weight percentages. The undoped sample is shown with a blue legend at 0 wt% doping, then the subsequent spectra are for CdS doped with nickel at 15 wt%, 25 wt%, 35 wt%, and 45 wt%.

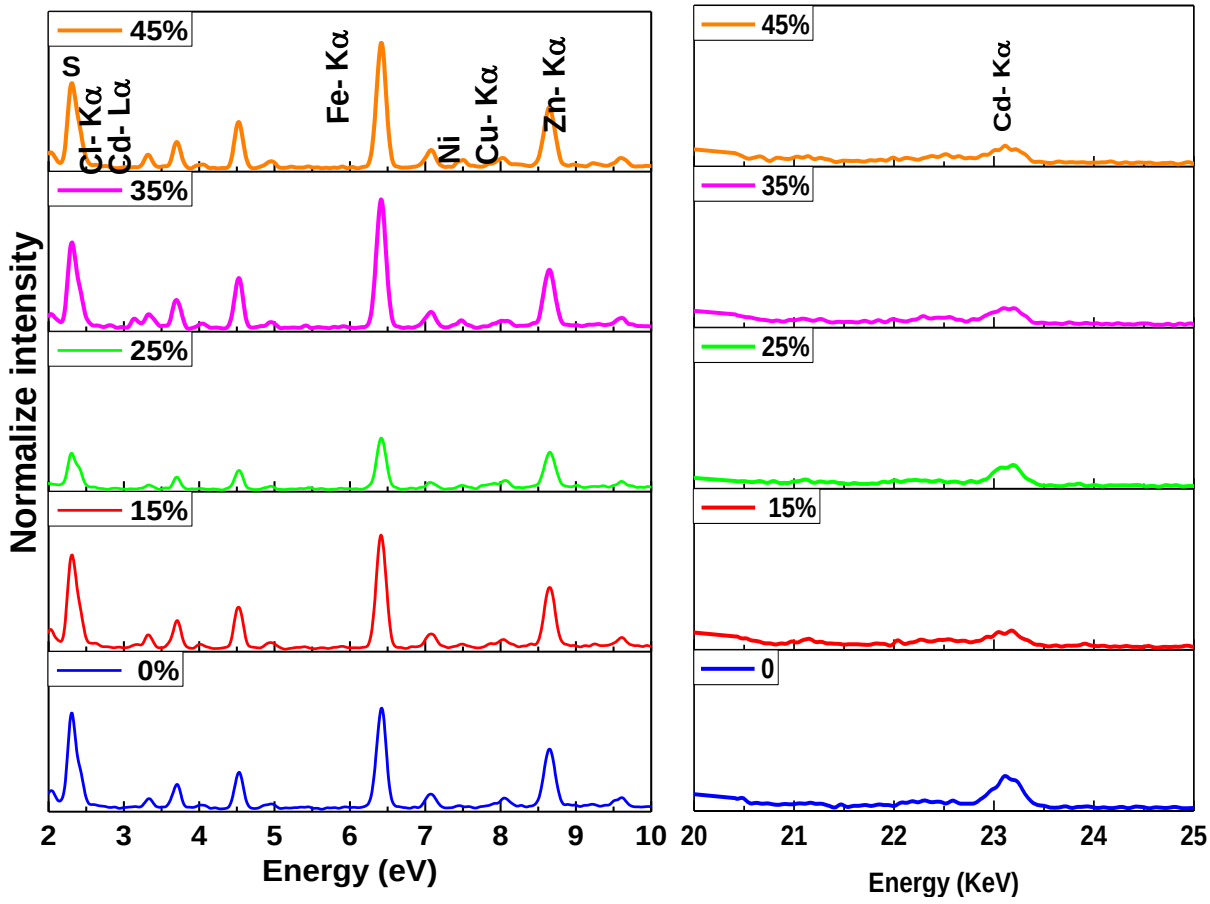

Figure 5. 2: EDXRF spectra of as-grown undoped and Ni-doped CdS thin films with concentrations of nickel from 0 wt% to 45 wt%

The characteristic $K\alpha_{1,2}$ and L_α peaks in the spectra reveal the presence of cadmium, nickel and sulphur at (L_α 3.133 & K_α 23.173) KeV, K_α 7.480 KeV and 2.309 KeV, respectively. From Figure 5.2, it is observed that the intensity of L_α 3.133 & K_α 23.173 peaks (X-ray energies of Cadmium) decreased as the nickel concentration was increased, while the intensity of K_α 7.480 (X-ray energy of Nickel) increased as the nickel concentration was increased. The increase in the intensity of Kα

7.480 (X-ray energy of Nickel) as the nickel concentration was increased confirms that more Ni^{2+} ions were successfully incorporated into the CdS structure with increasing nickel content.

5.2 Structural Analysis

5.2.1 Influence of Ni^{2+} concentration on CdS thin films

The as-grown pristine and Ni-doped CdS thin films were yellow. On further doping, the yellow colour of Ni-doped CdS changed to light yellow with increased Ni^{2+} ions from 0 wt% to 45 wt%. Figure 5.3 shows the X-ray diffraction patterns of as-grown Ni-doped CdS thin films synthesized with varying metal ions (Cd^{2+} and Ni^{2+}) concentrations in the starting solution.

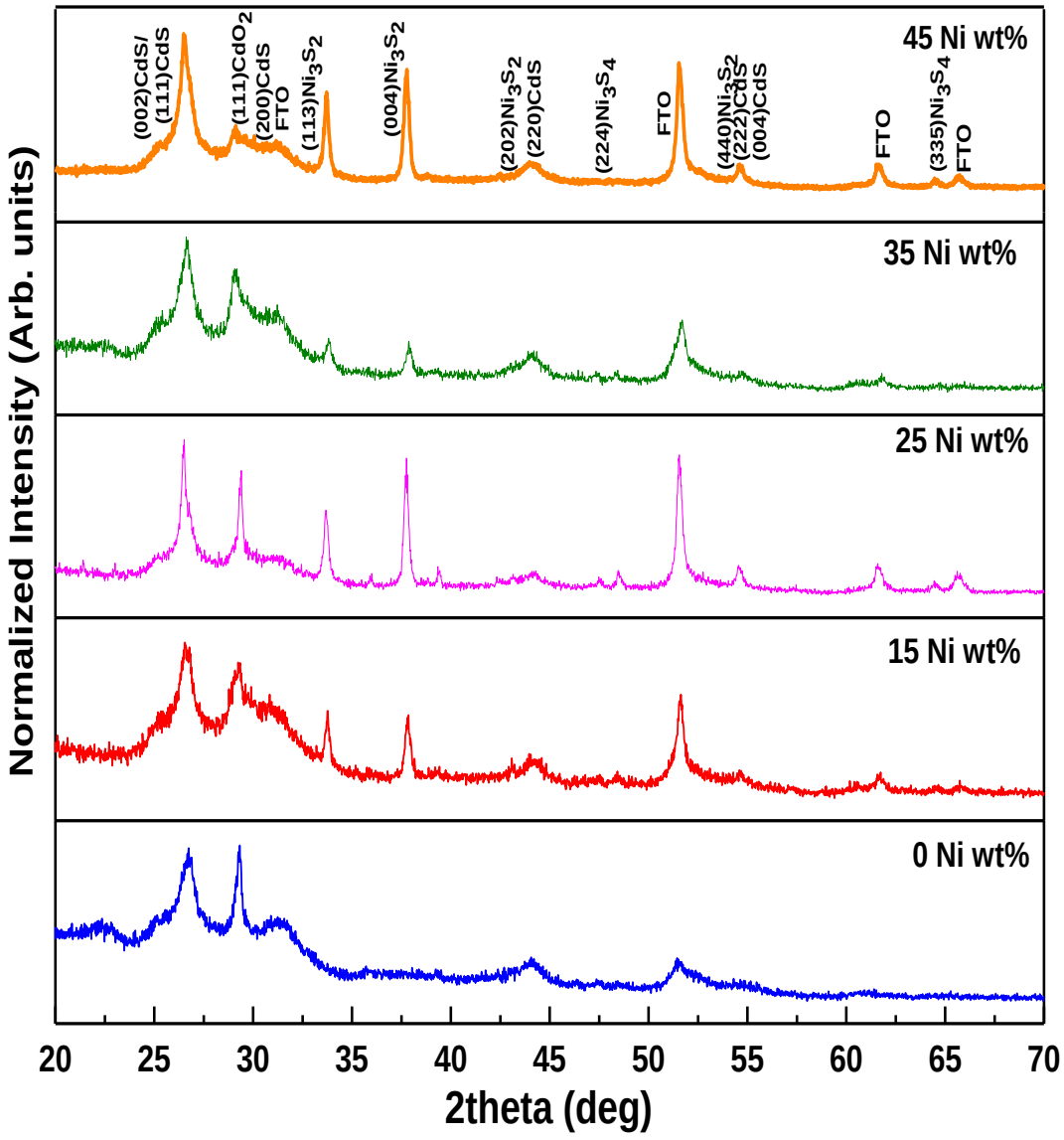

Figure 5. 3: X-ray diffraction pattern of as-grown Ni-doped CdS thin films obtained at various nickel concentrations

From Figure 5.3, it is observed that the diffraction patterns of the films have multiple diffraction peaks indicating that the films are polycrystalline with preferred orientation along (111) direction. The as-grown thin films exhibit a mixed-phase lattice structure (cubic and hexagonal structures). The 2θ values of cubic phased CdS diffraction peaks were observed at 26.499, 30.820, 43.941, and 54.579, respectively which match with reflections from (111), (200), (220), and (222) planes for CdS thin films.

The hexagonal-based diffraction peaks (002) and (004) were also observed at 2θ values of 26.52 and 54.66, respectively in the as-grown films. Cubic-phased nickel sulphide (Ni_3S_2) peaks were seen at 31.419, 37.98, 44.378, 47.381, 54.699, and 64.479 which correspond to reflections from (113), (004), and (202), (224), (440), and (335), planes respectively.

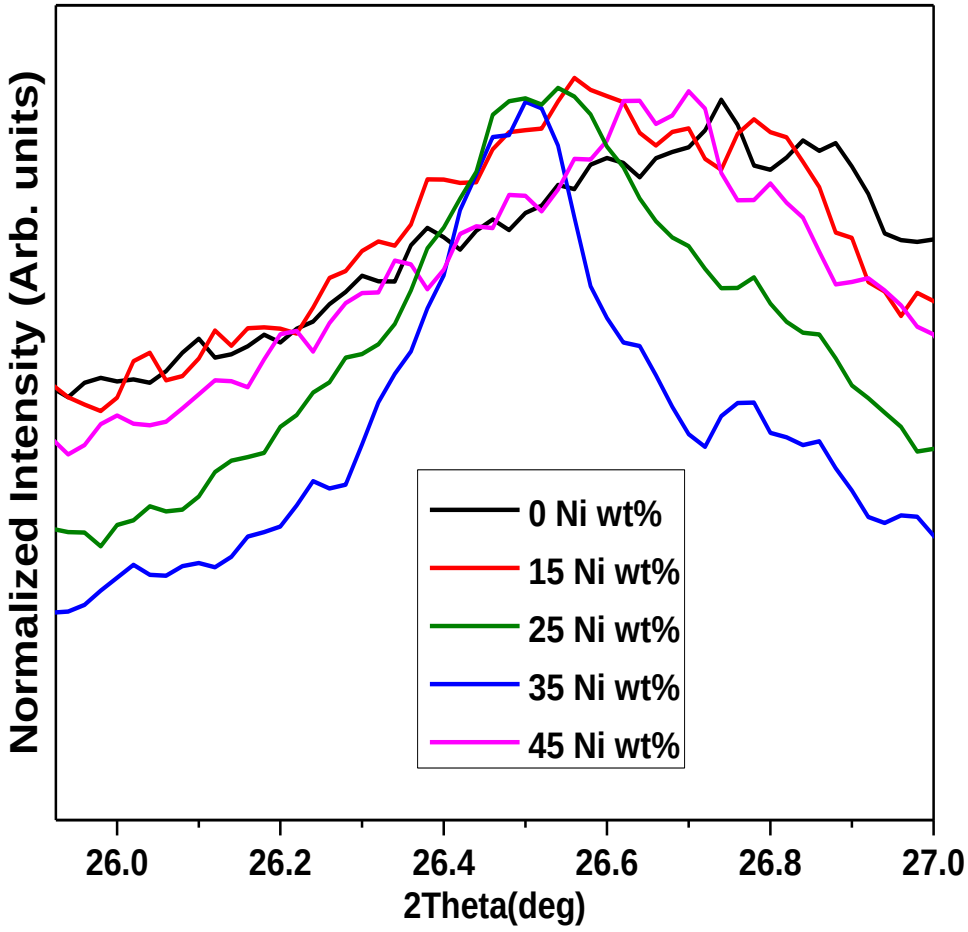

Figure 5. 4: GIXRD pattern of as-grown Ni-doped CdS thin films showing peak (111) slightly shifting to the lower angle with increasing Ni^{2+} concentration

It was further observed that that the peak (111) slightly shifts to the lower angle with increasing Ni^{2+} concentration (Figure 5.4) indicating that Ni ions substitute Cd ions in the CdS lattice owing to the small ionic radius (0.069 nm) as compared to that of Cd^{2+} (0.097 nm) and higher electronegativity (1.91 Pauling) as compared to that of Cd^{2+} (1.61 Pauling). The peak may be as a result of compressional micro-stress or elongational strain in the CdS lattice, due to the difference in ionic radii of Cd^{2+} ion and the Ni^{2+} ion. The XRD patterns in Figure 5.4 confirm that Ni^{2+} ions successfully incorporated into the CdS structure.

5.2.2 Influence of post-deposition annealing treatments on CdS:Ni thin films

The XRD patterns of 25 wt% Ni-doped CdS thin films annealed in air at various temperatures for 30 minutes are shown in Figure 5.5. From the patterns, we observe that the intensity of the peaks changes with annealing temperature, indicating changes in crystallinity of the films as the annealing temperature was varied. After annealing the 25 wt% Ni-doped CdS films in the air at 250 °C, the peaks become sharper than the as-grown 25 wt% Ni-doped CdS, with the films retaining the CdS cubic structure as shown in Figure 5.5. The increased peak sharpness after annealing the thin films is attributed to the reorientation of the particles when samples are annealed while the strain in the film is reduced. The composition of the films is not affected when the films are annealed at temperatures below 250 °C.

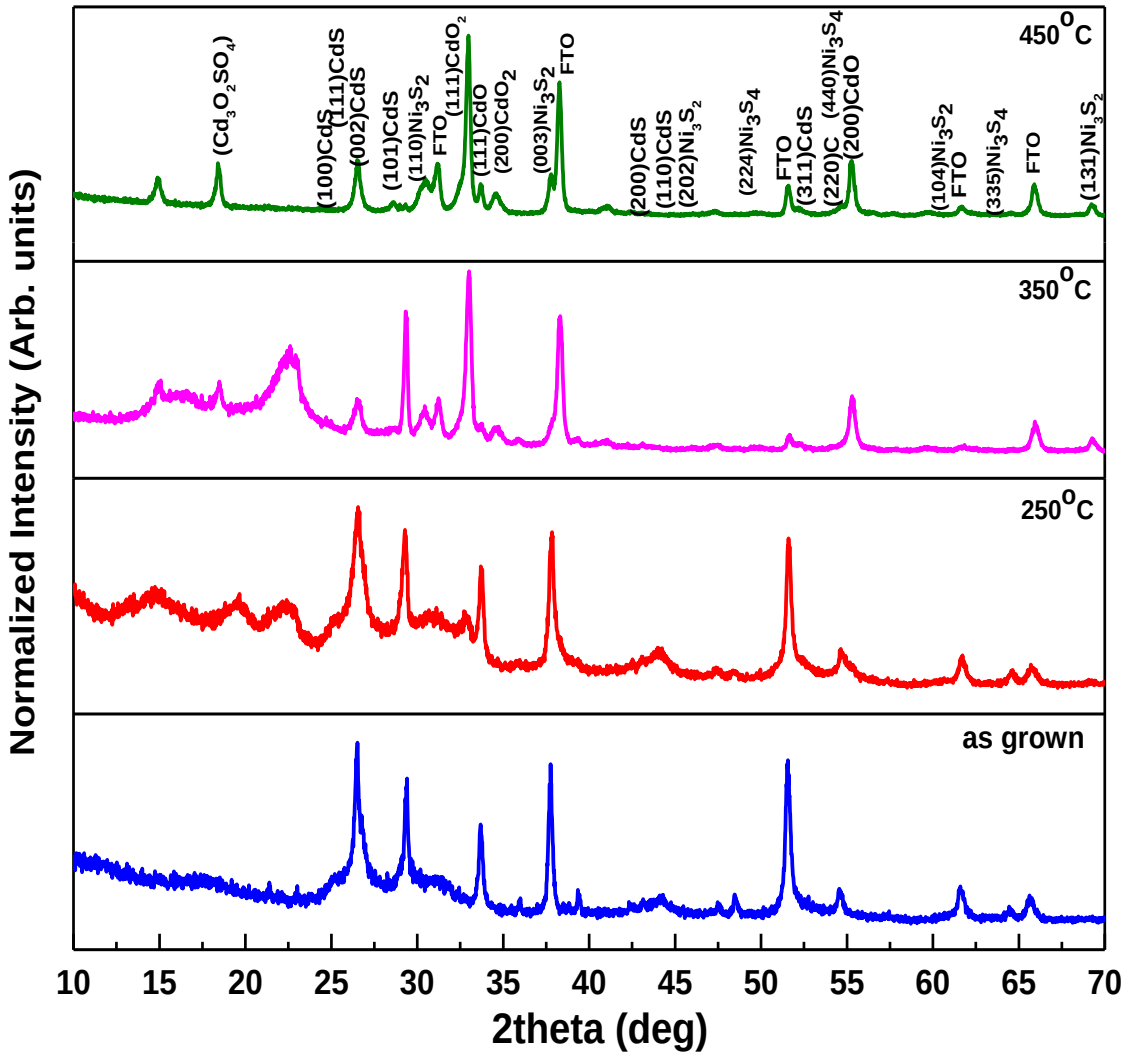

Figure 5. 5: X-ray diffraction pattern of 25wt% Ni-doped CdS obtained at various annealing temperatures.

Diffraction peaks due to (100), (002), (101), and (110) planes of hexagonal phased CdS were observed in thin films annealed at 350 ℃ and 450 ℃ at 2θ values 24.84, 26.52, 28.30, and 43.72 as shown in Figure 5.5. Annealing of undoped and Ni-doped CdS at 350 ℃ and 450 ℃ thin films results in re-crystallization and lattice transition from mixed-phase (cubic and hexagonal) to hexagonal phase. The hexagonal CdS preferred orientation is along the (002) direction. The hexagonal phase of CdS is more stable than the cubic phase (Nair *et al.*, 2001).

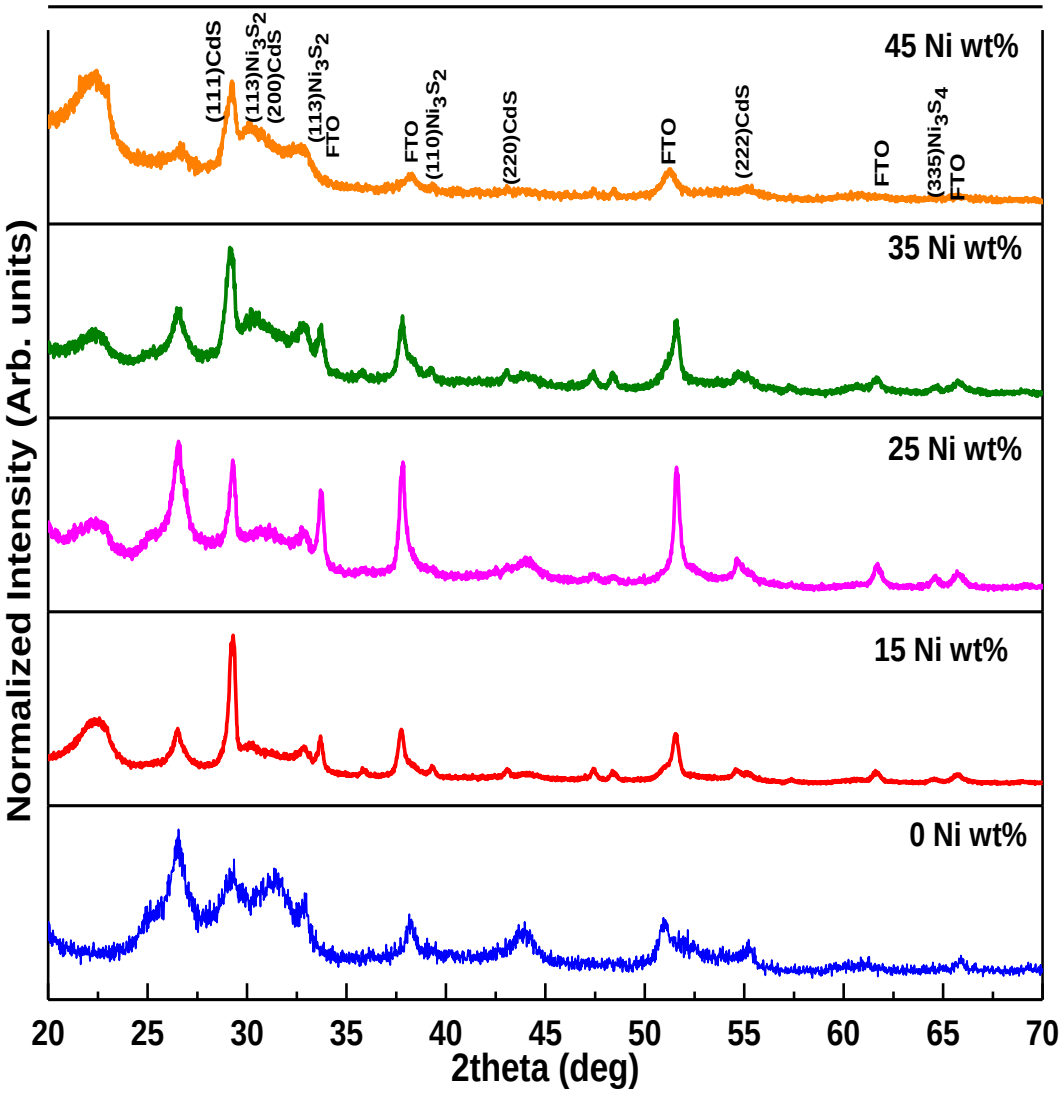

Figure 5. 6: X-ray diffraction pattern of Ni-doped CdS thin films annealed at 250 °C

Also, at these annealing temperatures (350 °C and 450 °C), there is a partial conversion of CdS to CdO. 2θ values of the CdO and CdO_2 diffraction peaks were observed at 29.18, 33.72, 38.28, 48.38, 55.26, and 65.88 which correspond to reflections from (111), (200), (200), (220), (220), and (311). When the undoped and Ni-doped samples were annealed at 350 °C and 450 °C in air, some of the CdS is oxidized to form CdO as shown in equation (5.1). Similar results have been obtained by Nair *et al.*, 2001.

$$CdS + \frac{1}{2}O_2 \longrightarrow CdO + 8S \qquad (5.1)$$

Also, some $Cd(OH)_2$ precipitates in the film during deposition. When the films are annealed, $Cd(OH)_2$ changes to CdO releasing water vapour that causes further oxidation.

Figures 5.7 and 5.8 show the XRD patterns of undoped and Ni-doped CdS thin films annealed in air at 350 ℃ and 450 ℃, respectively. At each of these annealing temperatures, the XRD patterns for all the samples with varying nickel concentrations are similar. The intensity of CdS peaks reduced while those of CdO and CdO_2 increased with an increase in annealing temperature (from 350 ℃ to 450 ℃).

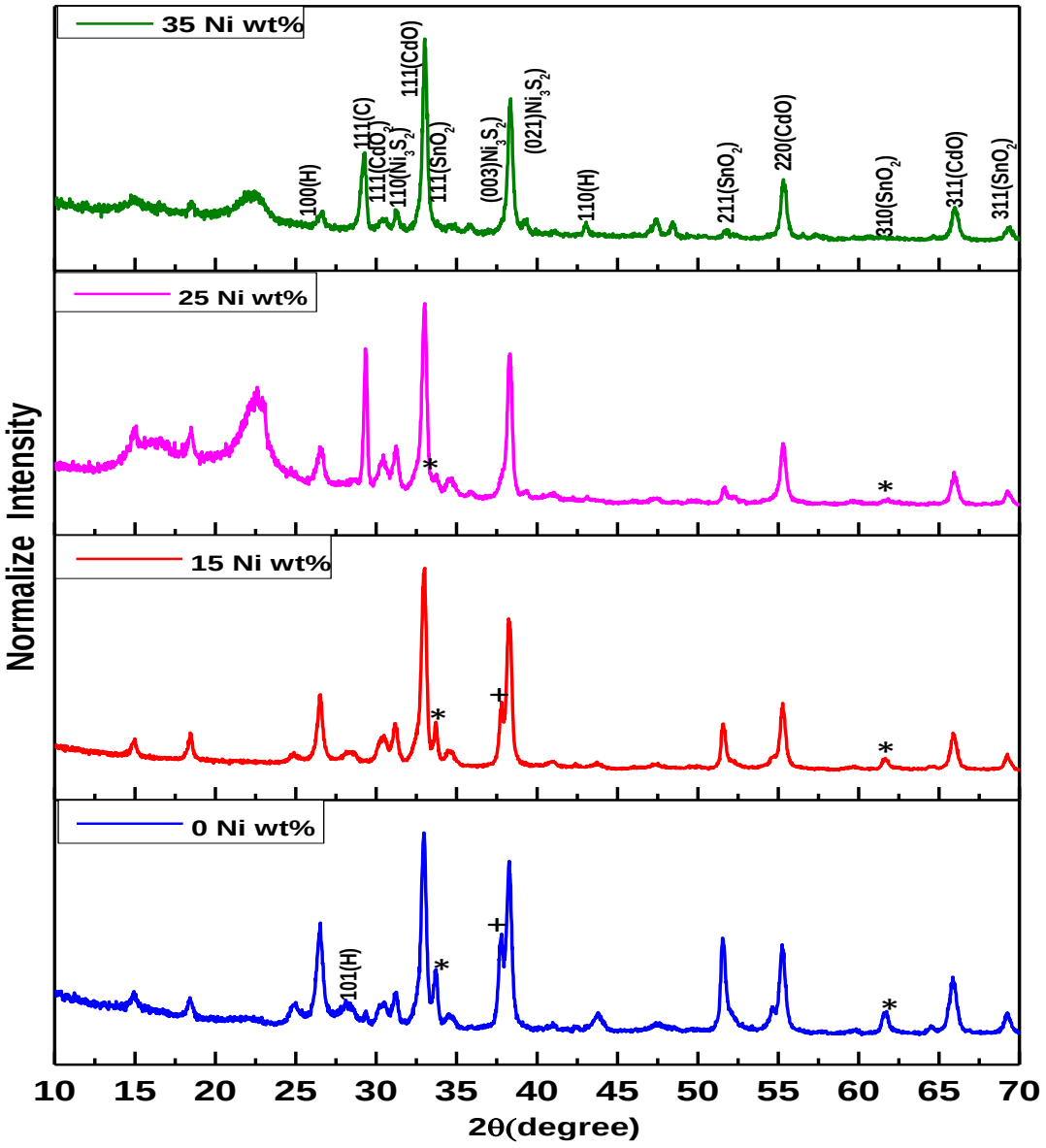

Figure 5. 7: X-ray diffraction pattern of undoped and Ni-doped CdS annealed at 350 ℃.

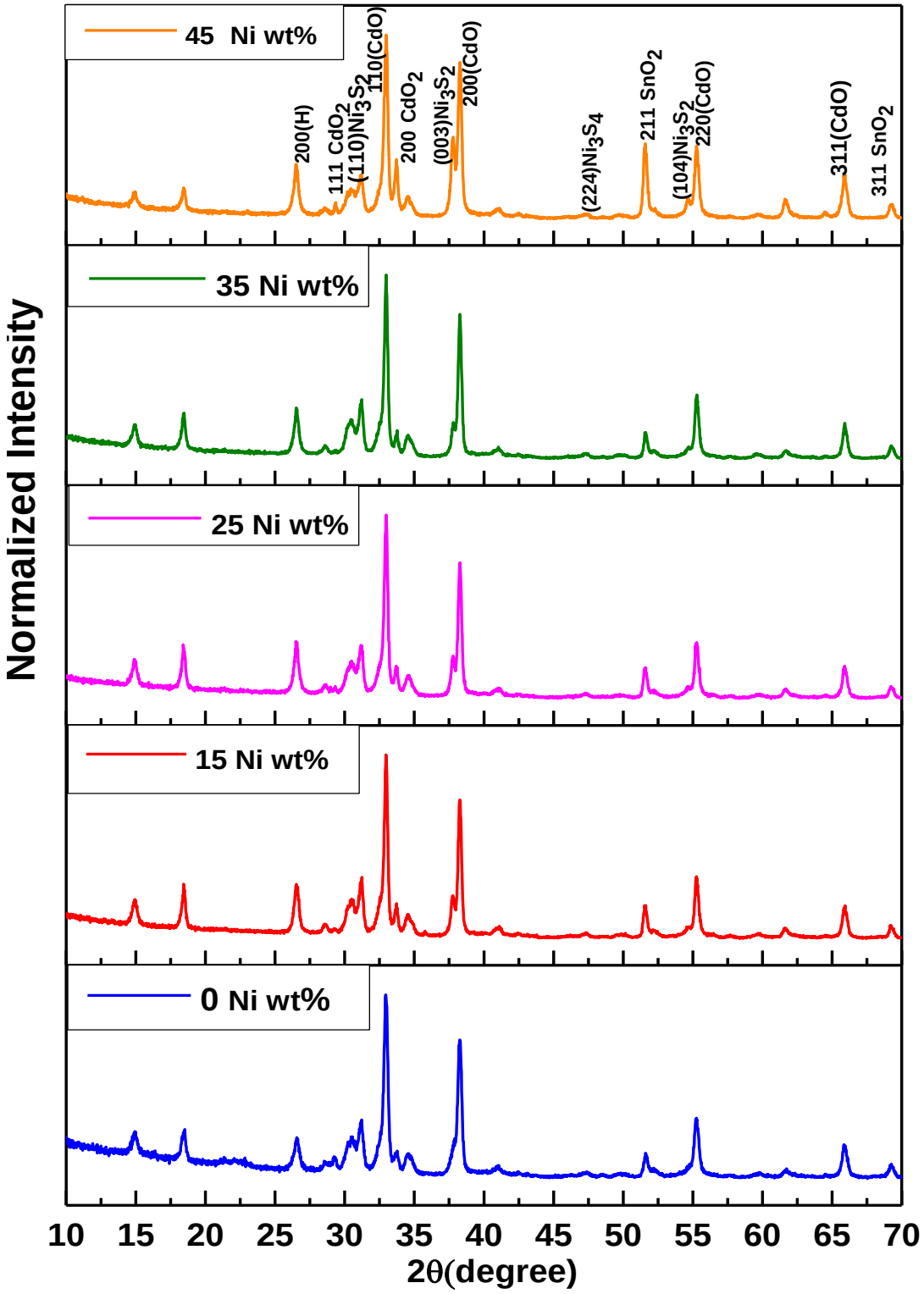

Figure 5. 8: X-ray diffraction pattern of Ni-doped CdS annealed at 450 °C

5.2.3 Crystallite size

The Scherrer equation, (equation (5.2)) was used to calculate the crystallite grain size of Ni-doped CdS thin films annealed at various temperatures.

$$D_P = \frac{K\lambda}{\beta Cos\theta} \tag{5.2}$$

where, D_p = Average crystallite size, K= 0.94, β = Line broadening in radians, θ = Braggs' angle and λ = X-Ray wavelength.

The shape factor of K ranges from 0.62 - 2.08 and is usually taken as about 0.94 (Monshi, *et al.*, 2012).

Table 5. 1: Calculated crystallite grain size of the as-prepared 25 wt% Ni-doped thin films

As-prepared, 25 wt% Ni-doped CdS						
2-Theta	Phase ID	*h*	*k*	*l*	FWHM	Crystallite size (nm)
26.50	CdS	1	1	1	0.41	20.99
29.36	CdO	1	0	1	0.32	26.71
33.70	CdO_2	2	0	0	0.29	29.68
47.52	Ni_3S_4	2	2	4	0.40	22.54
54.58	CdS	2	2	2	0.37	25.02
64.48	Ni_3S_4	3	3	5	0.35	27.78
Average crystallite size = 26.76 nm						

Table 5. 2: Calculated crystallite grain size of the 25wt% Ni-doped thin films annealed 250 ℃

25 wt% Ni-doped CdS annealed at 250 ℃						
2-Theta	Phase ID	*h*	*k*	*l*	FWHM	Crystallite size (nm)
26.58	Ni_3S_4	2	2	0	0.60	14.16
29.30	CdS	1	0	1	0.33	25.90
32.94	CdO	1	1	1	0.5	17.3
33.72	CdO_2	2	0	0	0.26	33.33
37.84	Ni_3S_4	4	0	0	0.38	22.89
44.10	CdS	2	2	0	0.73	12.24
47.42	S	3	2	1	0.39	23.05
54.70	Ni_3S_4	4	4	0	0.59	15.94
61.70	Ni_3S_4	6	2	0	0.44	21.76
65.74	CdO	3	1	1	0.50	19.67
Average crystallite grain size = 20.62 nm						

Table 5.3: Calculated crystallite grain size of 25 wt% Ni-doped CdS thin films annealed at 350 ℃

25 wt% Ni-doped CdS annealed at 350 ℃						
2-Theta	Phase ID	*h*	*k*	*l*	FWHM	crystallite size (nm)
26.52	CdS	1	1	1	0.46	18.52
31.24	Ni_3S_4	1	1	3	0.26	32.62
33.00	CdO	1	1	1	0.385	22.47
38.30	CdO	2	0	0	0.38	23.1
52.26	CdS	3	1	1	0.96	9.64
55.32	Ni_3S_2	3	0	0	0.42	22.51
69.28	Ni_3S_2	1	3	1	0.42	24.24
Average crystallite grain size = 21.87 nm						

Table 5. 4: Calculated crystallite grain size of 25wt% Ni-doped CdS thin films annealed at 450 ℃

25 wt% Ni-doped CdS annealed at 450 ℃						
2-Theta	Phase ID	*h*	*k*	*l*	FWHM	crystallite size (nm)
26.54	CdS	0	0	2	0.39	22.08
31.18	Ni_3S_2	1	1	0	0.36	23.72
32.96	CdO	1	1	1	0.35	24.85
37.78	Ni_3S_2	0	0	3	0.37	23.44
38.28	CdO	2	0	0	0.32	27.18
41.16	Ni_3S_4	2	2	4	0.53	16.68
54.66	Ni_3S_2	1	0	4	0.60	15.56
55.26	CdO	2	2	0	0.38	24.97
65.88	CdO	3	1	1	0.42	23.65
Average crystallite grain size = 22.46 nm						

The crystallite grain size of the as-grown and those annealed at 250 ℃, 350 ℃, and 450 ℃ were in a range of 20.99 nm-34.59 nm, 12.24 nm-33.33 nm, 9.64 nm-32.62 nm, and 22.08 nm-27.18 nm respectively as shown in Tables 5.1, 5.2, 5.3, and 5.4. Their average crystallite grain size 26.76 nm, 20.62 nm, 21.87 nm, and 22.46 nm, respectively. Similar results were observed on 0 wt%, 35 wt%, and 45 wt% Ni-doped CdS thin films, as shown in figures 6.1-6.15 (Appendix section). The crystallite grain size increases with annealing temperature. This occurs due to a decrease in surface energy resulting in grain boundary enlargement, and as a result of that, the particle size increases as a function of the temperature (Gaber *et al.*, 2014; Akbarnejad *et al.*, 2017).

5.3 Optical Analysis

5.3.1 Transmittance and reflectance

(a) Effect of nickel doping on Transmittance and reflectance of CdS thin films

The variation of optical transmittance and reflectance as a function of wavelength was recorded for both as-grown and annealed undoped and Ni-doped CdS layers in the wavelength range 250 nm - 2500 nm. Optical transmittance and reflectance spectra of as-grown undoped and Ni-doped CdS thin films are shown in Figure 5.9.

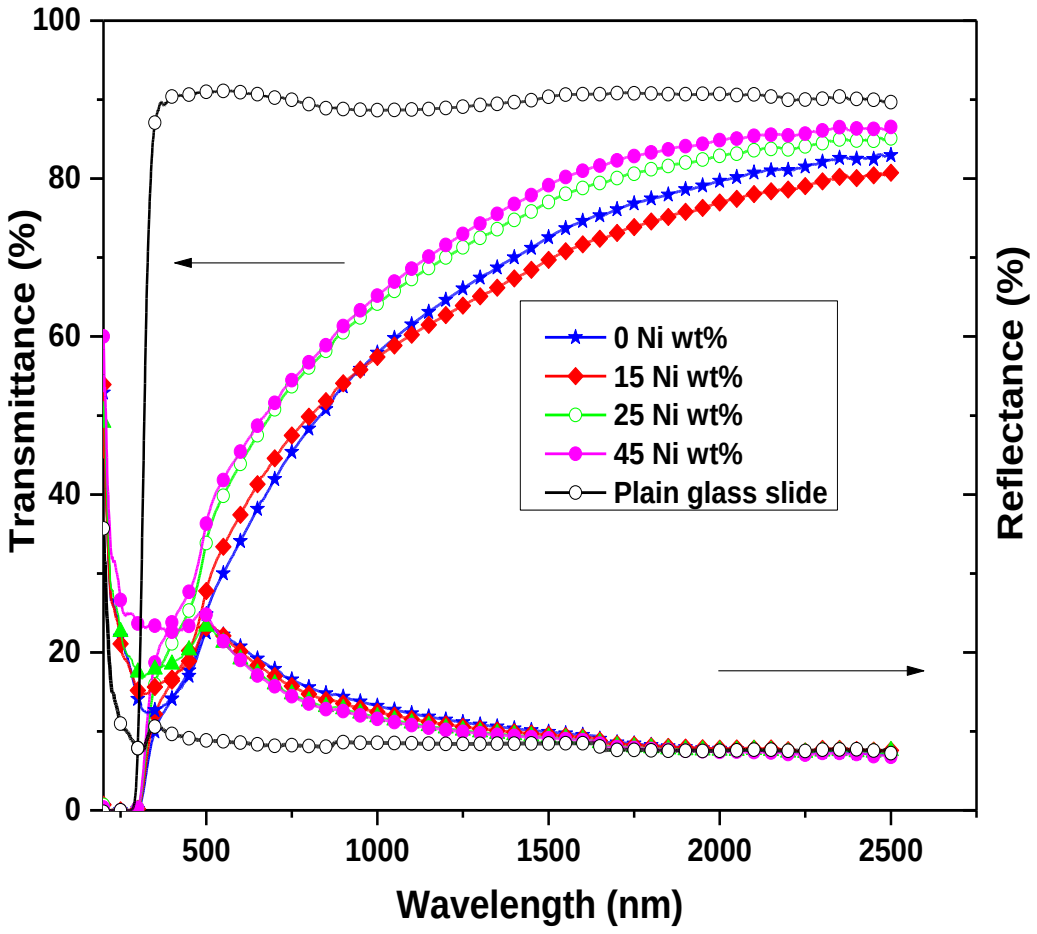

Figure 5. 9: Transmittance and reflectance spectra of as-grown undoped and Ni-doped CdS thin films synthesized by chemical bath deposition

From the transmittance spectra, it is evident that the transmittance of the thin films increased as dopant concentration increased. Ni-doping CdS films also led to the decrease of reflectance for all wavelengths. The increase in transmittance and the subsequent decrease in reflectance of Ni-doped CdS as the dopant concentration increases may be a result of an increase in the crystallinity of the thin films with increasing dopant concentration. This is evidenced by the XRD patterns of the as-grown Ni-doped CdS thin films shown in Figure 5.3. This indicates that the higher the nickel concentration the better the crystallinity of the thin film samples. Increased crystallinity of thin films enhances the light transmission thereby making the films a good candidate for solar cell applications as window/buffer layers.

The Ni-doped CdS thin films are highly transparent in the near infra-red regions (700 nm – 2500 nm). In the visible region (400 nm – 700 nm), transmission in films increased slightly when the

nickel concentration increased while the reflectance of all samples steadily decreases with increased wavelength.

(b) Effect of annealing temperature on transmittance and reflectance of Ni-doped CdS thin films

Figures 5.10 show the transmittance and reflectance spectra of 25 wt% Ni-doped CdS thin films annealed at various temperatures i.e. 150 °C, 250 °C, 350 °C, and 450 °C.

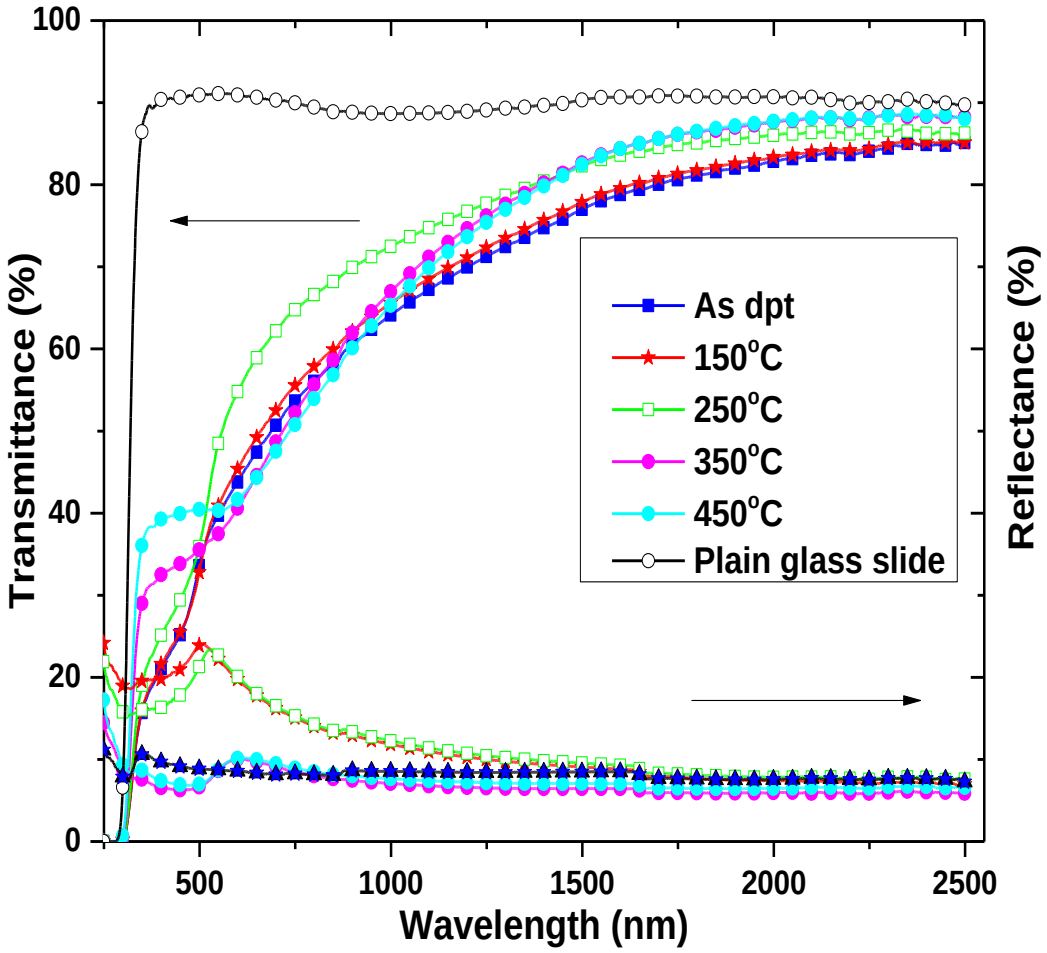

Figure 5. 10: Transmittance and reflectance spectra of 25 wt% Ni-doped CdS thin films prepared using chemical bath deposition and annealed at various temperatures

It is observed that the transmittance of as-prepared samples is lower than those of annealed samples over all the wavelength regions 250 nm to 2500 nm. The transmittance of the 25 wt% doped samples increased as the annealing temperature was at 250 °C for all wavelengths. However, when the films were annealed at temperatures 350 °C and 450 °C, the transmittance of the thin films

decreased in the UV-VIS region of the solar spectrum and slightly increases in the near infra-red region. Annealing the samples at temperatures 150 °C and 250 °C encourages recrystallization and the crystallinity of the films is improved. Also, from the transmittance and reflectance spectra shown in figure 5.10, it is observed that the CdS:Ni films with 25 wt% nickel concentration annealed at 250 °C and 450 °C have nearly the same (maximum) transmittance values in the range of 1500 nm-2500 nm. But in the range of 500 nm-1500 nm, CdS:Ni films with 25 wt% nickel concentration annealed at 250 °C have the highest (maximum) transmittance values. Therefore, 25 wt% is the optimal nickel dopant concentration while 250 °C is the optimal annealing temperature for best results when used as window/buffer as most of the sunlight must be absorbed in the absorber layer to increase the efficiency of the solar cell.

Figures 5.11 - 5.14 show the transmittance and reflectance spectra of CdS:Ni thin films annealed at 150 °C, 250 °C, 350 °C, and 450 °C respectively.

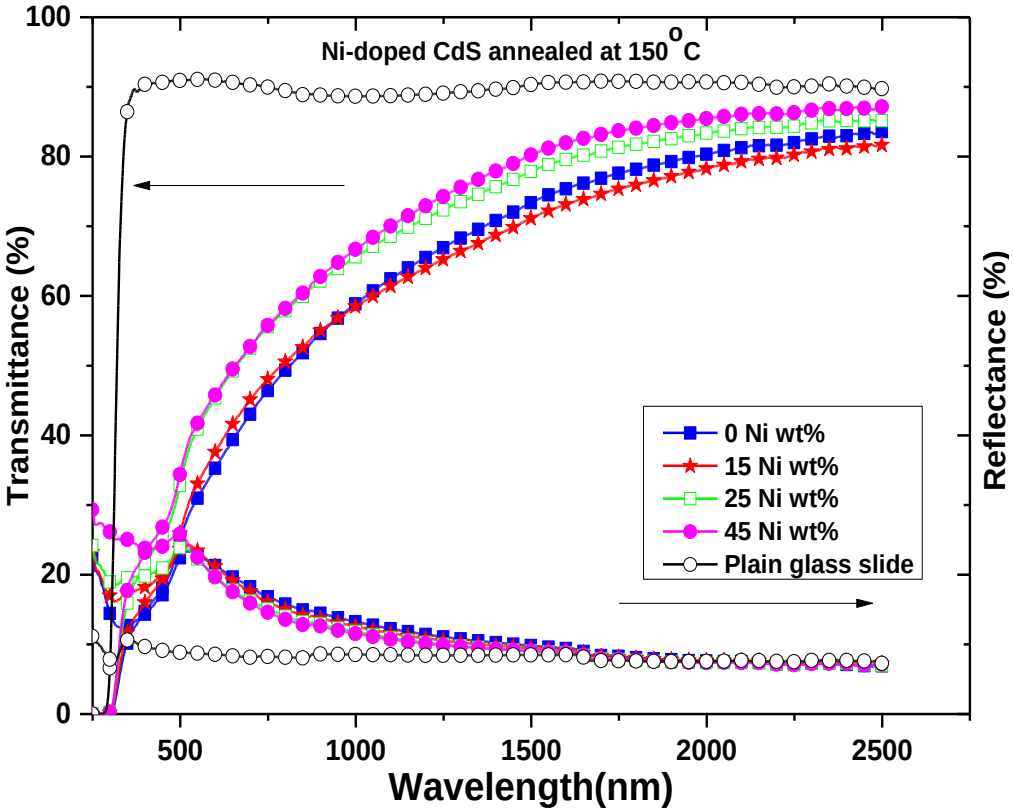

Figure 5. 11: Transmittance and reflectance spectra of undoped and Ni-doped CdS thin films prepared using chemical bath deposition and annealed at 150 °C

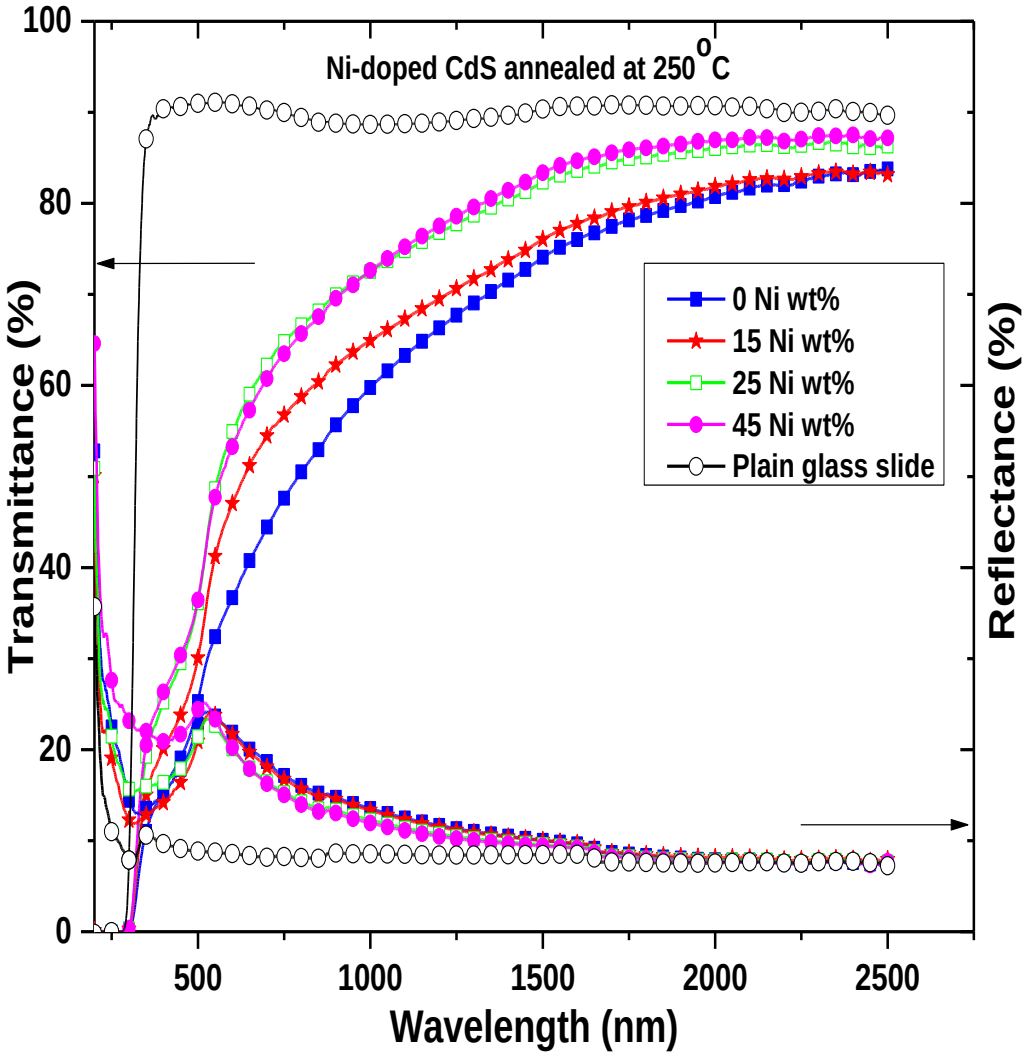

Figure 5. 12: Transmittance and reflectance spectra of Ni-doped CdS thin films prepared using chemical bath deposition and annealed at 250 °C

The transmittance for doped CdS:Ni (0 Ni wt%-45 Ni wt%) thin films increased as annealing temperature was raised upto 250 °C for all wavelengths. Annealing the samples at temperatures 150 °C and 250 °C encourages recrystallization and the crystallinity of the thin films to improve. From the transmittance spectra, it is evident that the transmittance of the thin films increased as dopant concentration, and annealing temperature increased. The increase in transmittance and the subsequent decrease in reflectance of CdS:Ni films as the dopant concentration and annealing temperature increases may be as a result of an increase in the crystallinity of the thin films with increasing dopant concentration and annealing temperature.

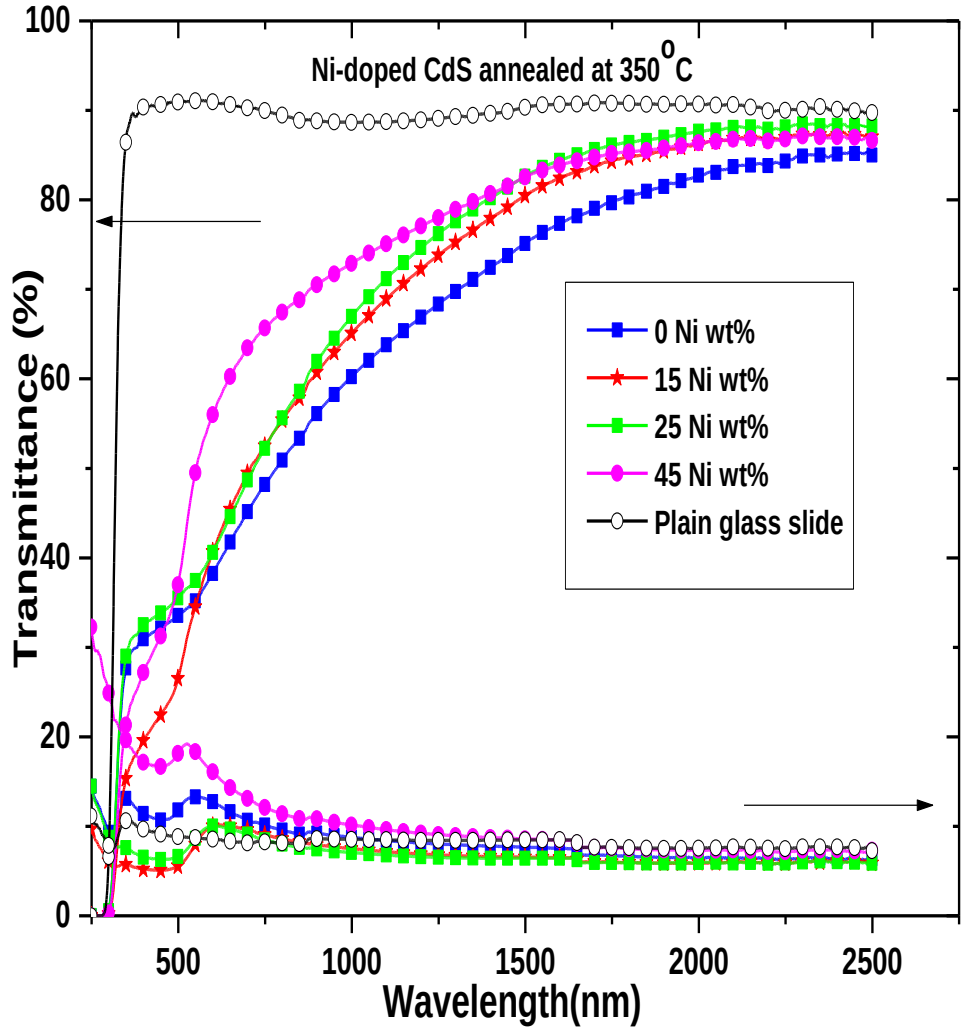

Figure 5. 13: Transmittance and reflectance spectra of Ni-doped CdS thin films prepared using chemical bath deposition and annealed at 350 °C.

Figures 5.13-5.14 show the transmittance and reflectance spectra of CdS:Ni thin films annealed at 350 °C and 450 °C, respectively. From the spectra, it is observed that annealing the thin films at these high temperatures lowers the transmittance of the thin films in the UV-VIS region of the solar spectrum and slightly increases in the near infra-red region. Annealing CdS:Ni films at these high temperatures results in the evaporation of some of the sulphur in the thin films. The colour of the films changes from yellow to brownish-yellow.

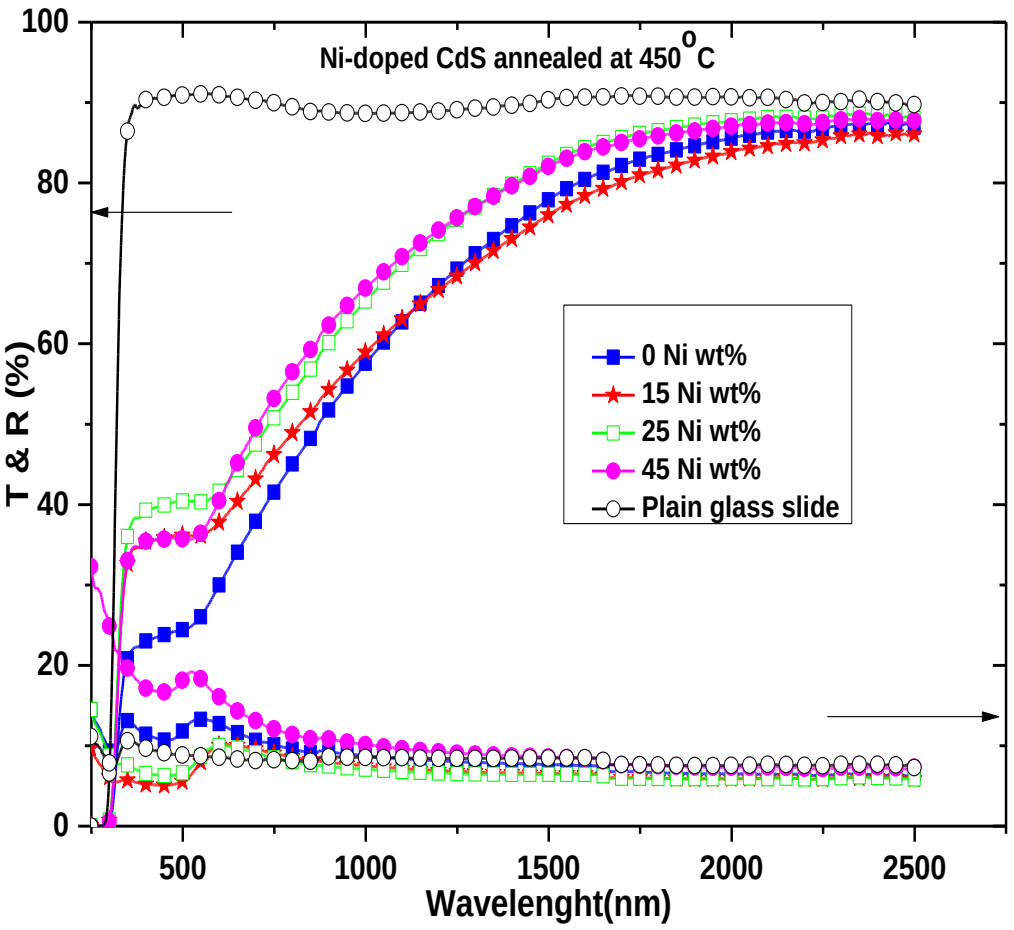

Figure 5. 14: Transmittance and reflectance spectra of Ni-doped CdS thin films prepared using chemical bath deposition and annealed at 450 °C

5.3.2 Optical bandgap

The Tauc model has been devised as an empirical model for determining the optical gap in semiconductors and gives the relationship between the absorption coefficients (α) to photon energy ($h\upsilon$) by the equation;

$$(\alpha h\nu) = \beta(h\nu - E_g)^{\acute{\eta}} \tag{5.3}$$

where α is the absorption coefficient, ($h\upsilon$) is photon energy, β is the band tailing parameter, E_g the bandgap of the material (the separation between the valence and conduction bands), and $\acute{\eta}$ denotes the type of transition which is dependent upon the nature of the material, whether it is crystalline or amorphous and it assumes values of $\acute{\eta} = 2$ for indirect gap materials and $\acute{\eta} = 1/2$ for

direct gap materials. For crystalline materials, direct transitions are valid according to Tauc's relation and ή = ½, hence:

$$(\alpha h\nu) = \beta(h\nu - E_g)^{\frac{1}{2}} \tag{5.4}$$

(a) Influence of Ni^{2+} concentration on the bandgap of CdS thin films

The bandgap values of the undoped and Ni-doped CdS films were calculated by plotting a graph of $(\alpha h\nu)^2$ against $h\nu$ for direct bandgap as shown in Figures 5.15 and 5.16. Table 5.5 shows the summary of bandgap values for undoped and Ni-doped CdS thin films annealed at various temperatures.

Table 5. 5: Summary of Bandgap values for undoped and Ni-doped CdS thin films annealed at various temperatures

	Nickel concentration			
Annealing temperature	0 wt%	15 wt%	25 wt%	45 wt%
	E_g(eV)	E_g(eV)	E_g(eV)	E_g(eV)
As-prepared	2.28	2.42	2.45	2.45
150 ℃	2.20	2.31	2.42	2.46
250 ℃	2.19	2.19	2.01	2.19
350 ℃	3.68	3.57	3.82	3.38
450 ℃	3.94	4.03	4.01	3.79

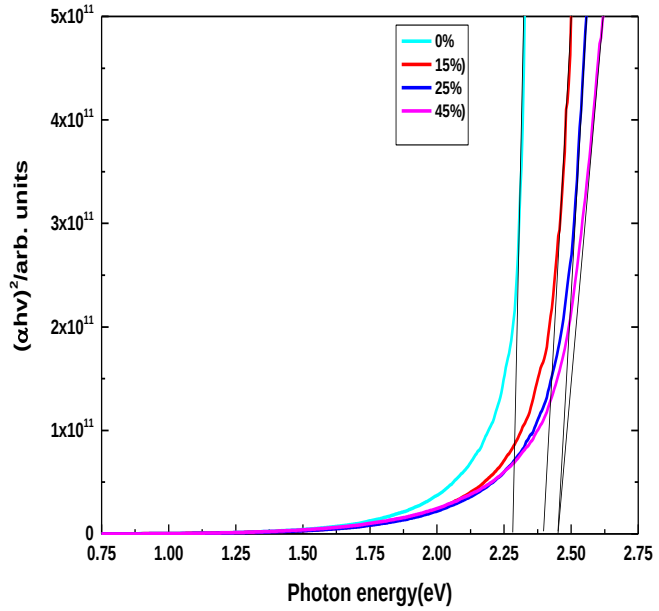

(a) Determination of bandgaps of as-deposited Ni-doped CdS thin films

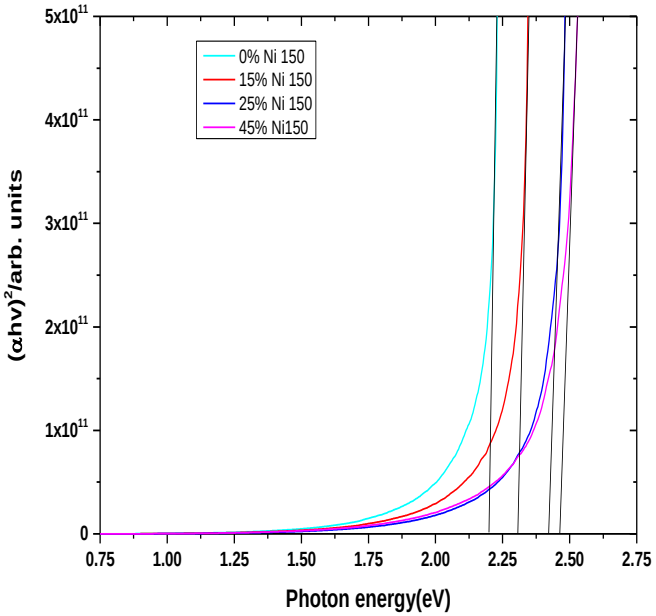

(b) Determination of bandgaps of Ni-doped CdS thin films annealed at 150°C

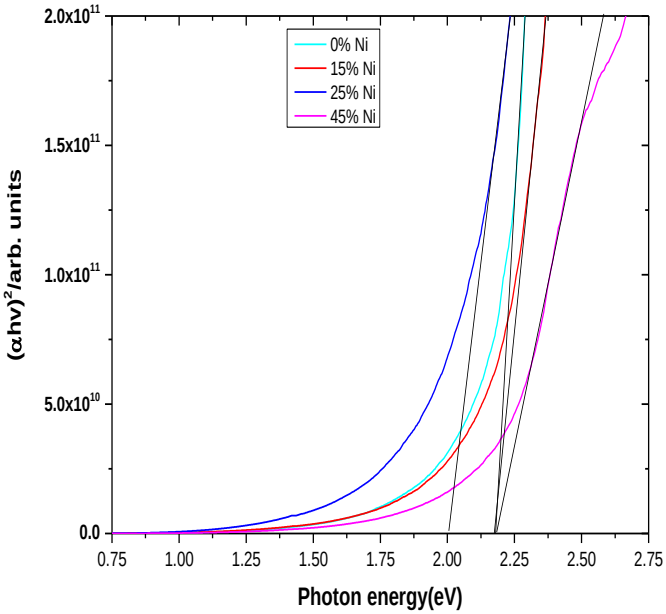

(c) Determination of bandgaps of Ni-doped CdS thin films annealed at 250°C

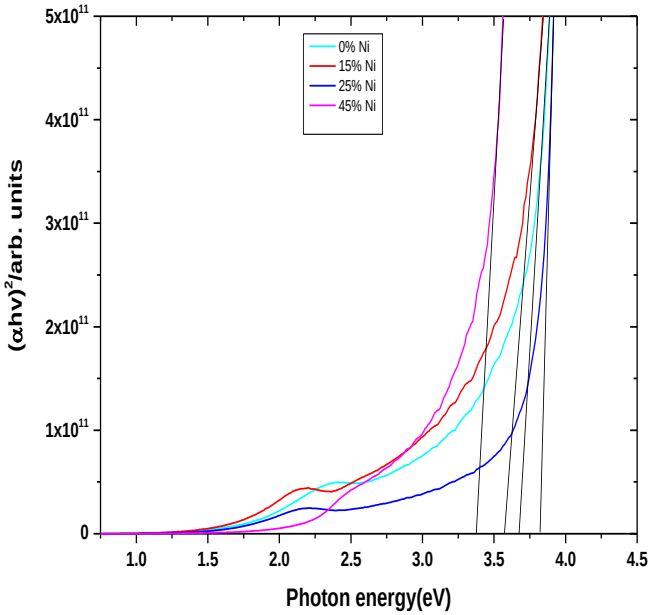

(d) Determination of bandgaps of Ni-doped CdS thin films annealed at 350°C

Figure 5. 15: Graphs of $(\alpha h\upsilon)^2$ against $h\upsilon$ for Ni-doped CdS thin films with varying nickel concentration (wt%) annealed at various temperatures. (a) As-deposited Ni-doped CdS films (b) Ni-doped CdS films annealed at 150 °C (c) Ni-doped CdS films annealed at 250 °C (d) Ni-doped CdS films annealed at 350 °C

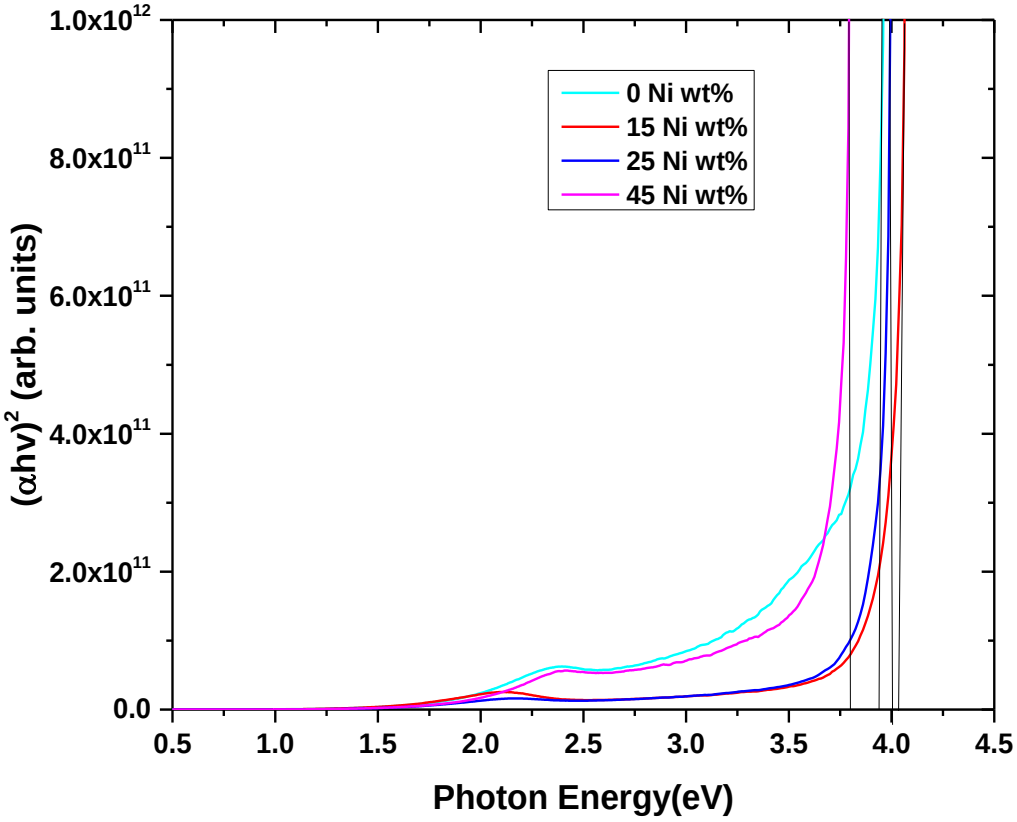

Figure 5. 16: Graphs of $(\alpha hv)^2$ against hv for Ni-doped CdS thin films with varying nickel concentration (wt%) annealed 450 °C

The bandgap of as-grown un-doped CdS was found to be approximately 2.30 eVs as shown in table 5.5. The bandgap of the as-grown un-doped CdS was found to be slightly lower than the bandgap of bulk CdS crystal (direct bandgap ≈ 2.42 eV (Haynes, 2014). The bandgap of doped CdS (as-prepared) increased as the concentration of nickel is increased with samples having 45 Ni wt% registering a bandgap of 2.45 eV as shown in Table 5.5. This observation can be explained as follows. Ni^{2+} has an ionic radius of 0.069 nm, which is slightly less than that of Cd^{2+}ions (0.097 nm) and its electronegativity of 1.91 Pauling is higher than that of Cd^{2+} ions (1.61 Pauling). With the increased concentration of Nickel, more and more nickel ions substituted cadmium ions in the crystalline structure of CdS, widening the bandgap of CdS (Gellings and Bouwmeester, 1997). The increase in bandgap as dopant concentration was increased could be as a result of donor electrons occupying the states at the bottom of the conduction band blocking thus the low energy transitions. This is known as the Burstein-Moss effect (Lu *et al.*, 2007).

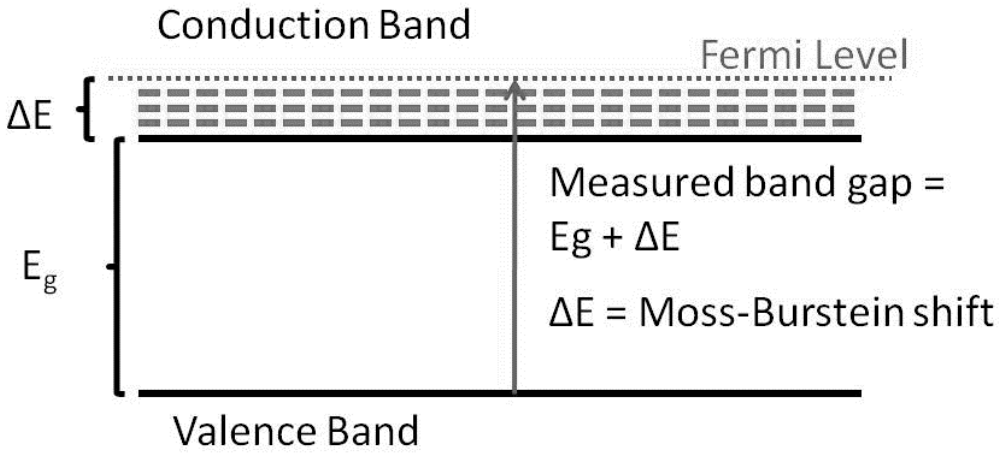

Figure 5. 17: Illustration of Burstein-Moss effect (Source: Wikipedia.org)

The Burstein-Moss band filling effect results from the Pauli Exclusion Principle which states that: "in an atom, there cannot be two or more equivalent electrons for which the values of all four quantum numbers coincide", and is seen in semiconductors as a shift in band-gap with increasing doping. The shift arises because the Fermi energy (E_F) lies in the conduction band for heavy n-type doping (or in the valence band for p-type doping) as illustrated in figure 5.17. The filled states block thermal or optical excitation. As a result, the measured bandgap determined from the onset of interband absorption moves to higher energy (Lu *et al.*, 2007).

(b) Influence of annealing temperature on the bandgap of CdS:Ni thin films

When the films, both doped and undoped, were annealed for 30 minutes in the air, it was observed that the bandgap of the films decreased when the annealing temperature was raised upto 250 ℃ and then increased with further annealing at 350 ℃ and 450 ℃ as shown in Figures 5.18 and 5.19. The decrease in the energy bandgap of films as the annealing temperature is raised upto 250 ℃ could be attributed to the increase in the grain size (diameter) of the CdS structure due to the annealing process (Enríquez, 2003; Nair et al., 2001). Reorganization of the film happens at all annealing temperatures. The voids in the films are filled leading to denser films with lower bandgaps (Metin and Esen, 2003). Another possibility could be as a result of a reduction in strain within the films after annealing (Enríquez, 2003).

.

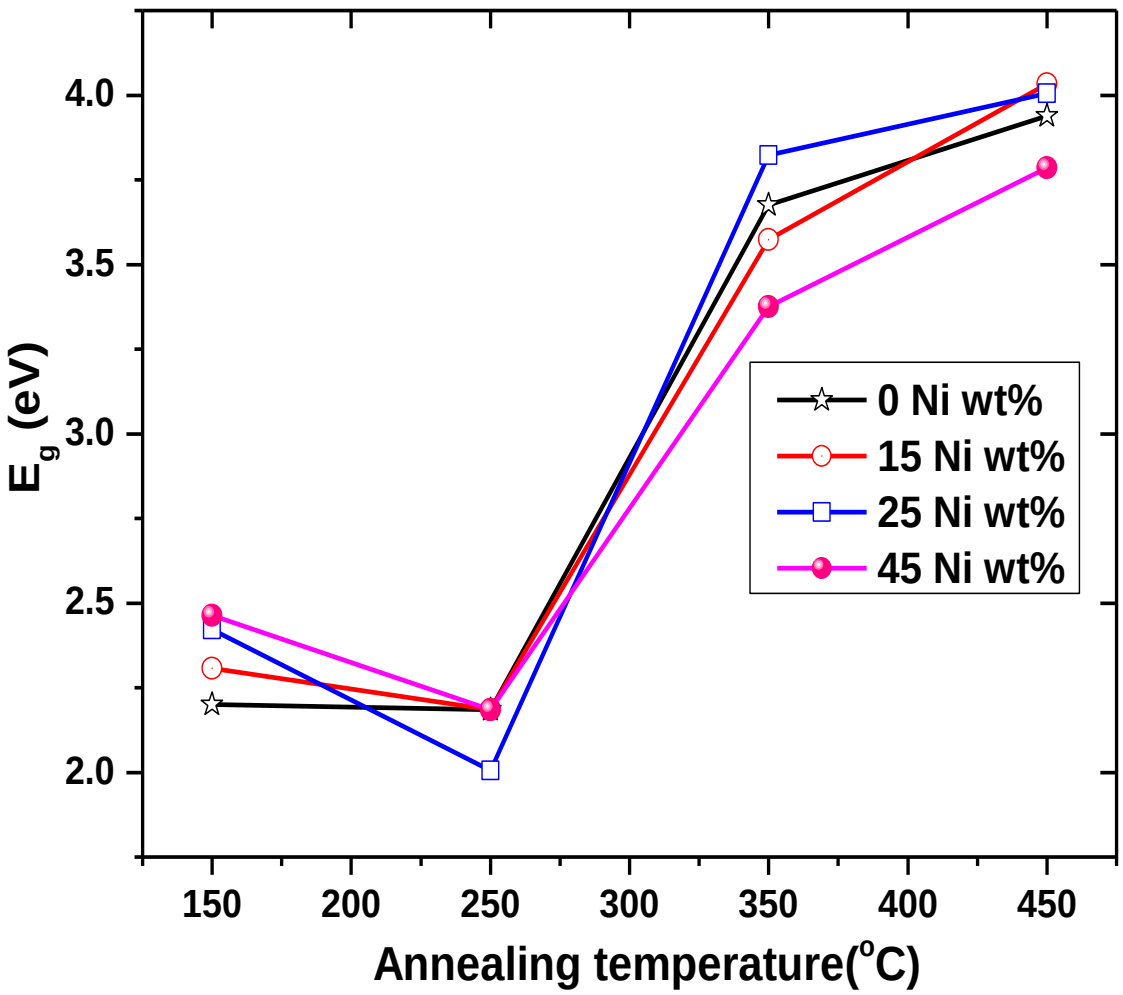

Figure 5. 18: Bandgap energy dependence on the thermal annealing temperature of nickel doped cadmium sulphide (CdS:Ni)

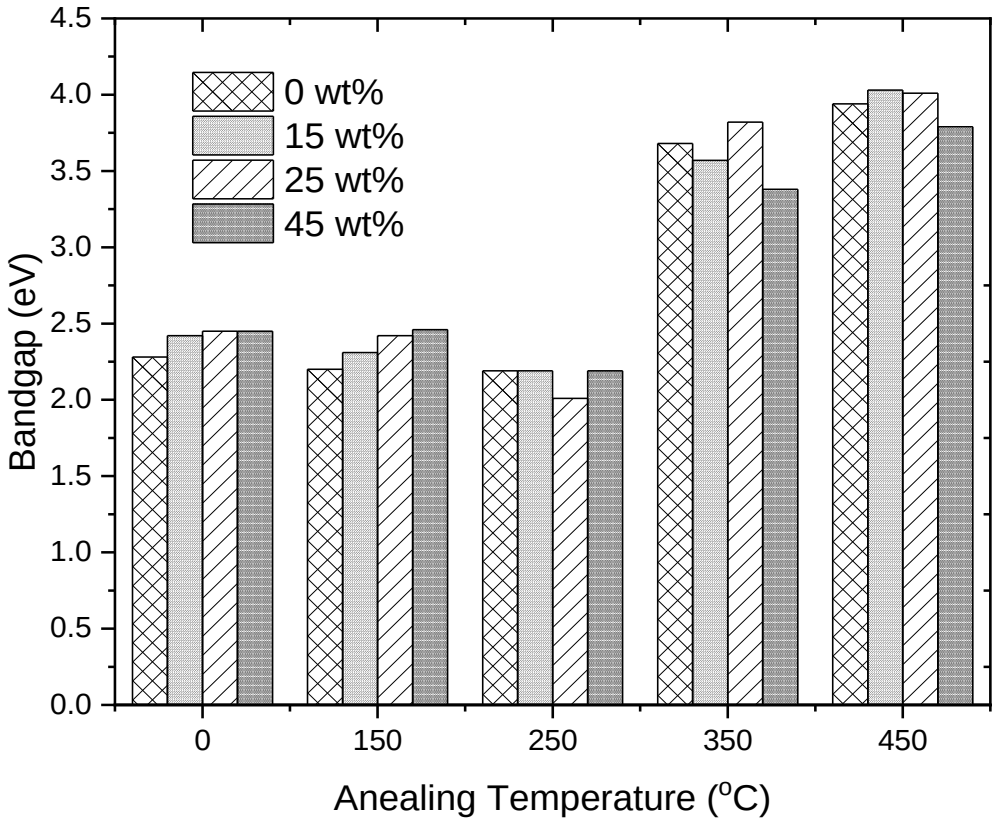

Figure 5. 19: Comparative bar graph showing the band-gap energy of nickel doped CdS thin films prepared using chemical bath deposition and annealed at varied temperature (150 °C – 450 °C)

The increase in the energy bandgap of films annealed at 350 °C and 450 °C could be attributed to the phase transition from cubic (zinc-blend) to hexagonal (wurtzite) structure as confirmed by the appearance of new peaks in the XRD patterns in Figure 5.5. CdS has a critical temperature (between 250 °C and 300 °C) at which a cubic to hexagonal lattice transition occurs (Zelaya-Angel et al., 1995). From these observations, it is noted that the dopant concentration and annealing temperature play an important role in the bandgap assignment. This, therefore, means that the energy bandgap of CdS:Ni thin films can be controlled to suit the application of the films by varying the ratio of Cd and Ni and the annealing temperature.

5.3.3 Absorption coefficients

The absorption coefficient (α) of undoped and Ni-doped CdS thin films annealed at varying annealing temperature was calculated from the experimental data of optical reflectance and transmittance data using equation (5.5):

$$\alpha = -\frac{ln\left(\frac{T}{1-R}\right)}{D_t} \tag{5.5}$$

where α is the absorption coefficient, T is transmittance, R is the reflectance, and D_t is the thickness of the film. The plots of absorption coefficient versus wavelength for undoped and Ni-doped CdS thin films are shown in Figure 20.

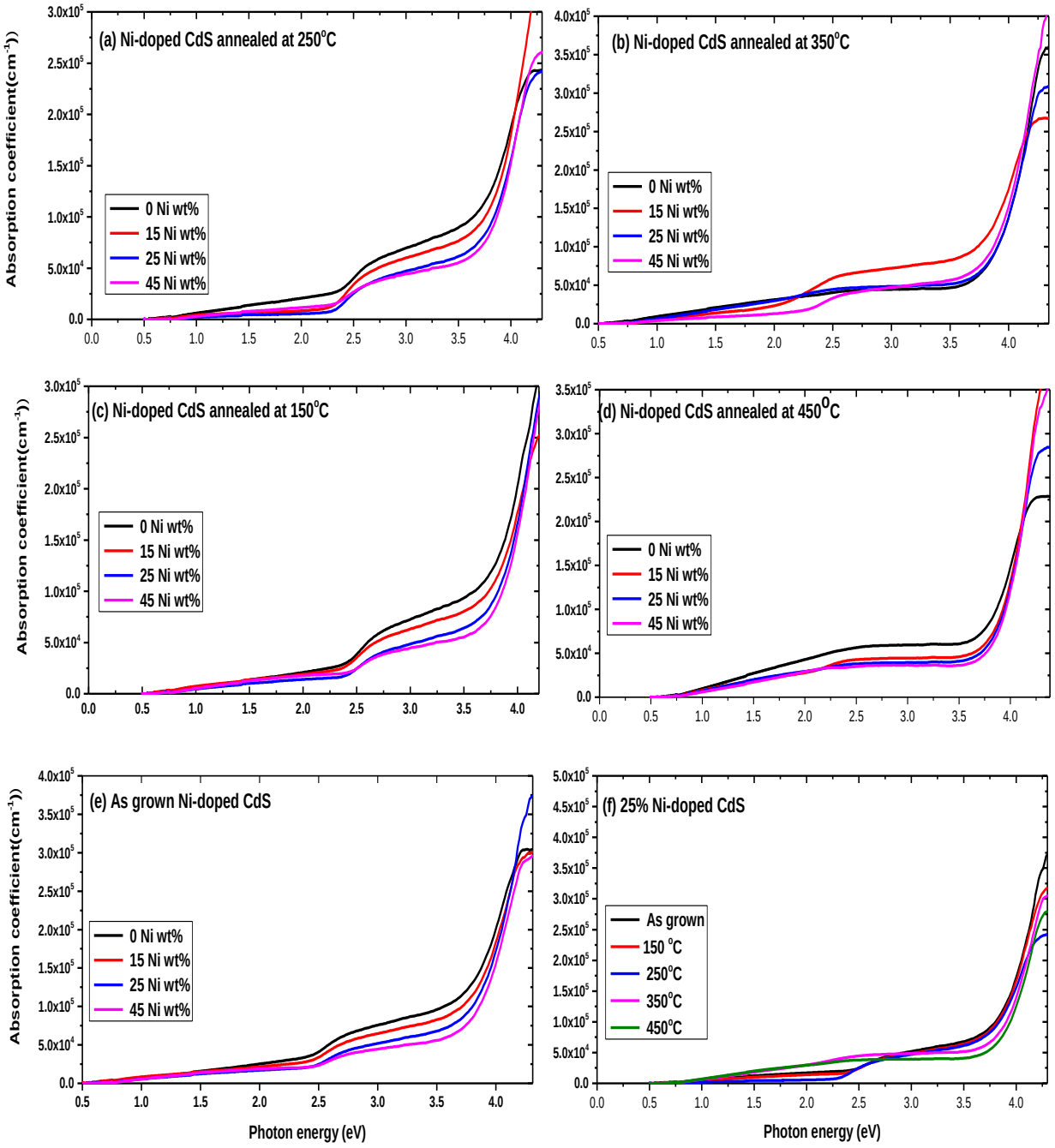

Figure 5. 20: Absorption coefficients of undoped and Ni-doped CdS thin films annealed at various annealing temperatures (a) Ni-doped CdS thin films annealed at 250 °C (b) Ni-doped CdS thin films annealed at 350 °C (c) Ni-doped CdS thin films annealed at 150 °C (d) Ni-doped CdS thin films annealed at 450 °C (e) As-grown Ni-doped CdS thin films (f) 25 wt% Ni-doped CdS thin films annealed at various temperature

The absorption coefficients for all the undoped and Ni-doped CdS thin films were found to be greater than 10^4 cm^{-1} in the visible region (380 nm to 780 nm) and near-infrared (780 nm and

2500 nm) regions which confirmed that the films have a direct optical energy gap. The absorption coefficients in the visible region (VIS) region are larger than those in the near-infrared region and decrease with the increase of nickel doping. The absorption coefficient of as grown Ni-doped CdS films decreased with increasing nickel content with samples having 45 wt% nickel concentration having the lowest absorption coefficient across all wavelengths. The absorption coefficient of the films also decreased when the annealing temperature was raised to 250 ℃ as shown in Figure 5.20. Samples annealed at 350 ℃ and 450 ℃ were observed to have a slightly higher absorption coefficient at regions below 460 nm (2.7 eV) than the as-grown and those annealed at 250 ℃. But above 460 nm (2.7 eV), the absorption coefficient of Ni-doped CdS films decreased with increasing as shown in figure 5.20 (f).

5.3.4 Refractive index (*n*) and Extinction coefficient/absorption index (α)

(a) Refractive index (*n*)

The refractive index (*n*) of undoped and Ni-doped CdS thin films annealed at varying annealing temperature was calculated from the experimental data of optical reflectance data using equation (5.6):

$$n = \frac{1+R}{1-R} + \sqrt{\frac{4\mathrm{R}}{(1-\mathrm{R})^2} - \mathrm{k}^2} \tag{5.6}$$

where R is the optical reflectance while k is the extinction coefficient of the films.

Figure 5.21 shows the variation of the refractive index of Ni-doped CdS thin films as a function of wavelength.

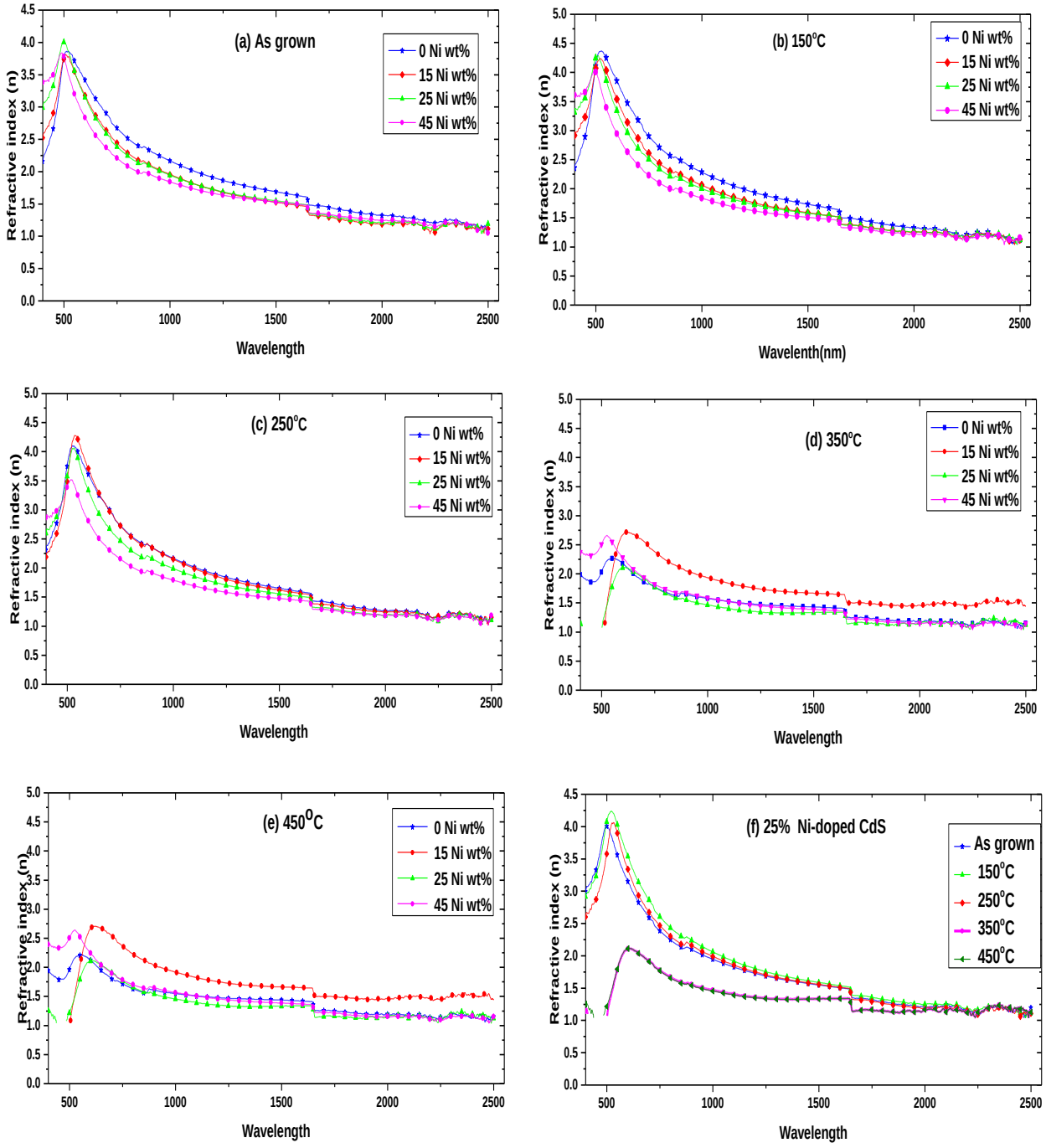

Figure 5. 21: Plots of refractive index Ni-doped CdS thin films annealed at various temperatures (a) As-prepared Ni-doped CdS thin films (b) Ni-doped CdS thin films annealed at 150 °C (b) Ni-doped CdS thin films annealed at 150 °C (c) Ni-doped CdS thin films annealed at 250 °C (d) Ni-doped CdS thin films annealed at 350 °C (e) Ni-doped CdS thin films annealed at 450 °C (f) 25 wt% Ni-doped CdS thin films annealed at various temperatures

From Figure 5.21(a), it is observed that the undoped CdS films have a high refractive index compared to Ni-doped CdS thin films. The refractive index of the Ni-doped CdS films decreases with an increase in nickel concentration across all wavelengths with films doped with 45 wt% nickel concentration having the lowest refractive index. The decrease in the refractive index as the nickel concentration increases is thought to be largely due to an increase in free carrier concentration Refractive index is inversely related to the carrier concentration (Paskov, 1997). Peaks

Typically, a decrease in the refractive index suggests an increase in transmittance. The optical transmittance of as-grown undoped and Ni-doped CdS thin films are discussed in section 5.3.1. From Figure 5.21(a), it is observed that the refractive index of the as-grown undoped and Ni-doped CdS films increases in wavelength 380 nm – 500 nm (visible region of the solar) and starts to decrease steadily as the wavelength increases up to 2500 nm. In wavelengths 500 nm – 700 nm, the refractive index decreases steadily with increasing wavelength indicating that the films are highly transmitting in the region. In general, the refractive index is higher for the shorter wavelength, and it gradually decreases at a higher wavelength.

Figure 5.21(f) shows the variation of the refractive index of the 25 wt% Ni-doped CdS thin films annealed at various temperatures as a function of wavelength. The refractive index of the films decreases slightly with an increase in annealing temperature up to 250 °C. Ni-doped CdS films annealed at 450 °C had the lowest refractive index. Peaks were observed on all the plots of the refractive index of undoped and nickel-doped CdS thin films annealed at various temperatures. The peaks are seen to shift to a higher wavelength with increasing annealing temperature.

(b) Extinction coefficient (absorption index)

The extinction coefficient (k) of undoped and Ni-doped CdS thin films annealed at varying annealing temperature was calculated from the experimental data of optical reflectance data using equation (5.7):

$$k = \frac{\alpha\lambda}{4\pi} \tag{5.7}$$

where λ is the wavelength of the light and α is the absorption coefficient.

Plots of the extinction coefficient versus wavelength are shown in Figure 5.22.

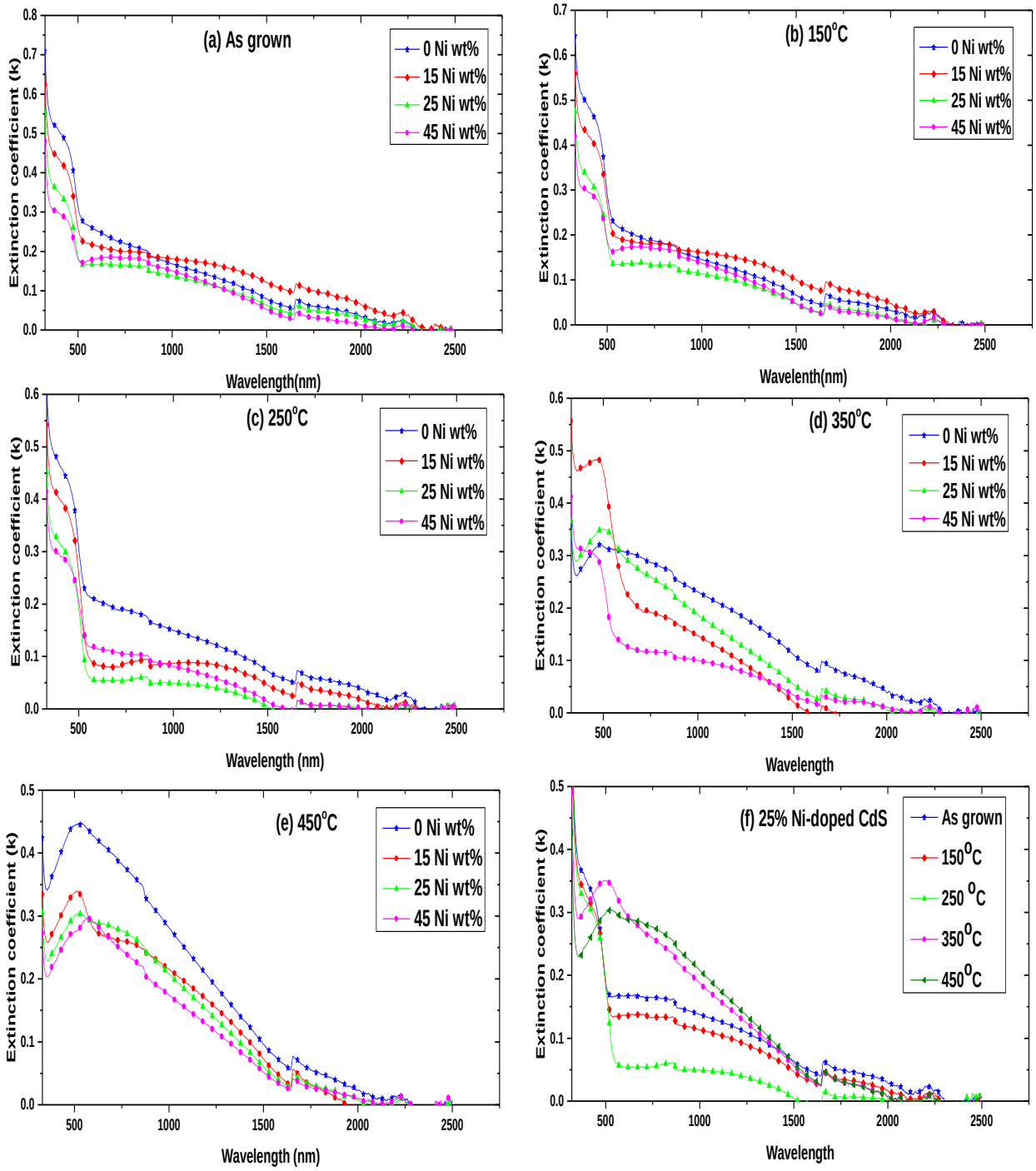

Figure 5. 22: Plots of extinction coefficient versus wavelengths of Ni-doped CdS thin films annealed at various temperatures: (a) As-prepared Ni-doped CdS thin films (b) Ni-doped CdS thin films annealed at 150 °C (b) Ni-doped CdS thin films annealed at 150 °C (c) Ni-doped CdS thin films annealed at 250 °C (d) Ni-doped CdS thin films annealed at 350 °C (e) Ni-doped CdS thin films annealed at 450 °C (f) 25 wt% Ni-doped CdS thin films annealed at various temperatures

It is observed that the extinction coefficient of the as-prepared Ni-doped CdS films decreased with an increase in nickel concentration across all wavelengths. The extinction coefficient of the 0 wt%, 15 wt%, 25 wt% and 45 wt% nickel content at 380 nm was found to be 0.52, 0.45, 0.36 and 0.30 respectively. At 780 nm, extinction coefficient of the 0 wt%, 15 wt%, 25 wt% and 45 wt% nickel content was found to be 0.21, 0.20, 0.17 and 0.18 respectively.

Figure 5.22(f) shows extinction coefficient plots of 25 wt% Ni-doped CdS thin films annealed at varying annealing temperatures. It was observed that the extinction coefficient values of the films decreased as the annealing temperature was raised upto 250 °C with films annealed at 250 °C having the lowest values of extinction coefficient across all wavelengths. The low extinction coefficient values for both as-grown and annealed thin films show how easily an electromagnetic wave can penetrate into the material. Further annealing the films at 350 °C and 450 °C increased their extinction coefficient across all wavelengths with those annealed at 450°C having the highest extinction coefficients. The sudden increase in extinction coefficient seen in films annealed at 350 °C and 450 °C may be attributed to the sudden decrease in their transmittance (Figure 5.10) due to phase transition from cubic (zinc-blend) to hexagonal (wurtzite) structure.

5.4 Urbach Energy

5.4.1 Influence of Ni^{2+} concentrations on Urbach energy of Ni-doped CdS films

Urbach energy of as-grown undoped CdS and Ni-doped CdS thin films were estimated by taking the reciprocal of the gradients of the $ln\alpha$ vs. $h\upsilon$ plots as given in equation (5.8):

$$ln\alpha = ln\alpha_0 + \frac{h\upsilon}{E_U} \tag{5.8}$$

Doping CdS with varying nickel concentrations resulted in varying Urbach energies. Figure 5.23 shows plots of $ln\alpha$ vs. $h\upsilon$ used to estimate the Urbach energies of the as-grown films.

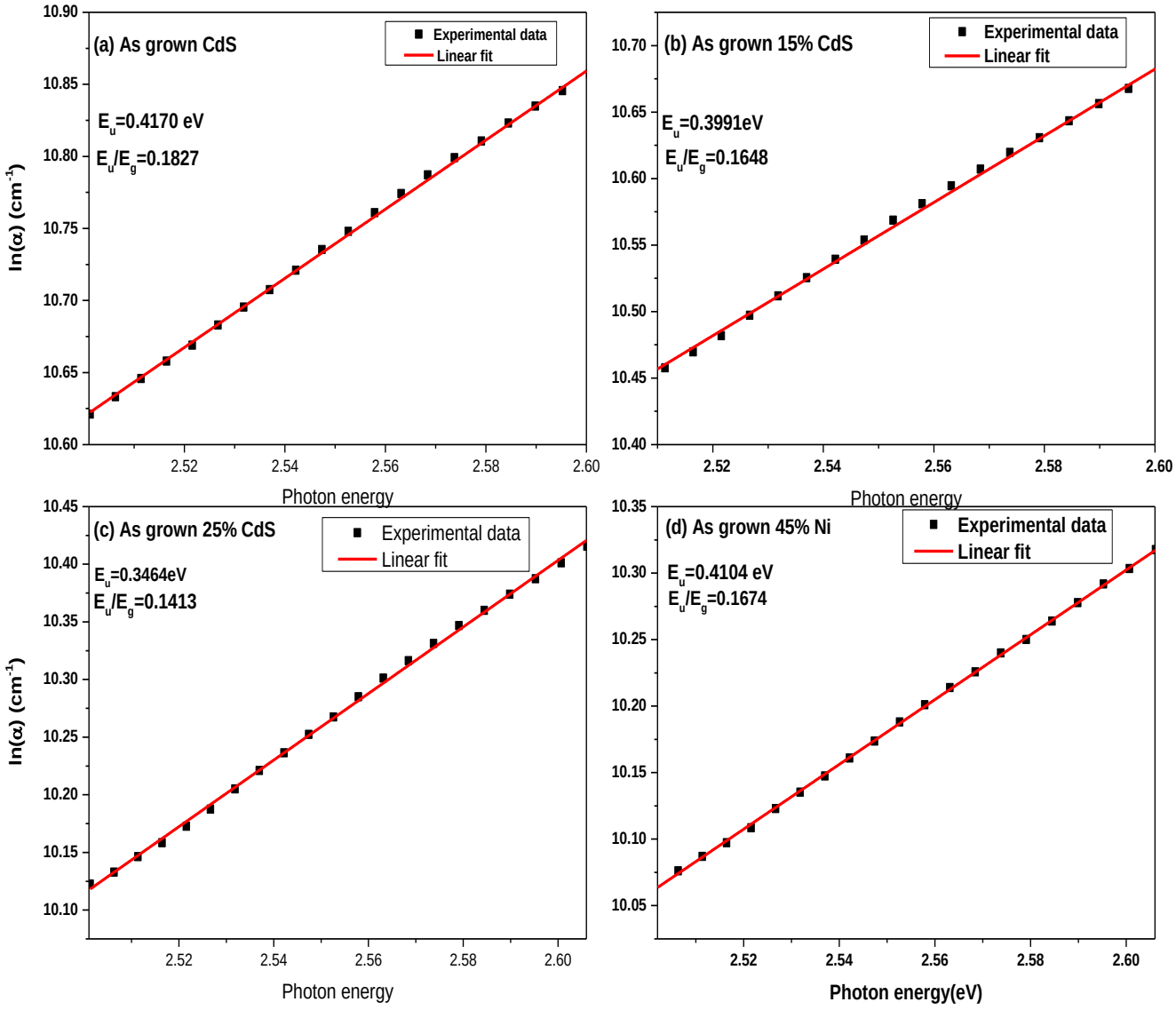

Figure 5. 23: Urbach energy of as-prepared Ni-doped: (a) undoped CdS (b) CdS with 15 Ni wt% (c) CdS with 25 Ni wt% (d) CdS with 45 Ni wt%

The Urbach energy of the films was found to be in the range of 0.35 eV – 0.42 eV. The estimates of the Urbach energy and ratio Eu/Eg are given in Table 5.6. It is observed that the Ni-doped CdS films have lower Urbach energy than undoped CdS films. This indicates an improvement in the quality of cadmium sulphide thin film on nickel doping due to improved crystallinity with increasing dopant concentration as evidenced by the XRD patterns in Figure 5.3.

Table 5. 6: Bandgaps and Urbach energies of undoped CdS and Ni-doped CdS thin film

Nickel Concentration	E_g (eV)	E_U (eV)	E_U/E_g
0 wt%	2.28	0.42	0.18
15 wt%	2.42	0.40	0.16
25 wt%	2.45	0.35	0.14
45 wt%	2.45	0.41	0.17

The change in Urbach energy as shown in Table 5.6 indicates the introduction of tail states at the band edges as the dopant concentration varies. The dopant (nickel) content is responsible for the width of localized states in the optical band of the films (Marquina *et al.*, 2017). The change in Urbach energies of nickel-doped CdS as shown in Table 5.6 confirms that nickel was successfully incorporated into cadmium sulphide.

5.4.2 Influence of annealing temperatures on Urbach energy of Ni-doped CdS thin films

Figures 5.24 - 5.27 show the $ln\alpha$ vs. $h\upsilon$ plots for Ni-doped CdS thin films annealed at 150 °C, 250 °C, 350 °C, and 450 °C respectively. The summary of bandgap and urbach energies of pure CdS and Ni-doped CdS thin films annealed at various temperatures is given in Table 5.7.

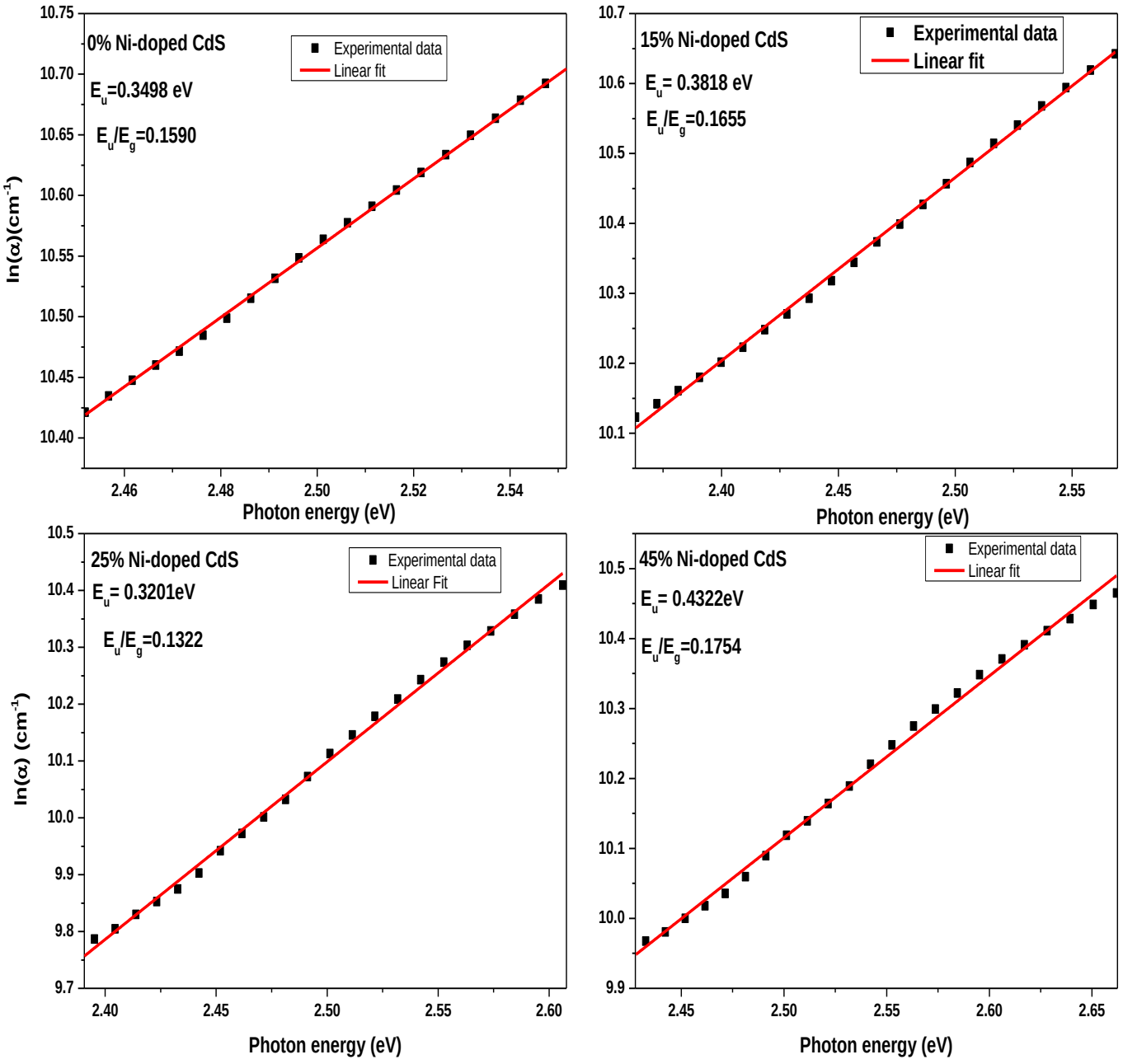

Figure 5. 24: Urbach energy of Ni-doped CdS thin films annealed at 150^{o}C: (a) undoped CdS (b) CdS with 15 Ni wt% (b) CdS with 25 Ni wt% (c) CdS with 45 Ni wt%

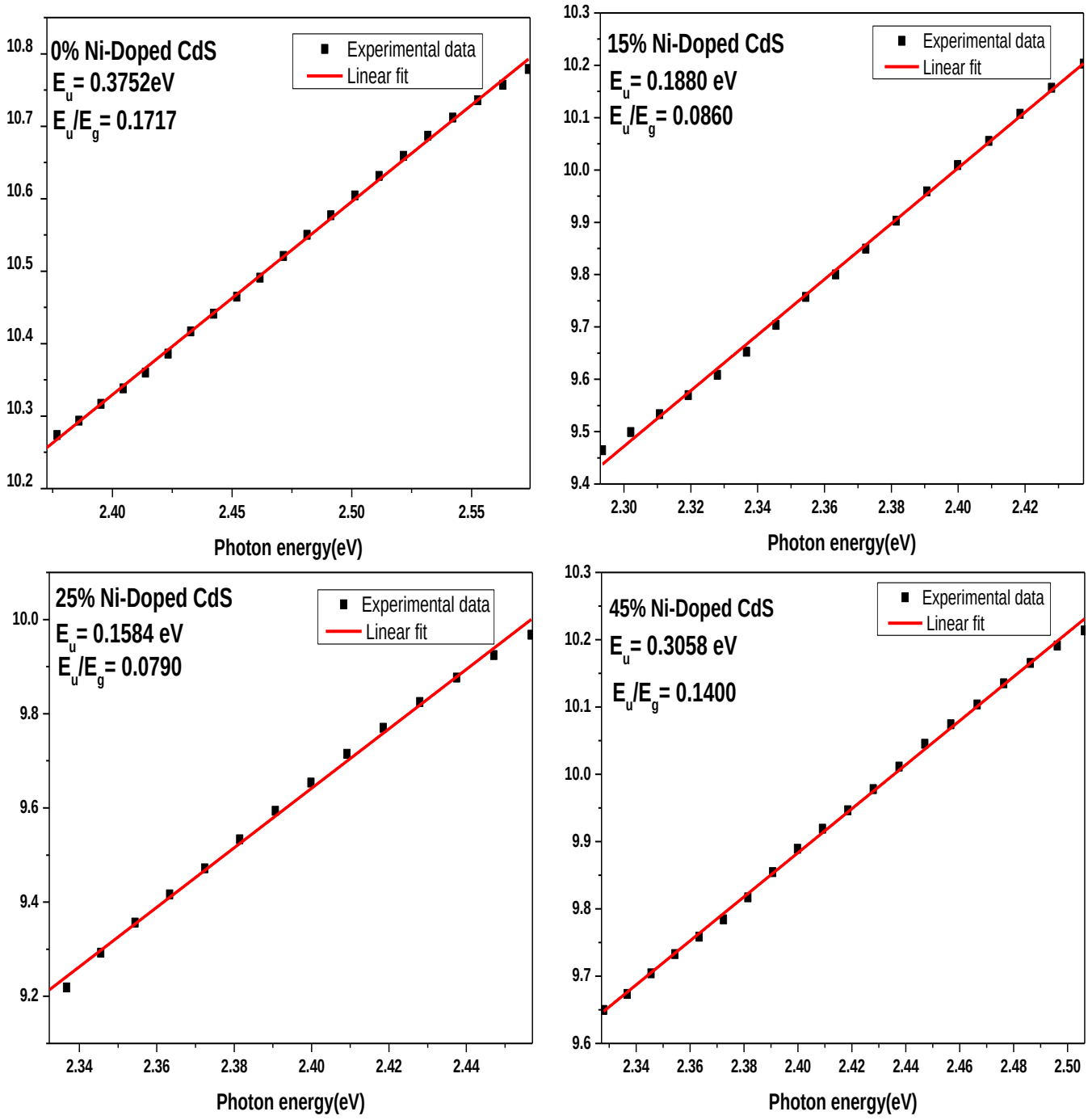

Figure 5. 25: Urbach energy of Ni-doped CdS thin films annealed at 250^{o}C: (a) undoped CdS (b) CdS with 15 Ni wt% (b) CdS with 25 Ni wt% (c) CdS with 45 Ni wt%

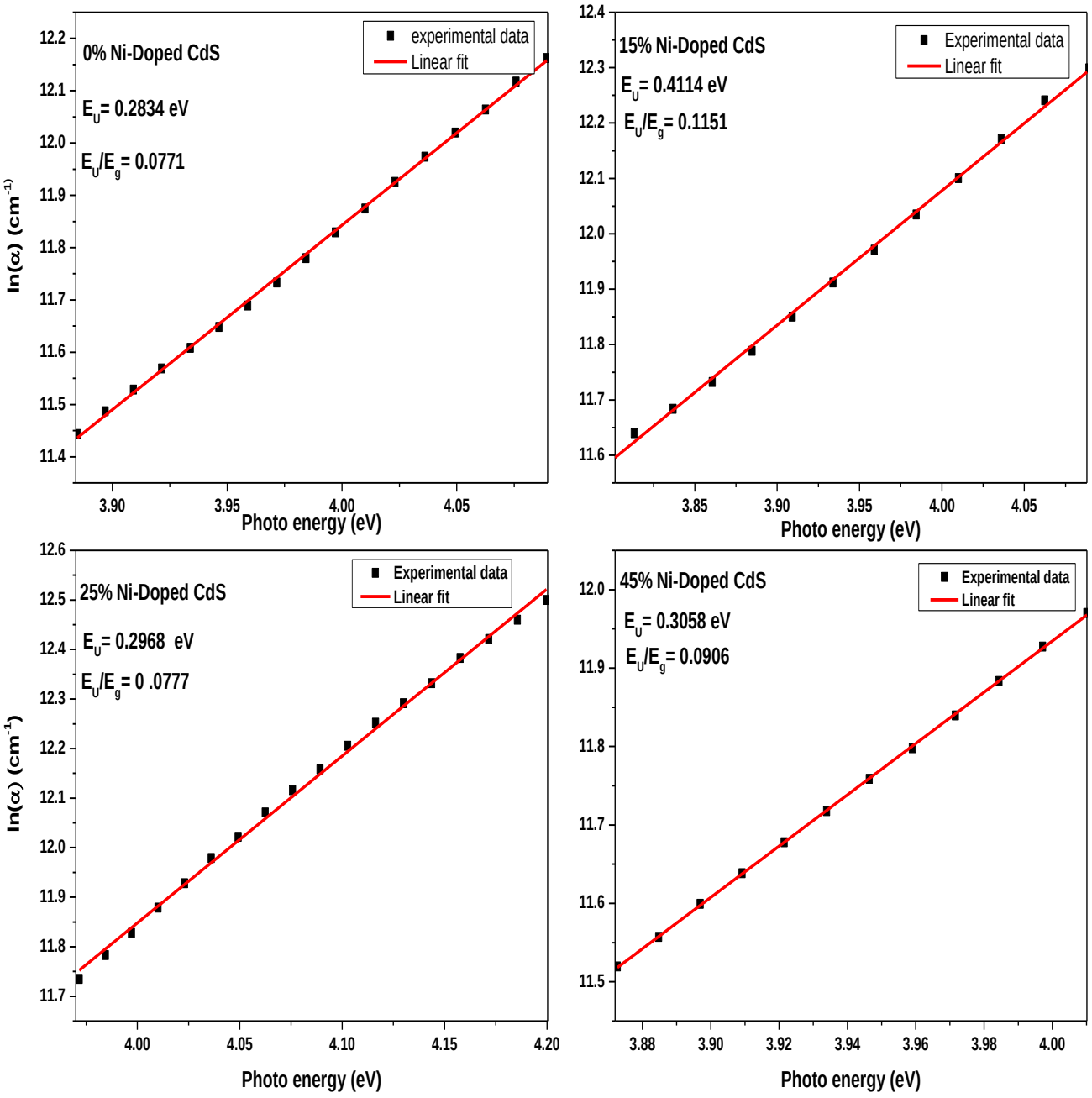

Figure 5. 26: Urbach energy of pure Ni-doped CdS thin films annealed at 350 °C: (a) undoped CdS (b) CdS with 15 Ni wt% (c) CdS with 25 Ni wt% (d) CdS with 45 Ni wt%

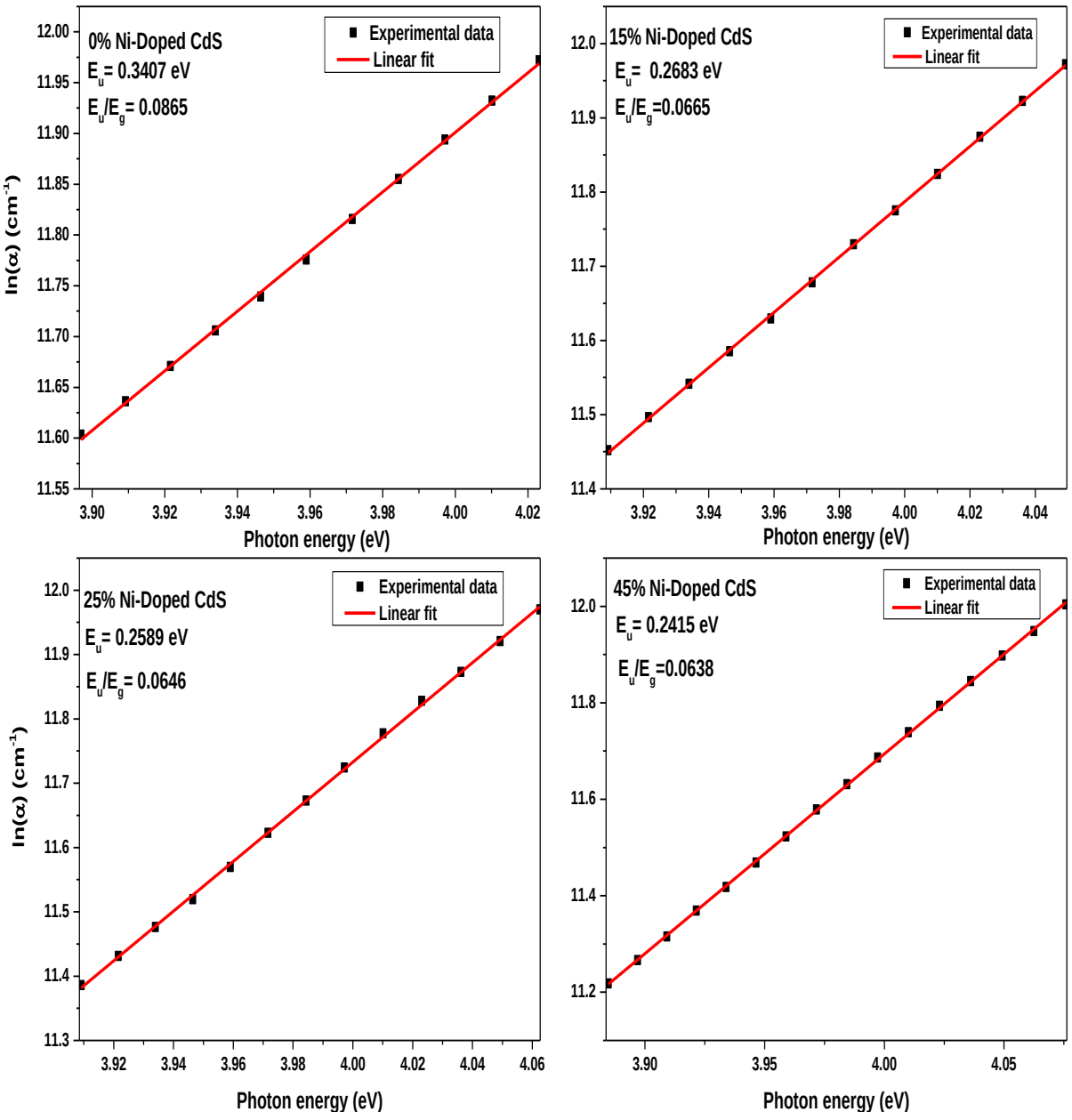

Figure 5. 27: Urbach energy of Ni-doped CdS thin films annealed at 450 °C: (a) undoped CdS (b) CdS with 15 Ni wt% (c) CdS with 25 Ni wt% (d) CdS with 45 Ni wt%

Table 5. 7: Summary of bandgap and urbach energies of pure CdS and Ni-doped CdS thin films annealed at various temperatures: (a) Pure CdS, (b) 15 wt% Ni-doped CdS, (c) 25 wt% Ni-doped CdS (d) 45 wt% Ni-doped CdS.

(a) Undoped CdS films

Annealing temp. (°C)	E_g (eV)	E_U (eV)	(E_U /E_g)
As-prepared	2.28	0.42	0.18
150	2.20	0.35	0.16
250	2.19	0.38	0.17
350	3.68	0.28	0.08
450	3.94	0.34	0.09

(b) 15 wt% Ni-doped CdS films

Annealing temp. (°C)	E_g (eV)	E_U (eV)	(E_U /E_g)
As-prepared	2.42	0.40	0.16
150	2.31	0.38	0.17
250	2.19	0.19	0.09
350	3.57	0.41	0.12
450	4.03	0.27	0.07

(c) 25 wt% Ni-doped CdS films

Annealing temp. (°C)	E_g (eV)	E_U (eV)	(E_U /E_g)
As-prepared	2.45	0.35	0.14
150	2.42	0.32	0.13
250	2.01	0.16	0.08
350	3.82	0.30	0.08
450	4.01	0.26	0.07

(d) 45 wt% Ni-doped CdS films

Annealing temp. (°C)	E_g (eV)	E_U (eV)	(E_U /E_g)
As-prepared	2.45	0.41	0.17
150	2.46	0.43	0.18
250	2.19	0.31	0.14
350	3.38	0.31	0.09
450	3.79	0.24	0.06

Figure 5.28 shows the comparative bar chart showing the urbach energy of Ni-doped CdS thin films annealed at various temperatures i.e. 150 °C, 250 °C, 350 °C, and 450 °C. From Figure 5.28, we observed that the Urbach energy of films decreased as the annealing temperature was raised upto 250 °C. On further annealing, the urbach energy of both doped and undoped films is then seen to increase as the annealing temperature is raised to 350 °C and finally slightly decreases as the temperature is raised to 450 °C. These observations can be explained as follows: The crystallinity of the films improves with increasing annealing temperature upto 250 °C. The disorder in the films is reduced when they were annealed as the voids in the films were filled leading to denser films. Urbach energy has an inverse relation with improvement in the crystalline structure.

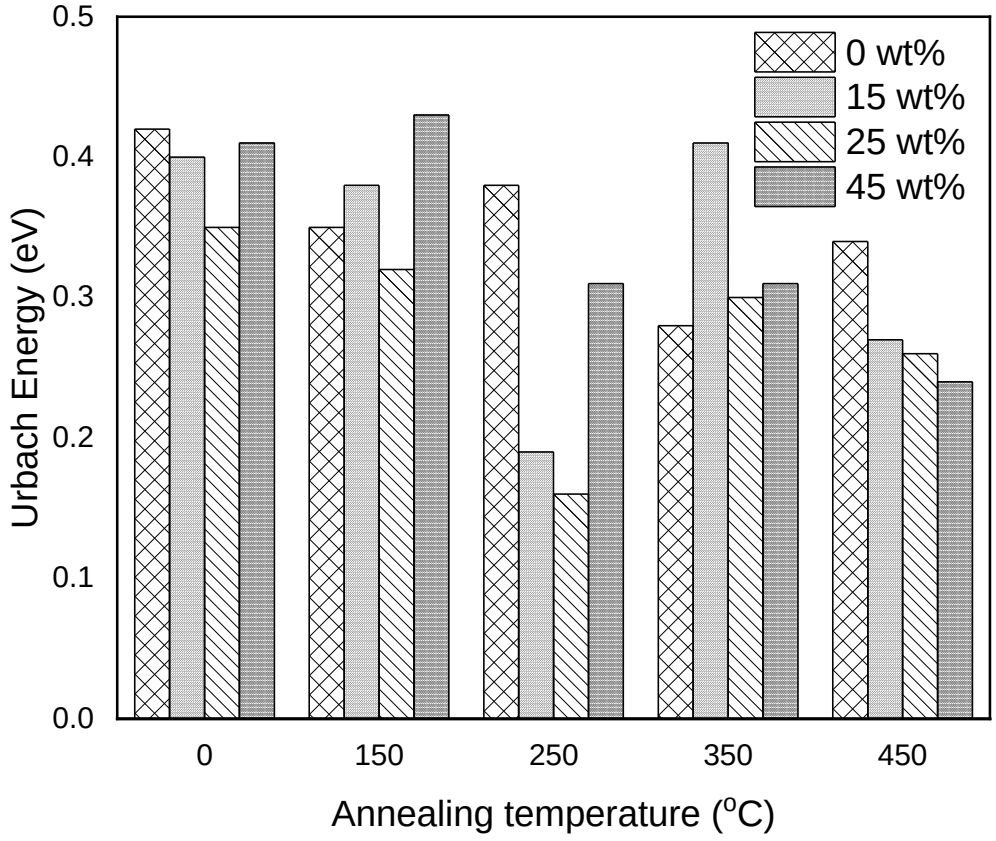

Figure 5. 28: Comparative bar chart showing Urbach energy of nickel doped CdS thin films prepared using chemical bath deposition and annealed at varied temperature (150 °C – 450 °C)

The Urbach energy of both doped and undoped films is then seen to increase as the annealing temperature is raised to 350 °C and finally slightly decreases as the temperature is raised to 450 °C. This can be explained by the change in the structure of the films as the annealing temperature is raised to 350 °C and 450 °C. On annealing the samples at 350 °C and 450 °C, the structure of doped and Ni-doped CdS changes from cubic to the hexagonal structure as confirmed by the X-ray diffraction patterns shown in Figures 5.7 and 5.8. 25 wt% Ni-doped CdS thin films annealed at 250 °C have the minimum Urbach energy of 0.16 eV. This study leads us to suggest that the samples with 25 wt% CdS:Ni thin films would be the most appropriate films to be used in thin-film solar cells because the films had the minimum Urbach energy of 0.16 and the lowest values of extinction coefficient across all wavelengths as discussed in section 5.3.4. The absorption

coefficient of the films was also found to be greater than 10^4 cm^{-1} in the visible region and near-infrared regions which makes the films promising for use as a window/buffer layer in thin-film solar cells and for optoelectronic applications.

5.5 Polarity of Charge Carriers

The polarity of the Hall voltage specifies the net carrier concentration. The Hall voltage is positive for p-type semiconductors and negative for n-type semiconductors. Figure 5.29 shows Hall Effect measurements for Ni-doped CdS thin films annealed at various temperatures.

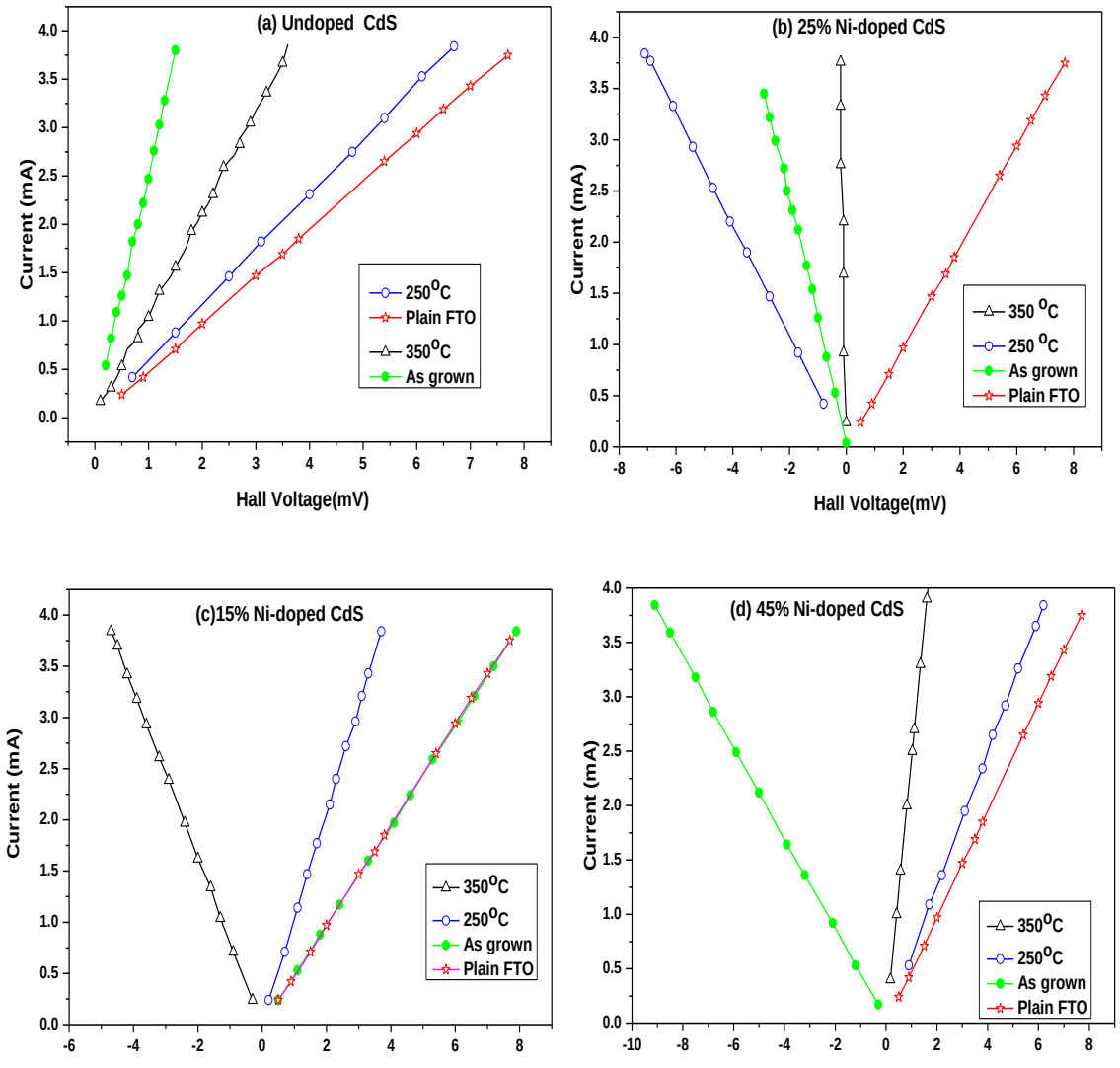

Figure 5. 29: Hall Effect measurements for Ni-doped CdS thin films: (a) undoped CdS (b) CdS with 25 Ni wt% (c) CdS with 15 Ni wt% (d) CdS with 45 Ni wt%

Hall measurements on a plain fluorine-doped tin oxide coated glass slide glass indicated that the conducting glass had a net positive carrier concentration. The majority of charge carriers were positive charges (holes). From Figure 5.29, we observe that as-grown undoped CdS had positive charges as the majority charge carriers. When the undoped CdS thin films were annealed at various temperature (150 ℃, 250 ℃ & 350 ℃), the undoped CdS thin films had a net positive carrier concentration

The Hall voltage for Ni-doped CdS thin films greatly depended on the nickel concentration and annealing temperature as seen in Figure 5.29. The As-prepared CdS doped 15 Ni wt% had a net positive carrier concentration while those doped 25 Ni wt% and doped 45 Ni wt% had a net negative carrier concentration. For a semiconductor to be used as a window/buffer layer in thin film solar cells, the material ought to be n-type for it to form a p-n junction with the absorber layer (p-type). From Figure 5.29 we observe that all the samples containing 25 wt% nickel concentration had negative charges as the majority charge carriers. This leads us to suggest that the samples with 25 wt% Ni-doped CdS thin films would be the most appropriate films to be used as the window/buffer layer for thin-film solar cells.

CHAPTER 6

6.0 CONCLUSION AND SUGGESTIONS FOR FURTHER WORK

6.1 Conclusions

The significant role played by dopants in semiconductor devices has recently stimulated research on the properties and the potential applications of doped semiconductor nanocrystals. Impurities are used to alter the properties of thin films in desirable and controllable ways. Control of the doping profile makes it possible to obtain a desired profile in the growing thin films.

This study focused on the effect of nickel concentration and annealing temperatures on the properties of CdS. For effective incorporation of Ni^{2+} ions into CdS, the films were prepared using chemical bath deposition at a bath temperature of ≈ 33 °C with varying metal ions (Cd^{2+} and Ni^{2+}) with triethanolamine complexing agent and ammonia solution as the pH regulator. The following conclusions were drawn:

1. Elemental analysis was done on CdS:Ni thin films showed the presence of elemental signals of Cd, Ni, and S confirming that Ni^{2+} ions were successfully incorporated into the CdS structure. XRD studies showed that the films were polycrystalline with preferred orientation along (111) direction with the films exhibiting mixed phase structure (both cubic and hexagonal phases). The peak (111) was observed to slightly shifts to the lower angle with increasing Ni^{2+} concentration indicating that Ni ions successfully substituted Cd ions in the CdS lattice owing to their small ionic radius (0.069 nm). The shifting of the peak may be as a result of compressional micro-stress or elongational strain in the CdS lattice, due to the difference in ionic radii of Cd^{2+} ion and the Ni^{2+} ion.
2. Optical studies were carried out on the nickel-doped and undoped CdS films where transmittance, reflectance, bandgap, Urbach energy, and refractive index were determined. From the transmittance spectra, it was evident that the transmittance of the films increased with an increase in dopant concentration. The increase in transmittance and the subsequent decrease in reflectance of CdS:Ni as the dopant concentration increases may be a result of an increase in the crystallinity of the films with increasing dopant concentration. The studies showed that CdS:Ni thin films exhibited good transmittance in the visible and near

infra-red regions of the electromagnetic spectrum (up to 86%). Doping CdS films with nickel widened the bandgap of as-prepared CdS with films doped with 45 wt% registering the highest bandgap of 2.45 (eV). The widening of the CdS bandgap as nickel concentration was increased could be as a result of donor electrons occupying the states at the bottom of the conduction band thus blocking the low energy transitions (Burstein- Moss effect). CdS:Ni thin films were found to have a high absorption coefficient (greater than 10^4 cm^{-1}) in the visible region and near-infrared regions, confirming that the films have a direct optical energy gap. The refractive index of the films was established to decrease with an increase in nickel concentration with 45 wt% CdS:Ni thin films having the lowest refractive index. CdS:Ni films had lower Urbach energy as compared to the undoped CdS films sample with 25wt%. The as-prepared CdS:Ni films had positive charges as the majority charge carriers.

3. There was a significant increase in the transmittance of undoped and nickel-doped CdS films when the films were annealed. Annealing the films encouraged recrystallization, thus improving the crystallinity of the films. XRD patterns indicate that the annealed films are polycrystalline. The composition of the films was not affected when the films were annealed at temperatures below 250 °C. However, annealing the CdS:Ni films at temperatures above 350 °C brought about the partial conversion of CdS to CdO. The bandgap, Urbach energy, and extinction coefficient decreased when the annealing temperature was raised to 250 °C. This could be due to improved crystallinity of the films with increasing annealing temperature and also the grain size increases. Further annealing the CdS:Ni thin films at temperatures 350 °C and 450 °C increased their bandgap, Urbach energy, and extinction coefficient. This could be attributed to the phase transition from cubic (zinc-blend) to hexagonal (wurtzite) structure and reduced strain within the film.
4. This study has leads us to suggest that the samples with 25 wt% CdS:Ni thin films would be the most appropriate films to be used as the window/buffer layer for thin-film solar cells because CdS:Ni with 25 wt% annealed at 250 °C also a net negative carrier concentration. Of all the CdS:Ni films, CdS films with 25 Ni wt% annealed at 250 °C films had the minimum Urbach energy of 0.16 and the lowest values of extinction coefficient across all wavelengths. The absorption coefficient of the films was also found to be greater than 10^4

cm^{-1} in the visible region and near-infrared regions which makes the films promising for use as a window/buffer layer in thin-film solar cells and optoelectronic applications.

6.2 Suggestions for Further Work

In this work, it was observed that doping CdS with nickel ions has an effect on the optical properties of the films e.g. bandgap and Urbach energy. It is important to monitor the level of nickel doping for various applications. Different dopant ions such as rare earth metal and alkali metal may also be incorporated into the CdS structure.

To realize higher conversion efficiencies in thin-film solar cells using the buffer/absorber heterojunction combination, it is important to control film thickness and composition of the Ni-doped thin films by varying the deposition time, pH of the solution, the concentration of the reagents, and temperature of the reaction bath. The main effect of the buffer layer on the heterojunction solar cell is the adjustment of the interface charge, thus ensuring the position of the Fermi level at the interface above the gap centre of the absorber.

REFERENCES

Akbarnejad, E., Ghorannevis, Z., Abbasi, F., Ghoranneviss, M., 2017. Investigation of annealing temperature effect on magnetron sputtered cadmium sulfide thin film properties. *J. Theor. Appl. Phys.* 11, 45–49.

Akintunde, J.A., 2000. Dual impurity doping of buffer solution grown cadmium sulphide thin films: electrical and optical properties. *J. Mater. Sci. Mater. Electron.* 11, 503–508.

Alam, M., Islam, M., Achour, A., Hayat, A., Ahsan, B., Rasheed, H., Salam, S., Mujahid, M., 2014. Solution processing of cadmium sulfide buffer layer and aluminum-doped zinc oxide window layer for thin films solar cells. *Surf. Rev. Lett.* 21, 1450059. https://doi.org/10.1142/S0218625X14500590

Als-Nielsen, J., McMorrow, D., 2011. Elements of Modern X-ray Physics. John Wiley & Sons, New York.

Ayieko, C.O., Musembi, R.J., Waita, S.M., Aduda, B.O., Jain, P.K., 2013. Performance of TiO_2/In (OH) i S j/Pb $(OH)_x$ S_y Composite ETA Solar Cell Fabricated from Nitrogen-Doped TiO_2 Thin Film Window Layer. *Int. J. Mater. Eng.* 3, 11–16.

Ballipinar, F., Rastogi, A.C., 2017. High transmittance cadmium oxysulfide Cd(S,O) buffer layer grown by triton X-100 mediated chemical bath deposition for thin-film heterojunction solar cells. *J. Appl. Phys.* 121, 035302. https://doi.org/10.1063/1.4972964

Balzani, V., Armaroli, N., 2010. Energy for a sustainable world: from the oil age to a sun-powered future. John Wiley & Sons.

Bayon, R., Herrero, J., 2001. Reaction mechanism and kinetics for the chemical bath deposition of In $(OH)_xS_y$ thin films. *Thin Solid Films* 387, 111–114.

Bertran, E., Morenza, J.L., Esteve, J., Codina, J.M., 1984. Electrical properties of polycrystalline In-doped CdS thin films. J. *Phys. Appl. Phys.* 17, 1679.

Bhambhani, P., Alvi, P.A., 2016a. A Systematic Study of the Optical Properties of Co-, and Ni-doped colloidal cadmium sulphide nanoparticles. *J. Optoelectron. Eng.* 4, 11–16.

Bhambhani, P., Alvi, P.A., 2016b. A Systematic Study of the Optical Properties of Co-, and Ni-Doped Colloidal Cadmium Sulphide Nanoparticles. *J. Optoelectron. Eng.* 4, 11–16.

Bhambhani, P., Alvi, P.A., 2016c. A Systematic Study of the Optical Properties of Co-, and Ni-Doped Colloidal Cadmium Sulphide Nanoparticles. *J. Optoelectron. Eng.* 4, 11–16.

Bhargava, R.N., Gallagher, D., Hong, X., Nurmikko, A., 1994. Optical properties of manganese-doped nanocrystals of ZnS. *Phys. Rev. Lett.* 72, 416–419. https://doi.org/10.1103/PhysRevLett.72.416

Borse, P.H., Deshmukh, N., Shinde, R.F., Date, S.K., Kulkarni, S.K., 1999. Luminescence quenching in ZnS nanoparticles due to Fe and Ni doping. *J. Mater. Sci.* 34, 6087–6093. https://doi.org/10.1023/A:1004709601889

Bradford, T., 2006. Solar revolution: the economic transformation of the global energy industry. MIT Press, Cambridge, Mass.

Casper, J.K., 2010. Fossil fuels and pollution: the future of air quality. Facts on File, New York.

Chandramohan, S., Kanjilal, A., Tripathi, J.K., Sarangi, S.N., Sathyamoorthy, R., Som, T., 2009. Structural and optical properties of Mn-doped CdS thin films prepared by ion implantation. *J. Appl. Phys.* 105, 123507. https://doi.org/10.1063/1.3151712

Chandramohan, S., Strache, T., Sarangi, S.N., Sathyamoorthy, R., Som, T., 2010. Influence of implantation-induced Ni-doping on structural, optical, and morphological properties of nanocrystalline CdS thin films. *Mater. Sci. Eng.* B 171, 16–19.

Chandran, R., Suresh, G., 2011. A Comparative Study of Physical and Optical Properties of CdZnS and CdNiS Nanocrystalline Films Deposited by Chemical Bath Method. *Chalcogenide Lett.* 8, 689–694.

Chopra, K.L., Das, S.R., 1983. Thin Film Solar Cells. Springer US, Boston, MA.

Chopra, K.L., Paulson, P.D., Dutta, V., 2004. Thin-film solar cells: an overview. *Prog. Photovolt. Res. Appl.* 12, 69–92.

Chtouki, T., El Kouari, Y., Kulyk, B., Louardi, A., Rmili, A., Erguig, H., Elidrissi, B., Soumahoro, L., Sahraoui, B., 2017. Spin-coated nickel doped cadmium sulfide thin films for third harmonic generation applications. J. Alloys Compd. 696, 1292–1297. https://doi.org/10.1016/j.jallcom.2016.12.089

Conibeer, G., 2007. Third-generation photovoltaics. *Mater. Today* 10, 42–50.

Contreras, M.A., Romero, M.J., To, B., Hasoon, F., Noufi, R., Ward, S., Ramanathan, K., 2002. Optimization of CBD CdS process in high-efficiency Cu (In, Ga) Se_2-based solar cells. *Thin Solid Films* 403, 204–211.

Cox, G.A., 1985. Fundamentals of energy dispersive x-ray analysis. IOP Publishing.

Dona, J.M., Herrero, J., 1997. Chemical bath deposition of CdS thin films: an approach to the chemical mechanism through a study of the film microstructure. *J. Electrochem. Soc.* 144, 4081–4091.

Dutrow, B., Christine, C., n.d. X-ray Powder Diffraction (XRD) [WWW Document]. Techniques. URL https://serc.carleton.edu/research_education/geochemsheets/techniques/XRD.html (accessed 12.05.20).

Elango, M., 2012. Investigation on synthesis, characterization, and associated photocatalytic properties of transition metal (Mn & Ni) doped CdS and ZnS nanomaterials. Anna University.

Ennaoui, A., Eisele, W., Lux-Steiner, M., Niesen, T.P., Karg, F., 2003. Highly efficient Cu (Ga, In)(S, $Se)_2$ thin-film solar cells with zinc-compound buffer layers. *Thin Solid Films* 431, 335–339.

Ennaoui, A., Weber, M., Scheer, R., Lewerenz, H.J., 1998. Chemical-bath ZnO buffer layer for $CuInS_2$ thin-film solar cells. *Sol. Energy Mater. Sol. Cells* 54, 277–286.

Enríquez, J., 2003. Influence of the thickness on structural, optical, and electrical properties of chemical bath deposited CdS thin films. Sol. Energy Mater. Sol. Cells 76, 313–322. https://doi.org/10.1016/S0927-0248(02)00283-0

Epina eBook Team, 2006. Cadmium Sulfide [WWW Document]. URL http://www.vias.org/genchem/chem_cds.html (accessed 2.8.19).

Ezugwu, S.C., Ezema, F.I., Osuji, R.U., Asogwa, P.U., Ekwealor, A.B.C., Ezekoye, B.A., 2009. Effect of deposition time on the band-gap and optical properties of chemical bath deposited CdNiS thin films. *Optoelectron. Adv. Mater. Commun*. 3, 141–144.

Fyfe, W.S., Powell, M.A., Hart, B.R., Ratanasthien, B., 1993. A global crisis: Energy in the future. *Nonrenewable Resource*. 2, 187–196. https://doi.org/10.1007/BF02257914

Gellings, P.J., Bouwmeester, H.J., 1997. Handbook of solid state electrochemistry. CRC press.

George, P.J., Sánchez, A., Nair, P.K., Nair, M.T.S., 1995. Doping of chemically deposited intrinsic CdS thin films to n-type by thermal diffusion of indium. *Appl. Phys. Lett.* 66, 3624–3626. https://doi.org/10.1063/1.113808

Gaber, A., Abdel-Rahim, M.A., Abdel-Latief, A.Y., Abdel-Salam, M.N., 2014. Influence of calcination temperature on the structure and porosity of nanocrystalline SnO_2 synthesized by a conventional precipitation method. *Int J Electrochem Sci* 9, 81–95.

Green, M.A., Hishikawa, Y., Dunlop, E.D., Levi, D.H., Hohl-Ebinger, J., Ho-Baillie, A.W.Y., 2018. Solar cell efficiency tables (version 52). *Prog. Photovolt. Res. Appl*. 26, 427–436. https://doi.org/10.1002/pip.3040

Guillén, C., Martínez, M.A., Herrero, J., 1998. Accurate control of thin film CdS growth process by adjusting the chemical bath deposition parameters. *Thin Solid Films* 335, 37–42.

Hall Effect [WWW Document], n.d. URL http://hyperphysics.phy-astr.gsu.edu/hbase/magnetic/Hall.html (accessed 1.29.18).

Hariskos, D., Spiering, S., Powalla, M., 2005. Buffer layers in Cu(In, Ga)Se_2 solar cells and modules. *Thin Solid Films* 480, 99–109.

Haynes, W.M., 2014. CRC Handbook of Chemistry and Physics. CRC Press.

Khallaf, H., Chai, G., Lupan, O., Chow, L., Heinrich, H., Park, S., Schulte, A., 2009a. In-situ boron doping of chemical-bath deposited CdS thin films. *Phys. Status Solidi A* 206, 256–262. https://doi.org/10.1002/pssa.200824290

Khallaf, H., Chai, G., Lupan, O., Chow, L., Park, S., Schulte, A., 2009b. Characterization of gallium-doped CdS thin films grown by chemical bath deposition. *Appl. Surf. Sci.* 255, 4129–4134. https://doi.org/10.1016/j.apsusc.2008.10.115

Hodes, G., 2002. Chemical solution deposition of semiconductor films. CRC Press.

Hollars, D.R., 2005. Thin-film solar cells. US6974976 B2.

Huang, C.H., Li, S.S., Shafarman, W.N., Chang, C.-H., Lambers, E.S., Rieth, L., Johnson, J.W., Kim, S., Stanbery, B.J., Anderson, T.J., 2001. Study of Cd-free buffer layers using In x (OH, S)$_y$ on CIGS solar cells. *Sol. Energy Mater. Sol. Cells* 69, 131–137.

Hubert, C., Naghavi, N., Etcheberry, A., Roussel, O., Hariskos, D., Powalla, M., Kerrec, O., Lincot, D., 2008. A better understanding of the growth mechanism of Zn (S, O, OH) chemical bath deposited buffer layers for high-efficiency Cu(In, Ga)(S, Se)$_2$ solar cells. *Phys. Status Solidi A* 205, 2335–2339.

Jackson, P., Hariskos, D., Lotter, E., Paetel, S., Wuerz, R., Menner, R., Wischmann, W., Powalla, M., 2011. New world record efficiency for Cu (In, Ga) Se$_2$ thin-film solar cells beyond 20wt%. *Prog. Photovolt. Res. Appl.* 19, 894–897.

Jäger, H., Seipp, E., 1981. Burstein-Moss shift in heavily In-doped evaporated CdS layers. J. *Appl. Phys.* 52, 425–427.

Jeyaprakash, B.G., Kumar, R.A., Kesavan, K., Amalarani, A., 2010. Structural and optical characterization of spray deposited SnS thin film. *J Am Sci* 6, 22.

Khallaf, H., Chai, G., Lupan, O., Chow, L., Park, S., Schulte, A., 2009. Characterization of gallium-doped CdS thin films grown by chemical bath deposition. *Appl. Surf. Sci.* 255, 4129–4134. https://doi.org/10.1016/j.apsusc.2008.10.115

Khallaf, H., Chai, G., Lupan, O., Chow, L., Park, S., Schulte, A., 2008. Investigation of aluminium and indium in situ doping of chemical bath deposited CdS thin films. *J. Phys. Appl. Phys.* 41, 185304.

Khan, Z.R., Zulfequar, M., Khan, M.S., 2010. Effect of thickness on structural and optical properties of thermally evaporated cadmium sulfide polycrystalline thin films. *Chalcogenide Lett.* 7, 431–438.

Kim, Y.D., Chang, Y.-C., Klein, M.V., 1993. Effect of d-electrons in transition-metal ions on band-gap energies of diluted magnetic semiconductors. *Phys. Rev. B* 48, 17770.

Kumar, S., Sharma, P., Sharma, V., 2013. Phase Transition in II–VI nanofilms of dilute magnetic semiconductors: $Cd_{1-x}Ni_x$ S. Sci. Adv. *Mater*. 5, 713–717.

Kumar, S., Sharma, P., Sharma, V., 2012. Structural transition in II-VI nanofilms: Effect of molar ratio on structural, morphological, and optical properties. *J. Appl. Phys*. 111, 113510. https://doi.org/10.1063/1.4724347

Lakshmi, M., 2001. Studies on chemical bath deposited semiconducting copper selenide and iron sulfide thin films useful for photovoltaic applications.

Li, Y., Chen, Z., Cao, C., Usman, Z., Feng, Y., Pan, Z., Wu, Z., 2012. The controllable synthesis, structural, and ferromagnetic properties of Co-doped GaN nanowires. *Appl. Phys. Lett*. 100, 232404.

Liu, F., Lai, Y., Liu, J., Wang, B., Kuang, S., Zhang, Z., Li, J., Liu, Y., 2010. Characterization of chemical bath deposited CdS thin films at different deposition temperatures. *J. Alloys Compd*. 493, 305–308. https://doi.org/10.1016/j.jallcom.2009.12.088

Lohninger, H., 2011. Cadmium Sulfide [WWW Document]. URL http://www.vias.org/genchem/chem_cds.html (accessed 11.14.17).

Lokhande, C.D., Pawar, S.H., 1982. Optical and transport properties of chemical bath deposited CdS: Al films. *Solid State Commun*. 44, 1137–1139.

Lu, J.G., Fujita, S., Kawaharamura, T., Nishinaka, H., Kamada, Y., Ohshima, T., Ye, Z.Z., Zeng, Y.J., Zhang, Y.Z., Zhu, L.P., 2007. Carrier concentration dependence of bandgap shift in n-type ZnO: Al films. *J. Appl. Phys.* 101, 083705.

Mahdi, M.A., Kasem, S.J., Hassen, J.J., Swadi, A.A., 2009. Structural and optical properties of chemical deposition CdS thin films. *Int. J. Nanoelectronics and Materials* 2 (2009) 163-172

Mane, R.S., Lokhande, C.D., 2000. Chemical deposition method for metal chalcogenide thin films. *Mater. Chem. Phys*. 65, 1–31.

Marquina, R.S., Sanchez, T.G., Mathews, N.R., Mathew, X., 2017. Vacuum coated Sb_2S_3 thin films: Thermal treatment and the evolution of its physical properties. *Mater. Res. Bull.* 90, 285–294.

Mathew M (2009). Engineering the properties of indium sulfide for thin-film solar cells by doping. Ph.D. thesis Cochin Univ. Sci. Technol. pp.1-2.

McGlade, C., Ekins, P., 2015. The geographical distribution of fossil fuels unused when limiting global warming to 2 °C. *Nature* 517, 187.

Metin, H., Esen, R., 2003. Annealing effects on optical and crystallographic properties of CBD grown CdS films. Semicond. Sci. Technol. 18, 647–654. https://doi.org/10.1088/0268-1242/18/7/308

Mocatta, D., Cohen, G., Schattner, J., Millo, O., Rabani, E., Banin, U., 2011. Heavily doped semiconductor nanocrystal quantum dots. *Science* 332, 77–81.

Mondal, A., Chaudhuri, T.K., Pramanik, P., 1983. Deposition of cadmium chalcogenide thin films by a solution growth technique using triethanolamine as a complexing agent. *Sol. Energy Mater*. 7, 431–438.

Monshi, A., Foroughi, M.R., Monshi, M.R., 2012. Modified Scherrer Equation to Estimate More Accurately Nano-Crystallite Size Using XRD. *World J. Nano Sci. Eng*. 02, 154–160. https://doi.org/10.4236/wjnse.2012.23020

Moskovits, M., Soles, G., 1990. Chemical Physics of Atomic and Molecular Clusters. Soles, G. (Ed.).

Moutinho, H.R., Albin, D., Yan, Y., Dhere, R.G., Li, X., Perkins, C., Jiang, C.-S., To, B., Al-Jassim, M.M., 2003. Deposition and properties of CBD and CSS CdS thin films for solar cell application. *Thin Solid Films* 436, 175–180.

Mushtaq, S., Ismail, B., Raheel, M., Zeb, A., 2016. Nickel antimony sulphide thin films for solar cell application: Study of optical constants. https://doi.org/10.4236/ns.2016.82004

Mustafa, G., Chowdhury, M.R.I., Saha, D.K., Hussain, S., Islam, O., 2012. Annealing effects on the properties of chemically deposited CdS thin films at ambient condition. Dhaka Univ. J. Sci. 60, 283–288.

Naciri, R., Bihri, H., Mzerd, A., Rahioui, A., Abd-Lefdil, M., Messaoudi, C., 2007. The role of the CdS buffer layer in the $CuInS_2$ thin film solar cell. *Rev. Energ. Reneouvelables CER* 7, 165–168.

Nair, M.T.S., Nair, P.K., Campos, J., 1988. Effect of bath temperature on the optoelectronic characteristics of chemically deposited CdS thin films. *Thin Solid Films* 161, 21–34.

Nair, M.T.S., Nair, P.K., Zingaro, R.A., Meyers, E.A., 1994. Conversion of chemically deposited photosensitive CdS thin films to n-type by air annealing and ion exchange reaction. *J. Appl. Phys.* 75, 1557–1564.

Nair, P.K., Daza, O.G., Readigos, A.A.-C., Campos, J., Nair, M.T.S., 2001. Formation of conductive CdO layer on CdS thin films during air heating. *Semicond. Sci. Technol.* 16, 651.

Nakada, T., Hongo, M., Hayashi, E., 2003. Band offset of high efficiency CBD-ZnS/CIGS thin film solar cells. *Thin Solid Films* 431, 242–248.

Nakada, T., Mizutani, M., 2002. 18wt% efficiency Cd-free Cu (In, Ga) Se2 thin-film solar cells fabricated using chemical bath deposition (CBD)-ZnS buffer layers. *Jpn. J. Appl. Phys.* 41, L165.

Nwofe, P.A., Agbo, P.E., 2017. Annealing treatments and characterisation of Ni-doped antimony sulphide thin films. *J. Non-Oxide Glas.* 9, 9–17.

O'Leary, S.K., Johnson, S.R., Lim, P.K., 1997. The relationship between the distribution of electronic states and the optical absorption spectrum of an amorphous semiconductor: An empirical analysis. *J. Appl. Phys.* 82, 3334–3340.

Oriaku, C.I., Ezema, F.I., Osuwa, J.C., 2008. Fabrication and optical constants of CdMnS ternary thin films deposited by chemical bath. *Pac. J. Sci. Technol.* 10, 413–416.

Ortega-Borges, R., Lincot, D., 1993. Mechanism of chemical bath deposition of cadmium sulfide thin films in the ammonia-thiourea system in-situ kinetic study and modelization. *J. Electrochem. Soc.* 140, 3464–3473.

Ottih, I.E., Ekpunobi, A.J., 2011. Fabrication and characterisation of high efficiency solar cell thin films (CdNiS). *Pac. J. Sci. Technol.* 12, 351–355.

Ottih, I.E., Ekpunobi, A.J., Ekwo, P.I., 2011. Solid state and optical properties of chemical bath deposited copper nickel sulphide (CuNiS) thin films". *Pac. J. Sci. Technol.* 12, 342–347.

Park, W.-D., 2012. Optical constants and dispersion parameters of CdS thin film prepared using chemical bath deposition. *Trans. Electr. Electron. Mater.* 13, 196–199.

Park, W.-D., 2011. Structural, optical and photoconductive properties of chemically deposited nanocrystalline CdS thin films. *Trans. Electr. Electron. Mater.* 12, 164–168.

Paskov, P.P., 1997. Refractive indices of InSb, InAs, GaSb, $InAs_xSb_{1-x}$, and $In_{1-x}Ga_xSb$: Effects of free carriers. *J. Appl. Phys.* 81, 1890–1898. https://doi.org/10.1063/1.365360

Patidar, M.M., Ajay, A., Wala, A.D., Kiran, N., Panda, R., Gangrade, M., Nath, R., Ganesan, V., 2014. Persistence photo conductivity in Ni doped CdS, in: *Journal of Physics: Conference Series*. IOP Publishing, p. 012046.

Pawar, S.M., Pawar, B.S., Kim, J.H., Joo, O.-S., Lokhande, C.D., 2011. Recent status of chemical bath deposited metal chalcogenide and metal oxide thin films. *Curr. Appl. Phys*. 11, 117–161.

Perednis, D., 2003. Thin film deposition by spray pyrolysis and the application in solid oxide fuel cells (PhD Thesis).

Peter, W., Uli, W., 2016. Physics of solar cells: from basic principles to advanced concepts. John Wiley & Sons.

Petre, D., Pintilie, I., Pentia, E., Botila, T., 1999. The influence of Cu doping on opto-electronic properties of chemically deposited CdS. *Mater. Sci. Eng*. B 58, 238–243.

Podlowski, L., Heitz, R., Hoffmann, A., Broser, I., 1992. Non-radiative recombination processes of Ni-impurities in CdS and ZnS. *J. Lumin*. 53, 401–405.

Popovic, R.S., 2003. Hall Effect devices. CRC Press.

Rajput, N., 2015. Methods of preparation of nanoparticles-A review. *Int. J. Adv. Eng. Technol*. 7, 1806.

Rao, B.S., Kumar, B.R., Reddy, V.R., Rao, T.S., Chalapathi, G.V., 2011. Structural characterization of nickel-doped cadmium sulfide. *Chalcogenide Lett.* 8, 53–58.

Reádigos, A.A.-C., Garcia, V.M., Gomezdaza, O., Campos, J., Nair, M.T.S., Nair, P.K., 2000. Substrate spacing and thin-film yield in chemical bath deposition of semiconductor thin films. *Semicond. Sci. Technol*. 15, 1022.

Renewable Power Generation Costs in 2012: An Overview [WWW Document], n.d.. Publ.-Power-Gener.-Costs--2012--Overv. URL /publications/2013/Jan/Renewable-Power-Generation-Costs-in-2012-An-Overview (accessed 3.30.18).

Ristova, M., 1998. Silver-doped CdS films for PV application. *Sol. Energy Mater. Sol. Cells* 53, 95–102. https://doi.org/10.1016/S0927-0248 (98)00011-7

Rmili, A., Ouachtari, F., Bouaoud, A., Louardi, A., Chtouki, T., Elidrissi, B., Erguig, H., 2013. Structural, optical and electrical properties of Ni-doped CdS thin films prepared by spray pyrolysis. *J. Alloys Compd*. 557, 53–59.

Sahu, S.N., Chandra, S., 1987. Chemical-bath-deposited CdS and CdS: Li films and their use in photoelectrochemical solar cells. *Sol. Cells* 22, 163–173.

Schubert, E.F., 2015. Doping in III-V semiconductors. Cambridge University Press, Cambridge.

SCOUT tutorial 1 [WWW Document], n.d. URL http://www.mtheiss.com/docs/sc2_tu1/index.html (accessed 10.14.17).

Sebastian, P.J., 1993. P-type CdS thin films formed by in situ Cu-doping in the chemical bath. *Appl. Phys. Lett*. 62, 2956–2958.

Shah, A.V., Platz, R., Keppner, H., 1995. Thin-film silicon solar cells: A review and selected trends. *Sol. Energy Mater. Sol. Cells* 38, 501–520. https://doi.org/10.1016/0927-0248(94)00241-X

Shikalgar, A.G., Pawar, S.H., 1979. Electric properties of chemically deposited lithium doped cadmium sulphide films. *Solid State Commun*. 32, 361–368.

Shur, M., 1990. Physics of Semiconductor Devices, Prentice-Hall series in solid state physical electronics. Prentice Hall.

Siebentritt, S., 2004. Alternative buffers for chalcopyrite solar cells. *Sol. Energy* 77, 767–775.

Solanki, P.S., 2010. Studies on mixed oxide functional ceramics (PhD Thesis). Saurashtra

University.

Sozzi, G., Troni, F., Menozzi, R., 2014. On the combined effects of window/buffer and buffer/absorber conduction-band offsets, buffer thickness and doping on thin-film solar cell performance. *Sol. Energy Mater. Sol. Cells* 121, 126–136. https://doi.org/10.1016/j.solmat.2013.10.037

Sta, I., Jlassi, M., Hajji, M., Boujmil, M.F., Jerbi, R., Kandyla, M., Kompitsas, M., Ezzaouia, H., 2014. Structural and optical properties of TiO2 thin films prepared by spin coating. *J. Sol-Gel Sci. Technol.* 72, 421–427.

Street, R.A., 1991. Hydrogenated amorphous silicon, Cambridge solid state science series. Cambridge University Press, Cambridge ; New York.

Sze, S. M. Physics of Semiconductor Devices (Wiley-Interscience, New York, ed. 2, 1981).

Thakur, S., Kumar, J., Sharma, J., Sharma, N., Kumar, P., 2013. Structural and optical study of nickel-doped ZnO nanoparticles and thin films for dye sensitized solar cell applications. *J. Optoelectron. Adv. Mater.* 15, 989–994.

Thankalekshmi, R.R., Rastogi, A.C., 2012. Structure and optical bandgap of $ZnO_{1-x}S_x$ thin films synthesized by chemical spray pyrolysis for application in solar cells. *J. Appl. Phys*. 112, 063708.

Thomail, Mahir N., Studying the Optical Properties of CdS Thin Films Prepared by Thermal Vacuum Evaporation Technique with a Different Thickness. *J. of University of Anbar for Pure Science* 6(1) (2012), (4 pages).

Von Roedern, B., Bauer, G.H., 1999. Material requirements for buffer layers used to obtain solar cells with high open circuit voltages, in: MRS Proceedings. Cambridge University Press, p. 761.

Wang, Y., Wu, J., Zheng, J., Jiang, R., Xu, R., 2012. Ni^{2+}-doped $Zn_x Cd_{1-x} S$ photocatalysts from single-source precursors for efficient solar hydrogen production under visible light irradiation. *Catal. Sci. Technol*. 2, 581–588. https://doi.org/10.1039/C2CY00310D

Warren, B.E., 1990. X-ray Diffraction. Dover Publisher, New York.

World Energy Outlook 2018 [WWW Document], URL https://www.iea.org/weo2018/ (accessed 5.7.19).

Wu, P.-G., Ma, C.-H., Shang, J.K., 2005. Effects of nitrogen doping on optical properties of TiO_2 thin films. *Appl. Phys*. A 81, 1411–1417. https://doi.org/10.1007/s00339-004-3101-4

Wu, X.J., Shen, D.Z., Zhang, Z.Z., Zhang, J.Y., Liu, K.W., Li, B.H., Lu, Y.M., Zhao, D.X., Yao, B., 2006. P-type conductivity and donor-acceptor pair emission in Cd_{1-x} Fe_xS dilute magnetic semiconductors. *Appl. Phys. Lett.* 89, 262118. https://doi.org/10.1063/1.2425028

X-ray diffraction – Bruker D8 Discover [WWW Document], n.d. URL https://fys.kuleuven.be/iks/nvsf/experimental-facilities/x-ray-diffraction-2013-bruker-d8-discover (accessed 1.29.18).

Zelaya-Angel, O., Hernandez, L., de Melo, O., Alvarado-Gil, J., Lozada-Morales, R., Falcony, C., Vargas, H., Ramirez-Bon, R., 1995. Band-gap shift in CdS: phase transition from cubic to hexagonal on thermal annealing. Vacuum 46, 1083–1085. https://doi.org/10.1016/0042-207X(95)00111-5

7.0 APPENDIX: CRYSTALLITE SIZE OF UNDOPED AND CdS:Ni THIN FILMS PREPARED BY CHEMICAL BATH DEPOSITION AND ANNEALED AT VARIOUS TEMPERATURES

Table 6. 1: Crystallite size of the as-grown undoped CdS thin films

Crystallite size of as-prepared undoped CdS						
2-Theta	Phase ID	*h*	*k*	*l*	FWHM	Crystallite size (nm)
26.74	CdS	0	0	2	0.67	12.69
29.32	NiC_x	1	1	1	0.35	24.71
31.20	Ni_3S_2	1	1	0	0.96	9.00
44.26	CdS	1	1	0	0.87	10.34
Average crystallite size = 14.19 nm						

Table 6. 2: Crystallite grain size of the as-prepared 35 wt% Ni-doped thin films

As-prepared, 35 wt% Ni-doped CdS						
2-Theta	Phase ID	*h*	*k*	*l*	FWHM	Crystallite size (nm)
26.67	CdS	0	0	2	0.65	13.19
29.30	CdO_2	1	1	1	0.34	25.21
31.42	Ni_3S_4	1	1	3	0.69	12.43
37.98	Ni_3S_4	0	0	4	0.40	21.87
43.94	CdS	2	2	0	0.79	11.29
44.38	Ni_3S_2	2	0	2	0.78	11.51
47.38	Ni_3S_{42}	2	2	4	0.33	27.53
48.46	CdO_2	2	2	0	0.29	31.26
Average crystallite size = 19.29 nm						

Table 6. 3: Crystallite grain size of the as-prepared 45 wt% Ni-doped thin films

As-prepared, 45 wt% Ni-doped CdS						
2-Theta	Phase ID	*h*	*k*	*l*	FWHM	Crystallite size (nm)
26.52	CdS	0	0	2	0.54	15.87
29.12	CdO_2	1	1	1	0.55	15.47
31.18	Ni_3S_4	1	1	3	0.59	14.59
33.72	CdO_2	2	0	0	0.30	29.28
44.00	CdS	2	2	0	0.79	11.28
54.62	CdS	0	0	4	0.40	23.34
64.48	Ni_3S_4	3	3	5	0.37	26.36
Average crystallite size = 19.46 nm						

Table 6. 4: Crystallite grain size of undoped CdS thin films annealed at 250 °C

Undoped CdS thin films annealed at 250 °C						
2-Theta	Phase ID	*h*	*k*	*l*	FWHM	Crystallite size (nm)
26.52	CdS	1	1	1	0.67	12.72
31.42	CdO	1	1	3	0.71	12.00
32.94	CdO	1	1	1	0.54	16.08
38.28	CdO	2	0	0	0.52	16.88
44.00	CdS	2	2	0	0.84	10.7
55.34	CdO	2	2	0	0.58	16.09
Average crystallite size = 14.08 nm						

Table 6. 5: Crystallite grain size of 15 wt% Ni-doped thin films annealed at 250 ℃

15 wt% Ni-doped CdS annealed at 250 ℃						
2-Theta	Phase ID	*h*	*k*	*l*	FWHM	Crystallite size (nm)
26.54	CdS	1	1	1	0.58	14.77
32.88	CdO	1	1	1	0.52	16.69
33.68	CdO_2	2	0	0	0.20	42.90
37.76	Ni_3S_4	4	0	0	0.41	21.17
47.44	S	3	2	1	0.35	26.11
48.38	CdO_2	2	2	0	0.31	29.43
54.58	CdS	2	2	2	0.62	15.10
55.20	CdO	2	2	0	0.93	10.05
57.38	Ni_3S_4	5	3	1	0.37	25.28
61.66	Ni_3S_4	6	2	0	0.41	23.50
64.54	Ni_3S_4	3	3	5	0.41	24.16
65.72	CdO	3	1	1	0.52	19.10
Average crystallite size = 22.36 nm						

Table 6. 6: Crystallite grain size of 35 wt% Ni-doped thin films annealed at 250 ℃

35 wt% Ni-doped CdS annealed at 250 ℃						
2-Theta	Phase ID	*h*	*k*	*l*	FWHM	Crystallite size (nm)
22.76	S	1	0	1	0.86	9.85
29.18	CdO_2	1	1	1	0.41	20.90
32.84	Ni_3S_4	2	2	2	0.51	16.82
33.72	CdO_2	2	0	0	0.49	17.69
37.82	Ni_3S_4	4	0	0	0.47	18.53
38.36	CdO	2	0	0	0.98	8.98
47.42	S	3	2	1	0.35	25.73
48.38	CdO_2	2	2	0	0.32	28.33
55.30	CdO	2	2	0	1.19	7.87
61.66	Ni_3S_4	6	2	0	0.48	20.34
65.78	CdO	3	1	1	0.60	16.57
Average crystallite size = 17.42 nm						

Table 6. 7: Crystallite grain size of 45 wt% Ni-doped thin films annealed at 250 ℃

45 wt% Ni-doped CdS annealed at 250 ℃						
2-Theta	Phase ID	*h*	*k*	*l*	FWHM	Crystallite size (nm)
22.96	S	1	0	1	0.35	24.32
29.24	CdO_2	1	1	1	0.41	20.80
32.88	Ni_3S_4	2	2	2	0.86	10.01
37.82	Ni_3S_4	4	0	0	0.47	18.53
38.30	CdO	2	0	0	0.61	14.39
61.66	Ni_3S_4	6	2	0	0.48	20.34
48.44	CdO_2	2	2	0	0.26	35.67
Average crystallite size = 20.58 nm						

Table 6. 8: Crystallite grain size of undoped CdS thin films annealed at 350 ℃

CdS thin films annealed at 350 ℃						
2-Theta	Phase ID	*h*	*k*	*l*	FWHM	Crystallite size (nm)
24.88	CdS	1	0	1	0.48	17.73
26.50	CdS	1	1	1	0.43	20.05
28.16	CdS	1	0	1	0.64	13.36
32.96	CdO	1	1	1	0.40	21.52
55.24	CdO	2	2	0	0.48	19.46
65.86	CdO	3	1	1	0.49	20.01
Average crystallite size = 18.69 nm						

Table 6. 9: Crystallite grain size of the 15 wt% Ni-doped thin films annealed at 350 °C

15wt% Ni-doped CdS annealed at 350 °C						
2-Theta	Phase ID	*h*	*k*	*l*	FWHM	Crystallite size (nm)
24.84	CdS	1	0	0	0.45	19.04
26.52	CdS	0	0	2	0.38	22.31
28.30	CdS	1	0	1	0.73	11.78
31.16	Ni_3S_2	1	1	0	0.27	32.01
32.98	CdO	1	1	1	0.40	21.84
37.78	Ni_3S_2	0	0	3	0.38	23.38
38.26	Ni_3S_2	0	2	1	0.42	20.85
43.72	CdS	1	1	0	0.60	14.97
55.28	CdO	1	1	4	0.43	21.59
65.92	CdO	3	1	1	0.46	21.73
Average crystallite size = 20.95 nm						

Table 6. 10: Crystallite grain size of 35 wt% Ni-doped thin films annealed at 350 °C

35wt% Ni-doped CdS thin films annealed at 350 °C						
2-Theta	Phase ID	*h*	*k*	*l*	FWHM	Crystallite size (nm)
26.64	CdS	0	0	2	0.37	23.04
29.26	CdO_2	1	1	1	0.37	23.36
31.16	Ni_3S_2	1	1	0	0.27	32.01
33.04	CdO	1	1	1	0.36	24.03
37.78	Ni_3S_2	0	0	3	0.38	23.38
38.26	Ni_3S_2	0	2	1	0.42	20.85
38.32	CdO	2	0	0	0.36	24.25
48.42	CdO_2	2	2	0	0.29	31.91
55.28	CdO	1	1	4	0.42	22.19
69.34	CdO	2	2	2	0.46	22.12
Average crystallite size = 24.71 nm						

Table 6. 11: Crystallite grain size of the undoped CdS thin films annealed at 450 ℃

Pure CdS thin films annealed at 450 ℃						
2-Theta	Phase ID	*h*	*k*	*l*	FWHM	Crystallite size (nm)
26.56	CdS	0	0	2	0.44	19.19
29.30	CdO_2	1	1	1	0.47	18.12
32.96	CdO	1	1	1	0.38	22.7
55.24	CdO	2	2	0	0.41	23.06
65.88	CdO	3	1	1	0.42	23.31
Average crystallite size = 21.28 nm						

Table 6. 12: Crystallite grain size of 15wt% Ni-doped thin films annealed at 450 ℃

15 wt% Ni-doped CdS annealed at 450 ℃						
2-Theta	Phase ID	*h*	*k*	*l*	FWHM	Crystallite size (nm)
26.54	CdS	0	0	2	0.40	21.46
31.18	Ni_3S_2	1	1	0	0.36	23.92
32.98	CdO	1	1	1	0.35	25.07
33.72	CdO_2	2	0	0	0.22	39.39
38.28	CdO	2	0	0	0.31	27.69
52.22	CdS	3	1	1	0.64	14.43
54.68	Ni_3S_2	1	0	4	0.66	14.15
55.26	CdO	2	2	0	0.37	25.65
65.90	CdO	3	1	1	0.41	24.41
Average crystallite size = 24.02 nm						